Copyright

by

Liam Glazer Connolly

2022

The Dissertation Committee for Liam Glazer Connolly certifies that this is the approved version of the following Dissertation:

ENABLING HYBRID PROCESS METROLOGY IN ROLL-TO-ROLL NANOMANUFACTURING:

Design of a Tip-Based Tool for Topographic Sampling on Flexible Substrates

Committee:

____
Michael A. Cullinan, Supervisor

____
S.V. Sreenivasan

____
Dragan Djurdjanovic

____
Lei Zhou

____
Neil Sarkar

ENABLING HYBRID PROCESS METROLOGY IN ROLL-TO-ROLL NANOMANUFACTURING:

Design of a Tip-Based Tool for Topographic Sampling on Flexible Substrates

by

Liam Glazer Connolly

Dissertation

Presented to the Faculty of the Graduate School of

The University of Texas at Austin

in Partial Fulfillment

of the Requirements

for the Degree of

Doctor of Philosophy

The University of Texas at Austin

May 2022

Dedication

To my ever-supportive parents, Amy and James, and the family, friends, colleagues, and mentors without whom I could not have made it this far.

Acknowledgements

I must profoundly thank my PI, Dr. Michael Cullinan, for his unflappable support, invaluable advice, and our lively debates which have led to this work. I'd also acknowledge the continuing help and support of my lab-mates Dr. Georgina Dibua, Dr. Dipankar Behera, David Cayll, Dr. Martin Ward, Dr. Nilabh Roy, Barbara Groh, Eva Natinsky, Dr. Tsung-Fu Yao and one of the hardest working undergraduate research assistants I've had the pleasure of mentoring, James Garcia. I would also like to thank David Morris from the ICSPI Corporation for his continued advice and material support. Lastly, I would acknowledge the support, expertise, and patience of my committee who were critical in shaping this work.

This research is based upon work supported primarily by the National Science Foundation under Cooperative Agreement No. EEC-1160494 and by the National Science Foundation Graduate Research Fellowship program under Grant No. 2017251210.

Abstract

ENABLING HYBRID PROCESS METROLOGY IN ROLL-TO-ROLL NANOMANUFACTURING:

A Tip-Based Tool for Topographic Sampling on Flexible Substrates

Liam Glazer Connolly, Ph.D.

The University of Texas at Austin, 2022

Supervisor: Michael A. Cullinan

This work seeks to demonstrate the efficacy of a novel approach for topography measurement of nano-scale structures fabricated on a flexible substrate in a roll-to-roll (R2R) fashion. R2R manufactured products can be extremely cost competitive compared to more traditional, silicon wafer or glass panel based nanofabrication solutions, in addition to the unique and often desirable mechanical properties inherent to flexible substrates. As such, flexible nanomanufacturing is an area of immense research interest. However, despite the significant potential of these products for a variety of applications, developing manufacturing systems from lab-scale prototypes to pilot- or high volume manufacturing (HVM) has often proven both difficult and infeasibly expensive as research investment and achievable process yield limit advancement. One of the most significant capability gaps in current art, and roadblocks on the path towards adoption of R2R nanomanufacturing, is the lack of high-throughput, nanometer-scale metrology for process development, real-time control, and yield enhancement. This dissertation presents the design of a tip-based measurement tool implementing atomic force microscope (AFM) probes manufactured with a micro-electro-mechanical system (MEMS) approach to the challenge of sub-micron topography measurement which is also compatible with R2R manufacturing on flexible

substrates. A proof-of-concept prototype tool with subsystems to regulate a flexible web, isolate and position the atomic force microscope probe, and measure features on the substrate, all coordinated by a real-time embedded control system, was designed and fabricated. The positioning subsystem was evaluated dynamically to ensure initial design requirements were met, and stationery, step-and-scan results were presented. However, to wholly meet this extent need for in-line R2R metrology, a system capable of atomic force microscope scanning despite a continuous, non-zero substrate velocity is required - any regular stoppage of the web in a R2R process all but dooms economically viable production throughput. Refinement and redesign of the proof-of-concept tool was driven by new system requirements to meet this goal, in addition to lessons learned from the initial prototype. Improvements focused on upgrading the web handling spindle design and mechatronics, tool power electronics, moving structures, and control algorithms used for high-speed synchronous positioning of the atomic force microscope and web. The culmination of this work will serve to introduce a new measurement framework which may be used to accelerate and enable future research in R2R manufacturing of nanofeatured products.

Table of Contents

List of Tables 11

List of Figures 12

CHAPTER 1 - INTRODUCTION 18

1.1 Photonic imaging Methods 20

1.1.1 Direct Optical Inspection 20

1.1.2 Diffraction limits and The Airy Disk 21

1.1.3 Indirect Optical Inspection 23

1.2 Electron Beam Methods 25

1.3 Tip-based Methods 26

1.3.1 Single-Chip Atomic Force Microscope 27

1.4 Thesis Overview 29

1.4.1 The State of Advanced, Multi-layer R2R Nanomanufacturing 29

1.4.2 Proof-of-Concept R2R Tip-based Measurement Prototype.................30

1.4.2.1 Step-&-Scan Topography Sampling 31

1.4.3 Upgraded Prototype Tool 31

1.4.4 Synchronous Control System Development 34

1.4.5 Conclusions and Future Integration for In-line Applications 35

CHAPTER 2 - LITERATURE REVIEW OF MULTI-LAYER ROLL-TO-ROLL NANOMANUFACTURING 37

2.1 Unstable Webs 37

2.1.1 Web Models 40

2.1.2 Tension and Velocity Control 44

2.2 Existing Multi-Layer Alignment Methods in R2R Micro/Nanofabrication Systems 50

2.2.1 Scale Compensation 50

2.2.2 Self-Alignment Using Back-Substrate Exposure (SABSE) 53
2.2.3 Self-Aligned Inkjet Printing (SAP)..54
2.2.4 Self-Aligned Imprint Lithography (SAIL)..56
2.2.5 Summary 58
2.3 Vision-Based Alignment..59
2.3.1 Machine Vision 60
2.3.2 Diffractive Optics...64
2.4 Model-based Control 70
2.5 Modern Control...77
2.5.1 Summary 83
2.6 Measurement Challenges Towards Multilayer R2R Nanomanufacturing..........84
CHAPTER 3 – INITIAL R2R METROLOGY PROTOTYPE DESIGN 87
3.1 Web Handling Subsystem...88
3.2 sc-AFM Nanopositioning Subsystem 89
3.3 Proof-of-Concept Results 94
3.3.1 Open-loop Nanopositioning...95
3.3.2 Step-and-scan Operation...98
CHAPTER 4 - IMPROVED R2R NANOMETROLOGY TOOL DESIGN 102
4.1 Improved Web Handling and Tension Control..102
4.1.1 Improved Unwind/Rewind Spindle Design and Web Sensing 103
4.1.2 Improved Metrology Idler Roller..106
4.2 Improved Nanopositioning Sub-System..107
4.2.1 Structural Upgrades 108
4.2.2 Sensing upgrades 109
4.2.3 Power and Control Electronics Upgrades 110

CHAPTER 5 - SYNCHRONOUS CONTROL SYSTEM DEVELOPMENT 112

5.1 Advanced Motion Control for Moving Scans 112

5.1.1 H-infinity Control for Nanopositioning..114

5.1.2 Heuristically Optimized MIMO H-Infinity 116

5.2 Rotary Motor Field-Oriented-Control 121

5.3 High speed FPGA controller development...122

CHAPTER 6 - CONCLUSIONS AND FUTURE WORK..125

6.1 Conclusions...125

6.2 Future Work...126

6.2.1 Further System Improvements..126

6.2.2 Data Fusion 127

6.2.3 True In-line Operation 127

REFERENCES...130

APPENDIX A: LABVIEW CODE FOR FPGA CONTROL SYSTEM 143

APPENDIX B: UPGRADED METROLOGY ROLLER FABRICATION 155

Vita...159

List of Tables

Table 2.1: Summary of scale compensation methods utilized in R2R manufacturing systems 53

Table 2.2: Summary of self-aligned methods compatible with R2R processing 59

Table 2.3: Summary of machine vision-based methods utilized in current R2R systems. 64

Table 2.4: Summary of the performance of the vision-based methods with structured light or structured patterns which is compatible to R2R systems 70

Table 2.5: the performance of the vision-based method using mathematical modelling utilized in current R2R systems 77

Table 2.6: Summary of the performance of vision-based methods with advanced control or mechanisms utilized in current R2R systems 82

Table 3.2: Kerf corrected parametric and FEA values vs. as-fabricated flexure modules 94

List of Figures

Figure 1.1: Throughput vs. cost in R2R and wafer-based lithography [18] 18

Figure 1.2: Areas of research need in R2R nanomanufacturing..19

Figure 1.3: Examples of direct optical inspection in R2R manufacturing [20] 20

Figure 1.4: The *Airy Disk* converging from distinct (A) to indistinguishable, diffraction limited points (C) 22

Figure 1.5: Scatterometry system for R2R processing 23

Figure 1.6: Exemplary diffractometer for R2R nanoimprint lithography (A) and measurement results (B)..24

Figure 1.7: Basic schematic of a scanning electron microscope 25

Figure 1.8: Diagram of a basic atomic force microscope system.....................................26

Figure 1.9: Micrograph of ICSPI single-chip Atomic Force Microscope MEMS device with a US 25¢ coin in the background and major subsystems highlighted............28

Figure 1.10: Schematic diagram of cantilever deflection measurements systems for photodiode (A) and piezoresistive (B) based AFMs....................................28

Figure 1.11: Sub-system overview of proof-of-concept prototype tool 30

Figure 1.12: SEM micrograph (left) and sc-AFM step-and-scan result of polymeric, nanometer scale holes fabricated through R2R-capable interference lithography 31

Figure 1.13: Side-view of the upgraded tool's measurement sensor module (left) and micrograph from the on-tool optical monitoring system (right) with major sub-systems labelled. 32

Figure 1.14: Upgraded web rewind stand with major components highlighted................33

Figure 1.15: Upgraded air-bearing supported metrology idler roller 34

Figure 1.16: Operational modes of both the current prototype measurement tool (top left) and future in-line use cases (top right) for an in-line measurement module (bottom) based upon the knowledge gained from this work......................................36

Figure 2.1: Common shape distortions during processing of flexible substrates [34].......38

Figure 2.2: Web models in longitudinal dynamics (A) and lateral dynamics (B) [58], [59]41

Figure 2.3: Structure of distributed tension control system [57] 46

Figure 2.4: Schematic diagram of a large-area high-throughput roll-to-roll patterning system [40] 52

Figure 2.5: Fabrication steps of self-aligned organic field-effect transistor using back substrate exposure [108] 54

Figure 2.6: Self-aligned inkjet printing. A: Schematic of the SAP process. B: Schematic of the process to form a self-aligned gate (SAG) structure [116] 55

Figure 2.7: All inkjet-printed transistor process with self-aligned S/D [117] 56

Figure 2.8: Schematic diagrams of the SAIL process flow for fabricating TFTs [118]....57

Figure 2.9: Schematic of a TFT fabrication process by a self-aligned, imprint-assisted inkjet printing [125] 58

Figure 2.10: Scheme of self-aligned prism-OTFT fabrication process [126]....................58

Figure 2.11: Alignment system for the RRI process [129]...61

Figure 2.12: Register control in Lee's R2R printing system [105]...................................63

Figure 2.13: Principle of optical measurement method for web position in MD and CD [140] 66

Figure 2.14: Schema of the interferometric optical system [142] 67

Figure 2.15: The process of web planar position measurement using hybrid alignment marks printed on the two edges of the web [143]...69

Figure 2.16: Register models in MD (A) and CD (B); block diagram of MD (C) and CD (D) register controllers [147]..72

Figure 2.17: Schematic of a rotogravure print unit with two print cylinders using CRC strategy for registration [156] 75
Figure 2.18: Dual state feedback control architecture augmented with NOILC [161]......77
Figure 2.19: (A) Working principle of the plate-to-plate gravure offset printing system; (B) Schematic diagram of roll-to-roll gravure offset printing equipment [162].79
Figure 2.20: Schematic of (A) process flow of overlay alignment, and (B) the R2R processing of substrate (side view) [163] 80
Figure 2.21: Schematic of the successive chucking mechanism [164]..............................81
Figure 2.22: (A) Configuration of the register control system using the AMBR; (B) Block diagram of the MD register error controller using the AMBR [120] 82
Figure 2.23: Silicon wafer manufacturing overlay requirements and process corrections per lot with respect to time...84
Figure 2.24: Basic hybrid metrology schema involving three tools of varying precision and throughput 86
Figure 3.1: CAD rendering of initial tool design with a proposed throughput-maximized configuration of parallel sc-AFM probes...87
Figure 3.2: Diagram of the Geometric Layout of the Web Handling Sub-system showing unwind and rewind diameters, angular velocities, web path, and the location of scanning 88
Figure 3.3: Initial prototype unwind/rewind stand assembly..89
Figure 3.4: Flexure mechanism geometric layout..91
Table 3.1: Double parallelogram flexure mechanism design variables 91
Figure 3.5: FEA simulation of out of plane flexure resonant modes................................92
Figure 3.6: Kerf, or vertical taper, in the as-fabricaed flexure beams 93
Figure 3.7: FEA Simulation of static maximum range and stiffness simulation of Z-axis (left) and X-axis (right) linear flexure bearings..93
Figure 3.8: Photographs of the initial concept prototype with major sub-systems labeled95

Figure 3.9: Initial experimental power electronics and control apparatus........................95
Figure 3.10: X- and Z-axis open loop noise floor in a single DPFM monolith................96
Figure 3.11: Cross-coupling ratio between independent axis within an individual flexure monolith 96
Figure 3.12: Experimental system ID Bode response of X- and Z-axis DPFM flexure bearings 97
Figure 3.13: Photograph and SEM micrographs of the nanostructures which make up the wing of the queen butterfly 98
Figure 3.14: Detailed view of sc-AFM scans of the wing of a queen butterfly................99
Figure 3.15: sc-AFM scans of gold nanoposts on a polycarbonate web 100
Figure 3.16: SEM micrograph (left) and sc-AFM result of R2R-capable interference lithography Nanopattern 101
Figure 4.1: Schematic outline of quasicontinuous scanning framework 102
Figure 4.2: Super precision class back-to-back angular contact ball bearing cartridge...103
Figure 4.3: Upgraded rewind stand with major components labeled 103
Figure 4.4: Upgraded unwind stand with major components labelled 104
Figure 4.5: Schematic diagram of a typical brushless DC motor (A), a slotless DC motor (B) and the difference in torque ripple under load between the two motor confirgurations (C)...105
Figure 4.6: Upgraded air-bearing supported metrology idler roller 106
Figure 4.7: Side-view of the metrology module in the upgraded prototype (left) and view from the tool observattion camera (right) 107
Figure 4.8: Structural upgrades to the sc-AFM positioning sub-system 108
Figure 4.9: Open loop noise levels in all three measured axis with the improved interferometric distance sensors...109
Figure 4.10: Sensor heads and mirror targets for the interferometer distance sensors....109
Figure 4.11: Upgraded system power amplifiers and control electronics 110

Figure 4.12: Upgraded DC power supplies, control relays, and protective circuitry 111
Figure 5.1: Schematic of single-axis MIMO model of sc-AFM gantry positioning system112
Figure 5.2: Open loop frequency response function and grey-box model for MIMO system of X-axis sc-AFM positioner...113
Figure 5.3: Control system block diagram for (a) decoupled MIMO PI control and (B) H-Infinity control 114
Figure 5.4: Flow-chart for the proposed "H-Optometry" algorithm...............................116
Figure 5.5: Optimization goals for the applied H-Optometry process............................116
Figure 5.6: Pareto optimal solution spaces after the initial *Direct Multi-Search* algorithm (top) and the final interaction of the NSGA-II algorithm (bottom) with the candidate controllers chosen by the operator filled with purple 118
Figure 5.7: Bode response (top) and LTI simulated system performance of final iteration of H-Optometry generated controller candidates (bottom) 119
Figure 5.8: Magnitude of the frequency response of the final h-optometry closed loop system in comparison to decoupled pi control and the open loop system 120
Figure 5.9: Traditional BLDC motor commutation (left) and the different coordinate reference frames of Field Oriented Control (right)....................................121
Figure 5.10: Control block diagram for FOC algorithm applied to rotary motors using a linear amplifier...122
Figure 5.11: Cascaded second order section structure to efficiently represent higher order transfer functions 123
Figure 6.1: Upgraded system state-machine operation flow chart (left) and trimetric view of the system in the NASCENT cleanroom metrology bay 126
Figure 6.2: System instrumentation future error compensation schema.........................127
Figure 6.3: Exemplary state-of-the-art R2R nanofabrication tool with design considerations for in-line metrology 128

Figure 6.4: Operational modes and applications of the current prototype tool as-designed (left) and future modular applications for true in-line process metrology ..128

Figure 6.5: Schematic diagram of proposed modularized sc-AFM in-line inspection system 129

Figure A1: Thermocouple, Interlock, Relay, and Thermistor measurement and control loops. 143

Figure A2: Laser distance sensor and air bearing pressure sensor analog input and scaling loop 143

Figure A3: Unwind and rewind stand encoder measurement loops 144

Figure A4: Unwind/rewind motor field oriented control and signal analog output loops.145

Figure A7: Laser interferometer high speed serial link position and velocity measurement and calculation loops 148

Figure A8: Implementation of high speed serial link interferometer digital communication protocol Figure A9: Optical angular encoder high speed 1 MHz analog input module and encoder count interpolation loops 149

Figure A10: Nanopositioner datalogging loops. 151

Figure B1: Upgraded idler roller fabrication showing bonding of stainless steel hubs and assembled roller before final precision surface grinding 155

Figure B2: Precision grinding of air bearing journals and CRFP body of upgraded idler roller 156

Figure B3: Upgraded idler roller after precision surface grinding 157

Figure B4: Final coating of idler roller CRFP body with acrylic resin based clear coat.158

CHAPTER 1 - INTRODUCTION

The promise of roll-to-roll (R2R) nanofabrication is to bring a class of products which match or exceed performance of counterparts manufactured with traditional silicon wafer or glass panel based substrates while possessing unique mechanical properties and significantly lowered processing cost [1]–[6]. From functional coatings, optical devices, energy materials, and even compute, logic, or memory, the push for faster, cheaper, and more tightly integrated products has driven intense research focus on enabling R2R fabrication techniques which can successfully make the jump from benchtop experimentation to high volume manufacturing (HVM) [7]–[14]. While successful lab- and pilot-scale fabrication has been demonstrated, there exists a key barrier to further adoption and development of these manufacturing techniques specifically for nanometer scale patterns — the metrology problem [15]–[17].

Two of the most critical areas to profitable HVM of nanofeatured products and devices are yield and throughput. Figure 1.1 demonstrates the throughput and processing cost advantage compared to wafer based manufacturing due to these factors [18]. While R2R processes typically excel in terms of throughput compared to traditional, silicon wafer based manufacturing processes, *make it by the mile* is only a successful strategy if enough of the final product meets quality standards. Figure 1.2 shows the major areas of research need to enable high volume R2R manufacturing identified by the National Institute of Standards and

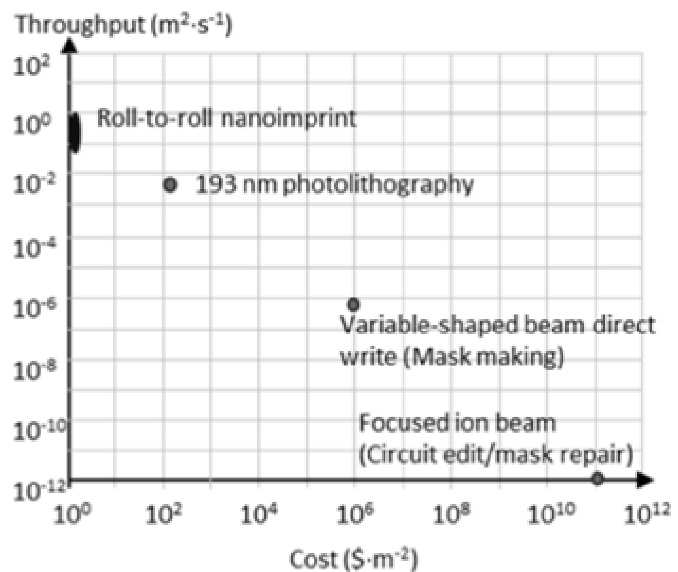

Figure 1.1: Throughput vs. cost in R2R and wafer-based lithography [18]

Technology. In practice, achieving viable yields is an area of significant difficulty, and as such the task of quickly, precisely, and non-destructively measuring fabricated nanopatterns is an area of significant research interest [16], [19].

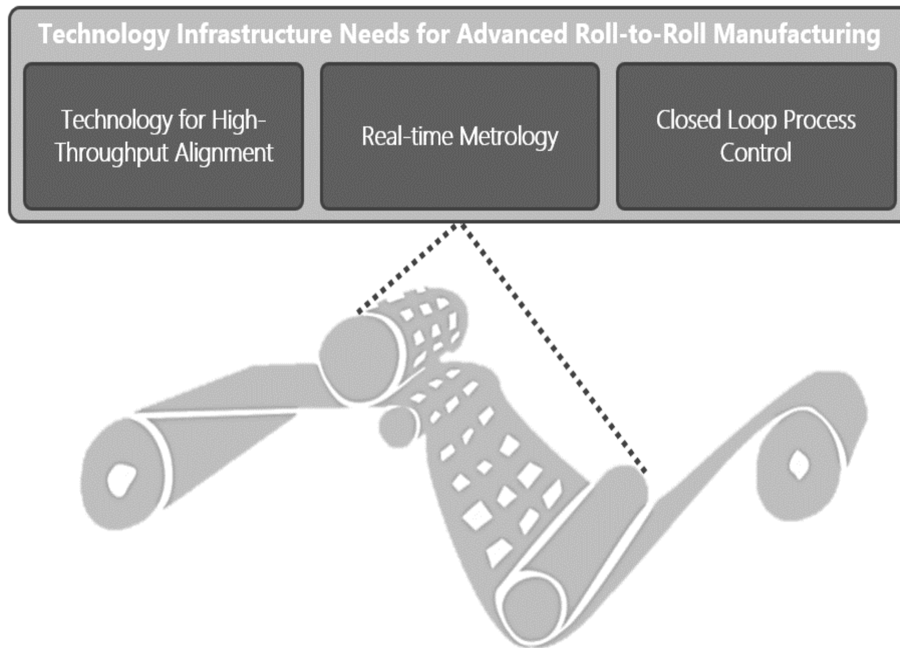

Figure 1.2: Areas of research need in R2R nanomanufacturing

While a significant proportion of current art in metrology for R2R nanopatterning is relatively recent, with most occurring within the last decade or so as could be expected of a nascent manufacturing technology, several approaches have been investigated and shown to be effective at specific, and often disparate, measures of performance and efficacy. The techniques vary by the physical phenomena which they use to measure fabricated features in addition to throughput, compatibility with in-line measurement in R2R HVM, and measurement precision. Further, despite the overarching basis of many of these approaches originating from years of development for similar tools in the wafer semiconductor fabrication industry, extension to R2R nanomanufacturing remains a daunting, and often insurmountable, challenge.

1.1 Photonic imaging Methods

A plurality of existing research investigating this critical gap of nanometrology capability in R2R manufacturing utilizes optical methods to acquire information regarding the geometry, topography, defectivity, planarity, various critical dimensions, or a combination of these qualities of the flexible, nanopatterned substrate. This process is usually thought of in terms of three steps – image acquisition, processing, and defect analysis [20].

1.1.1 Direct Optical Inspection

Optical process inspection, which typically revolves around measuring spatially resolved light intensity or spectrum to form a three dimensional dataset, is generally thought as encompassing commonly used photonic methods such as micrography, photography, and spectral imaging. These offer a means of directly measuring certain aspects of as-fabricated features on a substrate. Using optical magnification lensing systems, this approach can generally be extended from macro- and mesoscale imaging to resolve features at or just below the micrometer scale. Further, these inspection approaches have the advantage of collecting data in a generally parallel fashion – as even rolling shutters are orders of magnitude faster than overall sensor sampling rate.

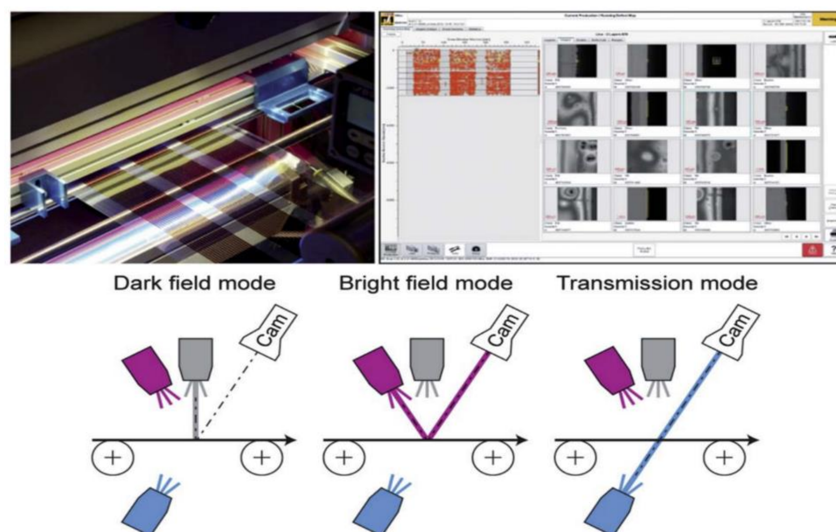

Figure 1.3: Examples of direct optical inspection in R2R manufacturing [20]

The most basic direct inspection system will consist of a light source, the R2R web, and an image sensing camera [21]. Figure 1.3 outlines the three most common methods of direct optical inspection in R2R fabrication, in this case for defect detection in the processing of organic photovoltaic products. Here images are acquired, processed to maximize contrast, and analyzed for any defects. Taken together, the advantages of direct optical inspection have led it to be the most common type of process metrology for a plethora of R2R manufacturing processes, however, fundamental physical limits severely hamper usability when critical dimensions or minimum feature sizes dip below roughly 0.5 μm.

1.1.2 Diffraction limits and The Airy Disk

Despite the evident set of advantages direct optical inspection offers for an application such as process measurement in R2R nanomanufacturing, the drawback comes in the limits to any optical system's ability to resolve sub-wavelength, nanoscale features. This effect was first described quantitatively by Earnest Abbe in Eq. 1.1 where *d* is the minimum resolvable distance, λ the wavelength of light used, and *NA* the numerical aperture of the optics system used to measure the sample [22].

$$d = \frac{\lambda}{2NA} \tag{1.1}$$

In addition to the diffraction issue, when practically implementing a direct optical inspection system requires the consideration of another quality of the measured images – contrast.

While often idealized to a single spot of illumination with uniform intensity, each point is more accurately represented by an airy disk. This feature, which is generally approximated by a gaussian distribution of intensity with respect to lateral distance, presents the issue of contrast as the more stringent measure of minimum resolvable feature size. The diameter of the airy disk

when measured by a small image sensor at infinite focal length is often approximated by Eq. 1.2 Where *d* is airy disk diameter, and *f/#* the f number of the lens.

$$d = 2.44\lambda * (f/\#) \qquad (1.2)$$

Figure 1.4A shows a simulation of two such airy disk where the color of the image corresponds to normalized intensity, with white being the highest measure and black the lowest. Subsequently, in Figs. 1.4B and 1.4C, as the two airy disks draw closer, there exists a separation distance, *ΔL,* where the two individual airy disks can no longer be seen distinct of one another. This limit in contrast, first described by Lord Rayleigh in the Rayleigh criterion states:

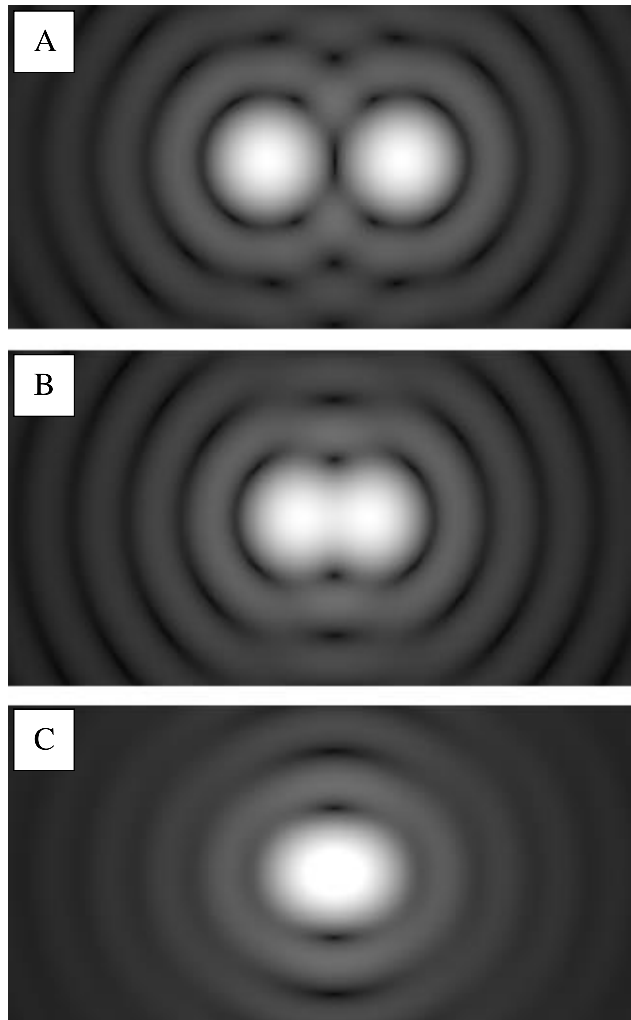

Figure 1.4: The *Airy Disk* converging from distinct (A) to indistinguishable, diffraction limited points (C)

Two point sources are regarded as just resolved when the principal diffraction maximum of the Airy disk of one image coincides with the first minimum of the Airy disk of the other. If the distance is greater, the two points are well resolved and if it is smaller, they are regarded as not resolved.

Rayleigh's equation relates an optical system's focal length, *f*, wavelength, and the diameter of the lens' aperture, *D*, to spatial resolution *d* as shown in Eq. 1.3 [23].

$$d = 1.22\frac{f\lambda}{D} \tag{1.3}$$

When utilizing light within the visible spectrum, these physical effects will prevent inspection of any patterns with a minimum feature size below roughly 300-500 nm, severely limiting the use of direct optical inspection in advanced R2R nanopatterning.

1.1.3 Indirect Optical Inspection

To extend the usefulness of optical inspection based measurement, systems have been developed which leverage secondary optical effects, often in the frequency or spectral domain, to accurately measure critical dimension or other features significantly below the traditional diffraction and airy disk limits. The two most typically implemented system architectures are scatterometry and diffractometry. These methods rely on the diffraction or scattering of, often, visible or ultraviolet

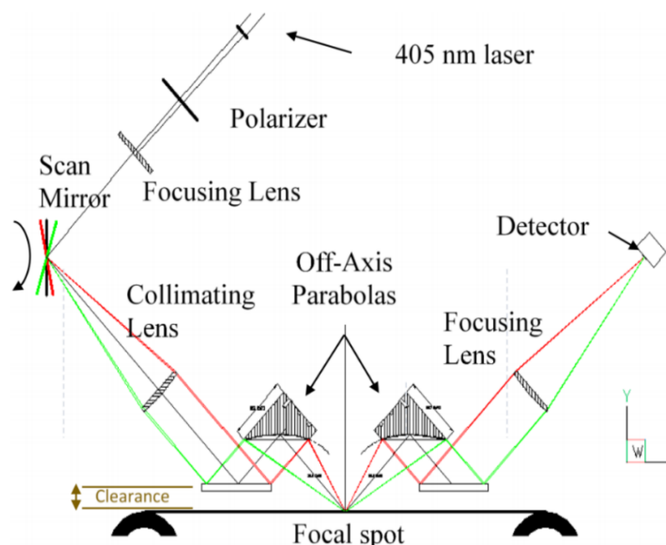

Figure 1.5: Scatterometry system for R2R processing

light to infer critical dimensions or other aspect of collections of nanoscale features based upon an offline library of calibration experiments. In wafer based manufacturing, hyperspectral scatterometry has been shown to achieve very accurate results and has become a staple of HVM [24], [25]. Critical dimensions such as feature diameter or width, pitch, taper, and defectivity can all be measured in a small amount of time [26]. An example of a R2R implementation of such a scatterometry system which could be used for in-line process control is shown in Figure 1.5 [27]. In addition to fabricated features, it can also be important verify degradation, or the lack thereof, of master patterns such as imprint rollers or templates. A diffractometry system which can measure pattern line width on a master template in real time within a R2R nanoimprint lithography manufacturing tool is shown in Figure 1.6. The advantage of this approach is the sampling speed and throughput achievable is often on the same order of magnitude as traditional direct optical inspection, while the achievable minimum measurement resolution is significantly smaller than that of diffraction limited optical systems. However, the drawbacks of this approach center on basis of indirect measurement itself as, inherently, only collections of features can be measured – no individual sub-diffraction structure or pattern can be coherently resolved. This limits usefulness

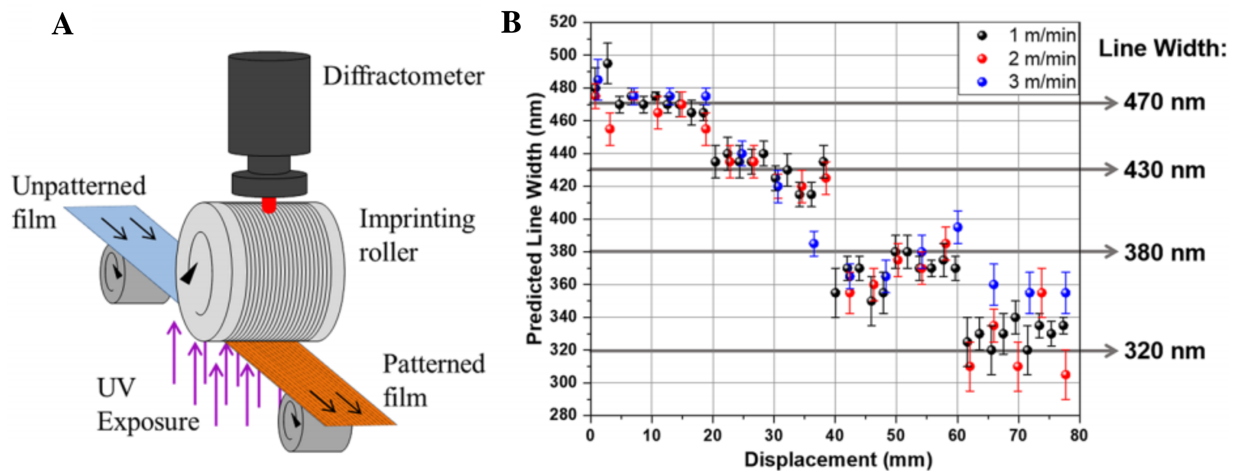

Figure 1.6: Exemplary diffractometer for R2R nanoimprint lithography (A) and measurement results (B)

for tasks such as defect root cause analysis, and, moreover, requires the time consuming and computational expensive task of building a measurement library with which to calibrate raw diffractometer or scatterometry data to critical dimension or feature characteristic [26]. Future R2R nanomanufacturing will almost certainly require a high level of integration with various diffraction based measurement (DBM) techniques, however, DBM alone cannot fulfill all measurement requirements for effective process control, and thus financially viable R2R nanopatterning.

1.2 ELECTRON BEAM METHODS

One of the most widely utilized methods for nanometer scale inspection is scanning electron microscopy (SEM) [28], [29]. Built upon the principles of transmission electron microscopy (TEM) first pioneered by Earnest Abbe, and later recognized to exceed the resolution of optical microscopy due to the de Broglie wavelength of incident high energy electrons, the SEM furthered the principle of TEM by combining backscatter and secondary electron detectors with a raster scanning of the incident electrons to spatially resolve structures [30]–[32]. The primary advantage to this approach is that it has the ability, depending on the specific tool and metrology goals, to resolve critical dimensions of a few nanometers or below. However, this performance comes at the cost of measurement speed and the need to pull hard vacuum for measurement to occur, as can be seen in Figure 1.7. Significant research effort has been

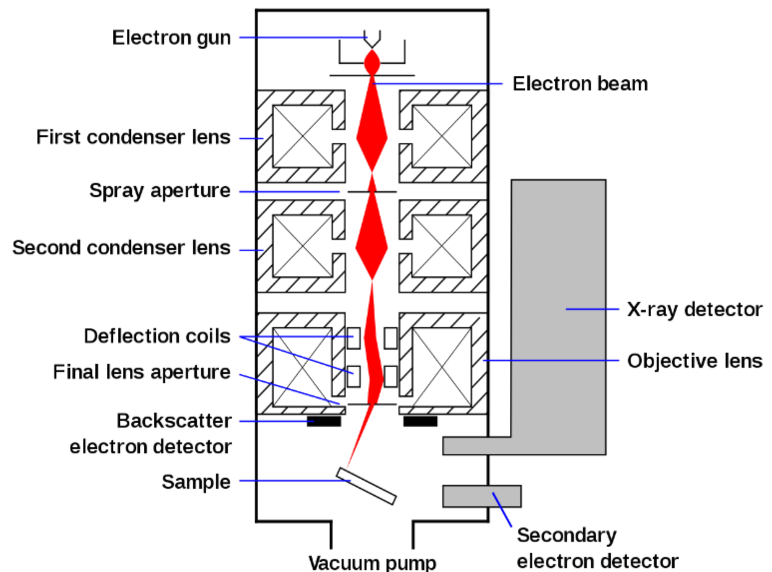

Figure 1.7: Basic schematic of a scanning electron microscope

dedicated to improving the throughput of these tools, and systems employing multiple parallel beams, numbering into the hundreds, has been successfully used to improve process control capabilities in traditional wafer based semiconductor manufacturing by extending the single "exposure" field of view beyond 200 µm while maintaining resolution [33]. Despite these advantages, integrating SEM based metrology into a process control scheme for R2R nanomanufacturing has proven exceedingly difficult due packaging and environmental requirements. Dimensional SEMs also often require hard vacuum and a grounded sample – commonly necessitating that R2R samples must be destructively removed from the web for measurement. Moreover, the limited SEM exposure speed compared to R2R web velocities in addition to limited field of view further exacerbates the issue of applying SEM in an in-line fashion.

1.3 TIP-BASED METHODS

A more recent development than electron beam methods, the atomic force microscope (AFM) essentially combines the principles of a scanning tunneling microscope and a surface profilometer to raster scan a surface and utilize a very sharp tip attached to a thin cantilever positioned in the vertical direction to maintain either consistent contact or a particular separation distance [34]. Typically, these systems employ a laser system to measure cantilever deflection and a piezoelectric XY stage to scan the tip over the sample surface in a rasterized fashion as is shown in Figure 1.8 By

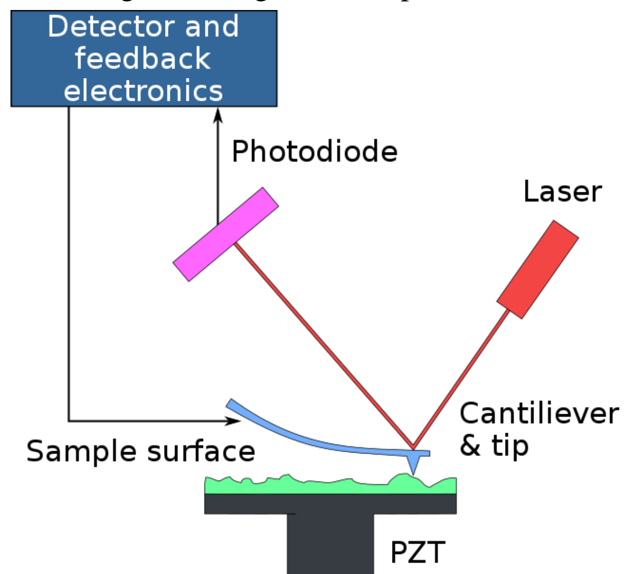

Figure 1.8: Diagram of a basic atomic force microscope system

a simple calibration of cantilever deflection, and thus measured force, to a sample artifact with known height, the measured sample topography can be determined from a map of cantilever deflection values with respect to sample stage position. This microscopy method has a significant advantage in minimum resolvable feature size as vertical resolution has been demonstrated below 1 nm and lateral resolution of the tool is generally only limited by the positioning accuracy of the XY motion stage used and the radius and aspect ratio of the sharpened tip, depending on the exact geometry of the structures to be measured. However, like SEM methods, the resolution of the raster scanning is a direct tradeoff with measurement throughput and samples are almost always required to be taken out of line for measurement – an inherently destructive process in R2R manufacturing.

1.3.1 Single-Chip Atomic Force Microscope

Recent advancements in micro-electro-mechanical systems (MEMS) design and fabrication have led to the commercial development of a wholly new type of AFM. The MEMS-based AFM is monolithically integrated on a single silicon die and packaged with all necessary sensing and actuation systems. This AFM-on-a-chip, or single chip AFM (sc-AFM), combines a high performance, thermally actuated MEMS flexure stage for positioning the cantilever and tip in the XY plane and a vertical bimorph stage to position the cantilever in the Z axis [35]–[38]. Figure 1.9 shows a micrograph of an sc-AFM with the motion stages and cantilever labeled [39]. The MEMS approach to fabrication also enables low-cost and easy integration of a piezoresistive sensor in stress concentration point embedded in the pivot for the cantilever itself, negating the need for bulky and expensive optical systems to measure tip deflection.

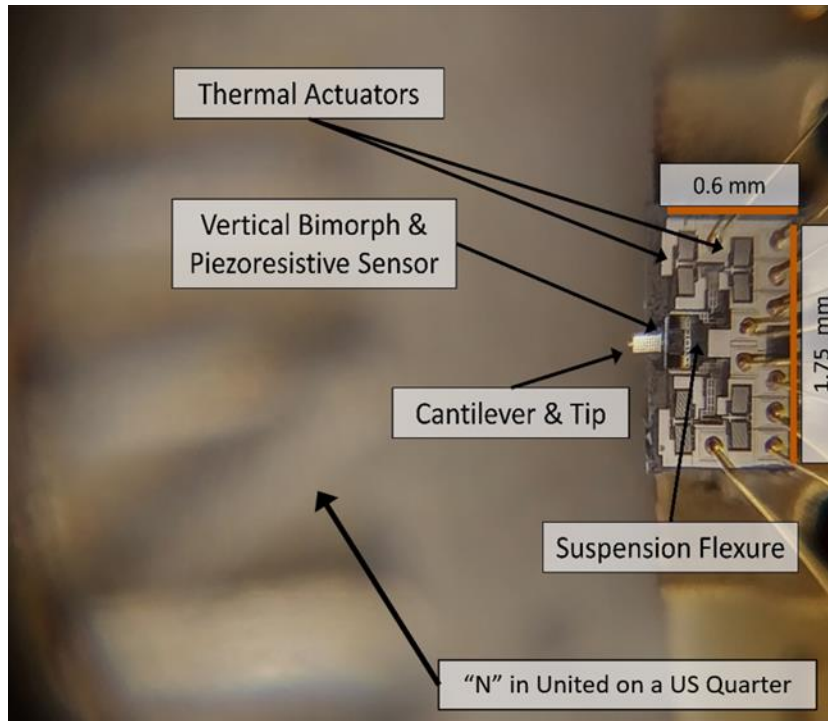

Figure 1.9: Micrograph of ICSPI single-chip Atomic Force Microscope MEMS device with a US 25¢ coin in the background and major subsystems highlighted

A comparison of these two tip sensing methods is shown in Figure 1.10A and 1.10B respectively. As such, this MEMS package has the distinct advantage of a combining a mm-scale overall package with a measurement precision that is on the same order of magnitude of more traditional table-top AFMs. Additionally, by positioning the cantilever in lieu of the sample itself, the sc-AFM can be used in a much less invasive manner compared to lab-scale tools, and at a

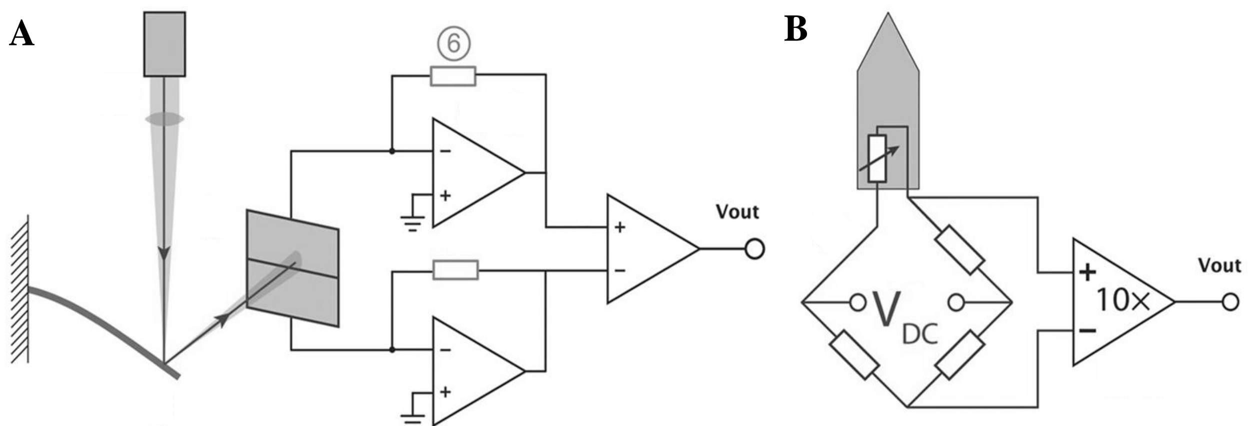

Figure 1.10: Schematic diagram of cantilever deflection measurements systems for photodiode (A) and piezoresistive (B) based AFMs

fraction of the cost. Moreover, due to the scaling effects inherent to MEMS mechanisms, notably the significantly lowered weight of the positioned payload and thermal mass of the device, the sc-AFM is much more tolerant of both mechanical vibrations and nonequilibrium thermal conditions than tabletop tools.

1.4 Thesis Overview

This dissertation presents a proof-of-concept prototype for a tip-based tool aimed at implementing a novel measurement framework for sampling nm-scale topography on flexible webs fabricated in a R2R manner. The measurement is accomplished through the implementation of a MEMS-based sc-AFM probe which is positioned in the vertical and web-directions by means of a linear flexure-bearing based positioning system and actuated by linear Lorentz force actuators. In the case of the proof-of-concept, a web sample is loaded onto unwind and rewind core chucks and the prototype conveys the web in a manner as to enable sequential sampling. This system embodies a wholly unique capability for nanometer-scale direct measurement of R2R fabricated features without time consuming and disruptive destructive sample preparation.

The remainder of this thesis is organized as follows:

1.4.1 The State of Advanced, Multi-layer R2R Nanomanufacturing

Chapter 2 presents a comprehensive literature review of relevant, state-of-the-art technologies aimed at the handling of inherently unstable thin webs in addition to the community's efforts towards multi-layer fabrication. As the functional objective of the prototype tool is centered on applications to future advanced flexible electronics, the limits of current multi-layer R2R micro- and nanofabrication and efforts to minimize overlay errors in manufacturing present the most likely use-case for the proposed measurement framework. This chapter encompasses not only the challenges in modeling and controlling flexible webs for feature registration, velocity, and tension,

but also shows comparison between achieved overlay error of a variety of previously demonstrated fabrication techniques and research tools.

1.4.2 Proof-of-Concept R2R Tip-based Measurement Prototype

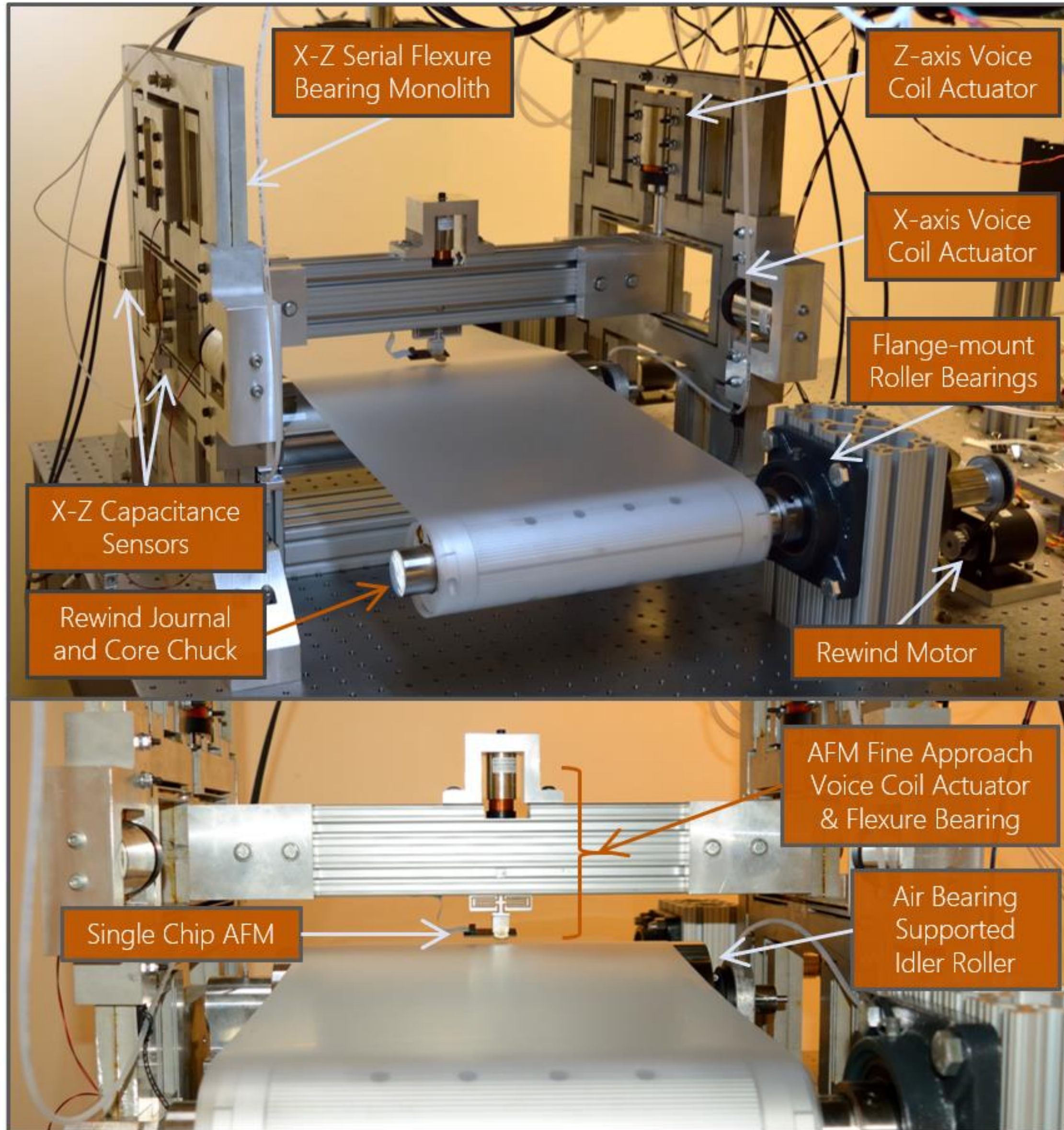

Figure 1.11: Sub-system overview of proof-of-concept prototype tool

Chapter 3 presents the design and fabrication of the initial prototype measurement tool, as shown in Figure 1.11, including the parametric process used to design the double parallelogram flexure mechanisms for probe positioning, dynamic response of the flexure positioners, and open

loop performance in the vertical (Z) and web direction (X) axis. Further, this chapter details the design and operation of the web handling subsystem in this initial prototype in addition to sc-AFM measurement results.

1.4.2.1 Step-&-Scan Topography Sampling

The step-and-scan operation of the initial prototype is demonstrated on a variety of test artifacts, including an exemplary nanopattern created through interference lithography [12], which

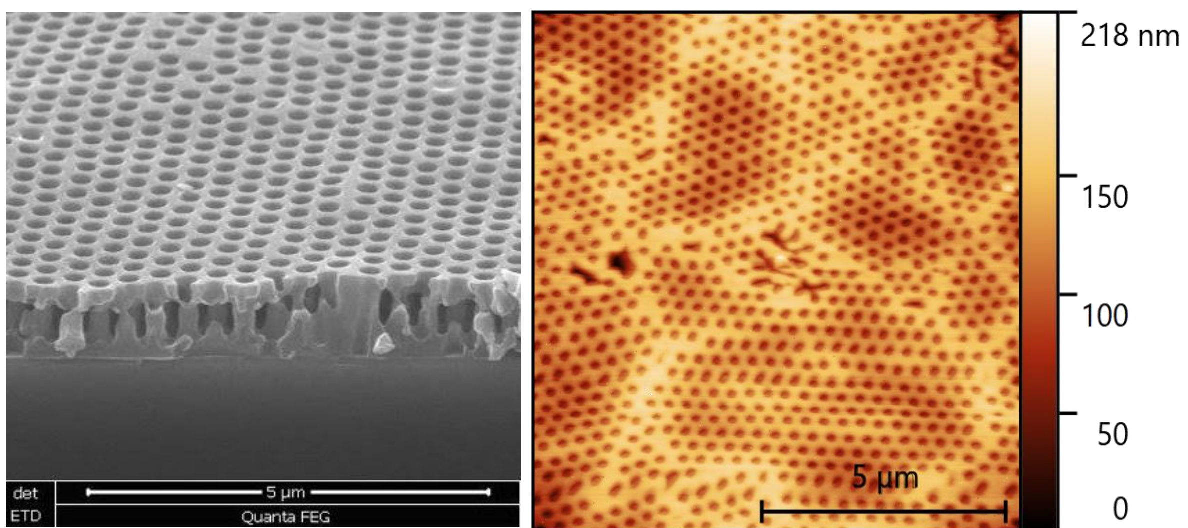

Figure 1.12: SEM micrograph (left) and sc-AFM step-and-scan result of polymeric, nanometer scale holes fabricated through R2R-capable interference lithography

is representative of the challenges in many R2R applications for nondestructive evaluation of nano-scale height and lateral feature dimensions and a soft, polymeric structure. The results from this scanning, contrasted with an SEM micrograph from a calibrated table-top tool, is shown in Figure 1.12.

1.4.3 Upgraded Prototype Tool

Chapter 4 presents a series of upgrades undertaken to advance the capabilities of the initial proof of concept prototype such that both positioning and web-handling sub-systems may achieve a performance level which will enable not only the static step-and-scan operation previously

demonstrated, but also the ability to measure web topography without halting the conveyance of the web through the tool. In order to accomplish this, improvements were made to the gantry which support's the sc-AFM probe, measurement and sensing capabilities, and a wholly new unwind and rewind web-handling sub-system.

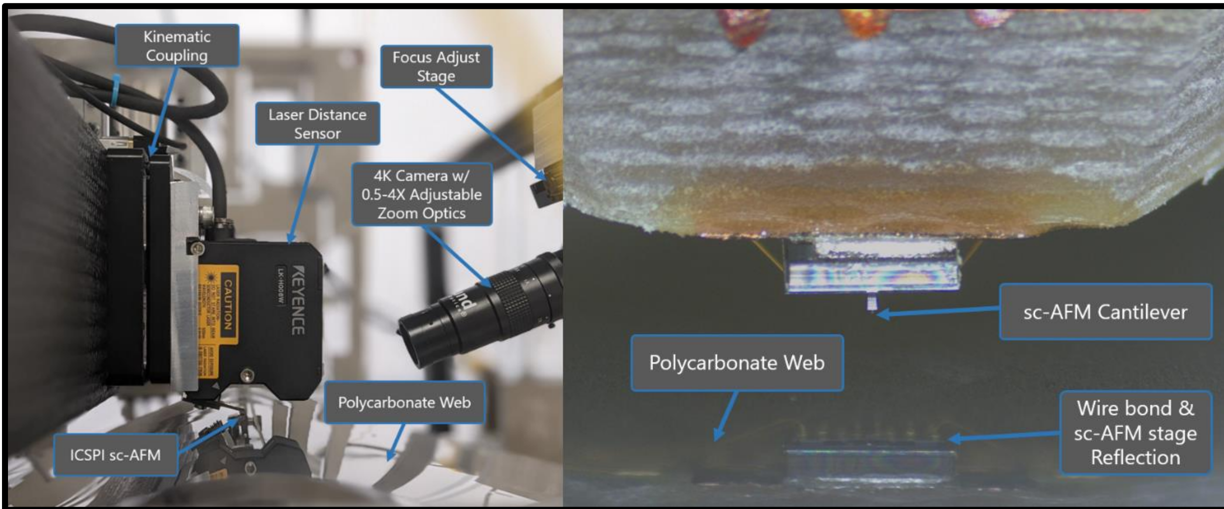

Figure 1.13: Side-view of the upgraded tool's measurement sensor module (left) and micrograph from the on-tool optical monitoring system (right) with major sub-systems labelled.

Improvements to the measurement and sc-AFM positioning system include custom fabricated, high specific stiffness carbon fiber reinforced polymer (CRFP) composite structure, probe monitoring imaging system, and a high speed, sub 5 nm precision laser triangulation distance sensor for substrate tracking during moving scans. These upgrades are shown in Figure 1.13. Further, both unwind and rewind stands were upgraded with improved mechanical structure, super precision class rolling element bearings, high specific stiffness CRFP structure and slotless, brushless DC motors for smooth velocity and torque control performance. Further, 100 nm repeatability laser distance sensors were added to measure roller diameter in real time in order to accurately convert requested linear velocity and web tension into motor control parameters for angular velocity and applied torque. The upgraded rewind stand is shown in Figure 1.14.

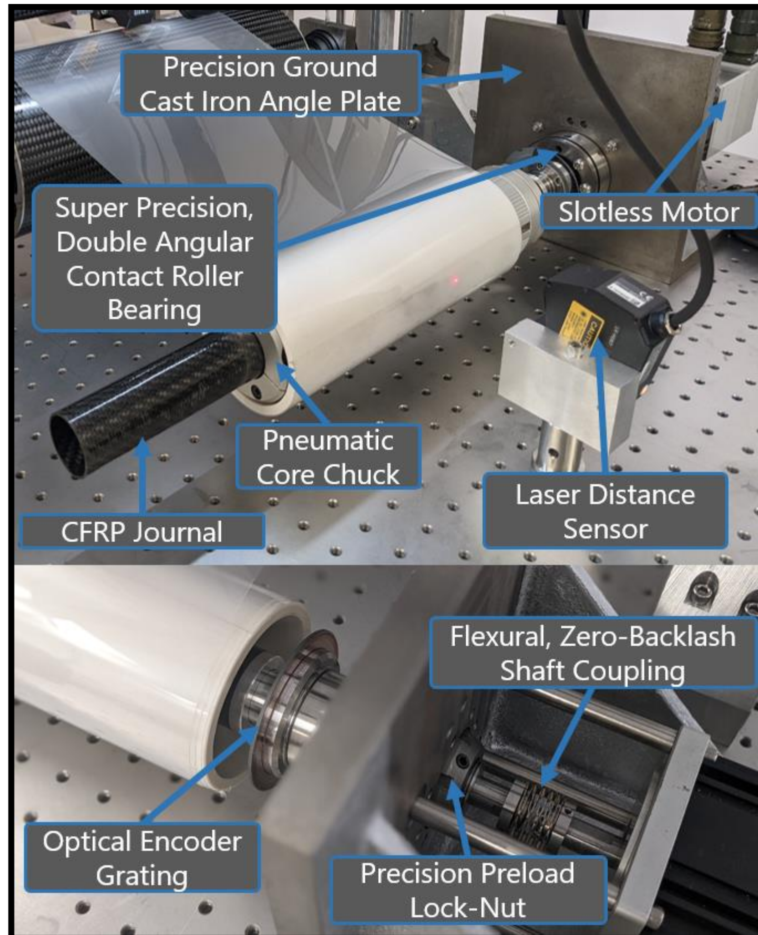

Figure 1.14: Upgraded web rewind stand with major components highlighted

Lastly, the idler roller on which sc-AFM scanning takes place was upgraded from a 100 mm diameter stainless steel roller with a mass of ~6.33 kg to a 150 mm diameter CRFP idler roller with a mass of less than 2 kg. This significantly reduces the angular moment of inertia of the idler roller minimizing the chance of slip due to the friction force between roller and web required to change the speed of the roller. A photograph of the new roller in addition to the air bearing mounting blocks is shown in Figure 1.15. By and large, the CRFP structures in the upgraded tool both roughly double the specific modulus – the Young's modulus normalized to density - of the aluminum and steel structures in the initial prototype and reduce the coefficient of thermal expansion of these sensitive metrology frames anywhere from 10x to 20x compared to steel and

aluminum respectively which reduce measurement uncertainty due to environmental control errors.

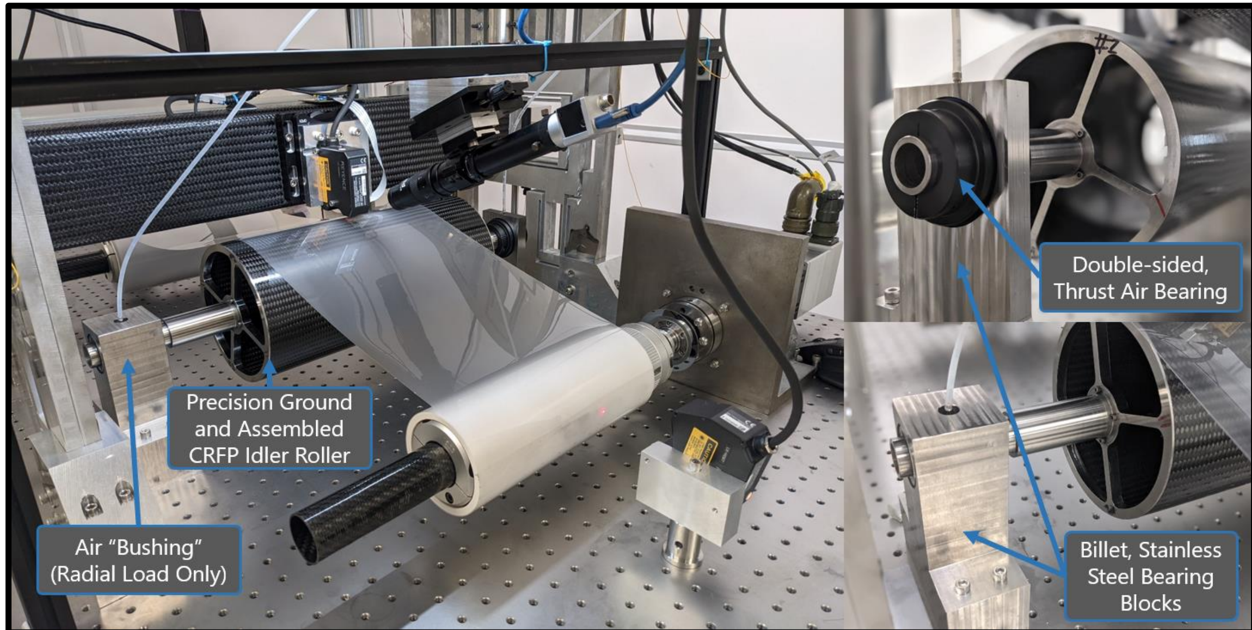

Figure 1.15: Upgraded air-bearing supported metrology idler roller

1.4.4 Synchronous Control System Development

Chapter 5 presents the design of a robust, higher-order control system generation strategy through heuristic optimization of H-Infinity based controller synthesis for the multiple-input-multiple-output (MIMO) sc-AFM positioning stage and advanced vector based field oriented control for maximum performance of the rotary slotless motors in the web handling sub-system. Lastly, design of a field programmable gate array (FPGA) based deployment of the higher-order positioner control system by means of cascaded second order section (SOS) systems and synchronous control of unwind and rewind rotary motors and the sc-AFM positioning stage is detailed, with maximum propagation delay between various components of the control systems of 80 ns.

1.4.5 Conclusions and Future Integration for In-line Applications

Chapter 6 details the contributions of this thesis and future work and applications with feasibility demonstrated as a direct result of the advances presented in this dissertation. Figure 1.16 outlines the current operational modes of the prototype tool (top left) which serve mainly to aid in the tuning and development of new processes, or the research and development required to create new fabrication tools in a batch fashion – in that each roll of material to be measured must be individually loaded on to the detached sc-AFM measurement prototype. However, the true ceiling of the value this metrology framework demonstrates lies not in the piecewise operation of the current tool but continuous in-line sampling as in Figure 1.16 (top right). With such an approach, sc-AFM measurement modules following the mold of the tool architecture developed in this dissertation can be "dropped in" between fab and rewind modules, or between multiple fab steps, as shown in Figure 1.16 (bottom). The end result of such an approach is a quasicontinuous measurement process which may sample in a line-scan fashion many times per minute and automatically report nanometer-scale topography data to a centralized fab control algorithm such that informed process control decisions may be made based off both existing direct optical and diffractive optical methods and direct topography information provided by the sc-AFM system.

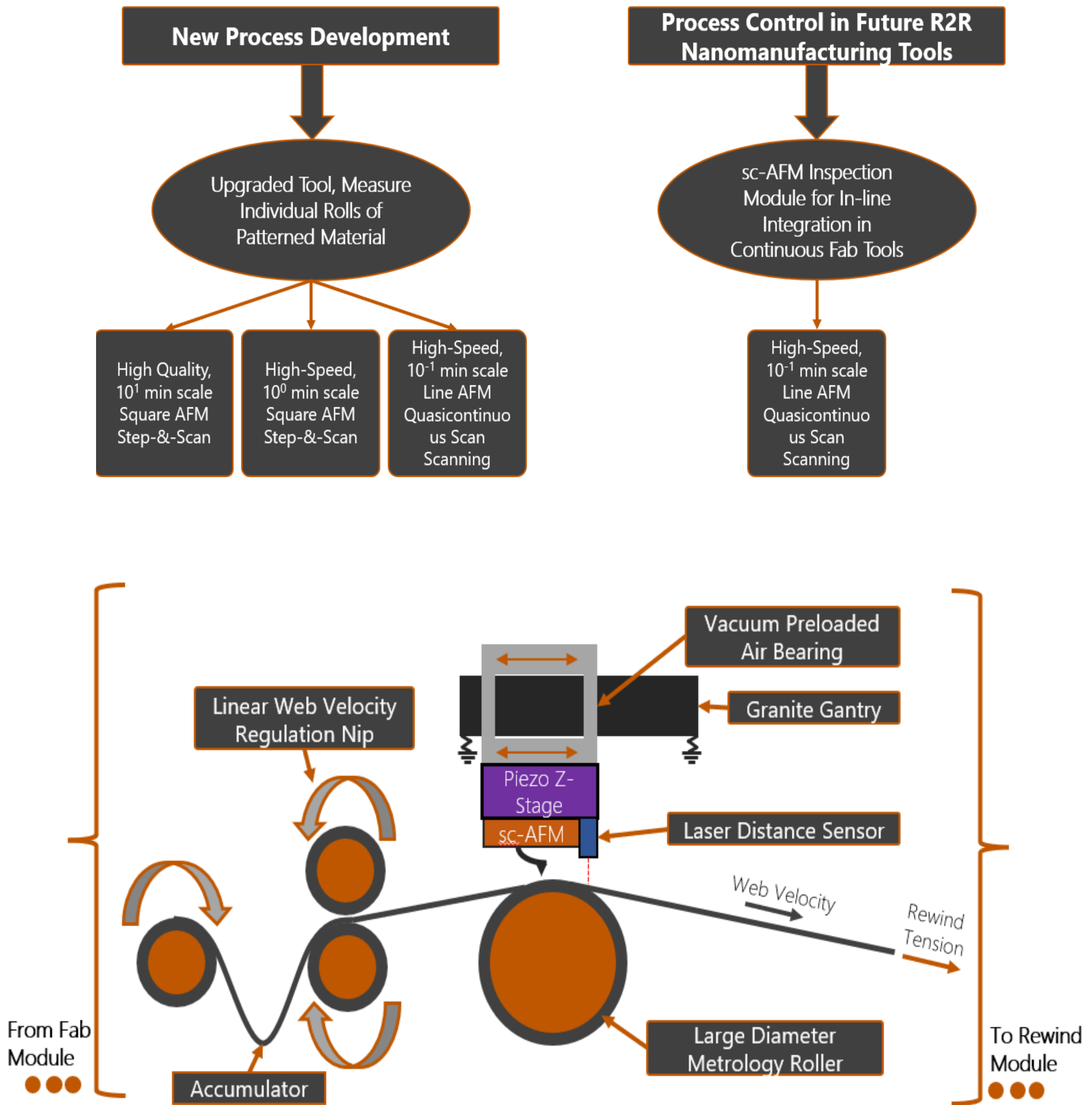

Figure 1.16: Operational modes of both the current prototype measurement tool (top left) and future in-line use cases (top right) for an in-line measurement module (bottom) based upon the knowledge gained from this work.

CHAPTER 2 - LITERATURE REVIEW OF MULTI-LAYER ROLL-TO-ROLL NANOMANUFACTURING

In order to best understand the needs and requirements of future R2R HVM of advanced, nanofeatured products, it is critical to have a broad comprehension of the unique challenges and current state-of-the-art approaches in, specifically, multi-layer manufacturing with micron and sub-micron overlay error. As any logic or memory integrated into flexible electronic devices will require multiple fab steps, the process metrology required to push overlay error down to a level which allows for this type of advanced manufacturing at volume, and more closely resembles overlay errors achieved in wafer based manufacturing, is the most prominent potential application of the measurement framework presented in this thesis. Firstly, the ways in which flexible webs may be modeled and simulating is key to understanding the requirements for subsequent protype web handling subsystems.

2.1 UNSTABLE WEBS

Unlike manufacturing with rigid substrates, webs are much more unstable during both transportation and manufacturing. Here we define a web as a continuous, and typically meter-scale in length, thin sheet of a material, often a polymer film or metal foil, such that the web is mechanically very flexible [40]. In micro- and nanofabrication, roll-to-roll web systems are susceptible to sudden disturbances due to the inherent compliance of these substrates. The flexible web can be easily deformed by mechanical tension or changes in temperature and the properties of the web may also change under different environmental factors. Figure 1 shows the typical substrate distortions which can occur in R2R systems.

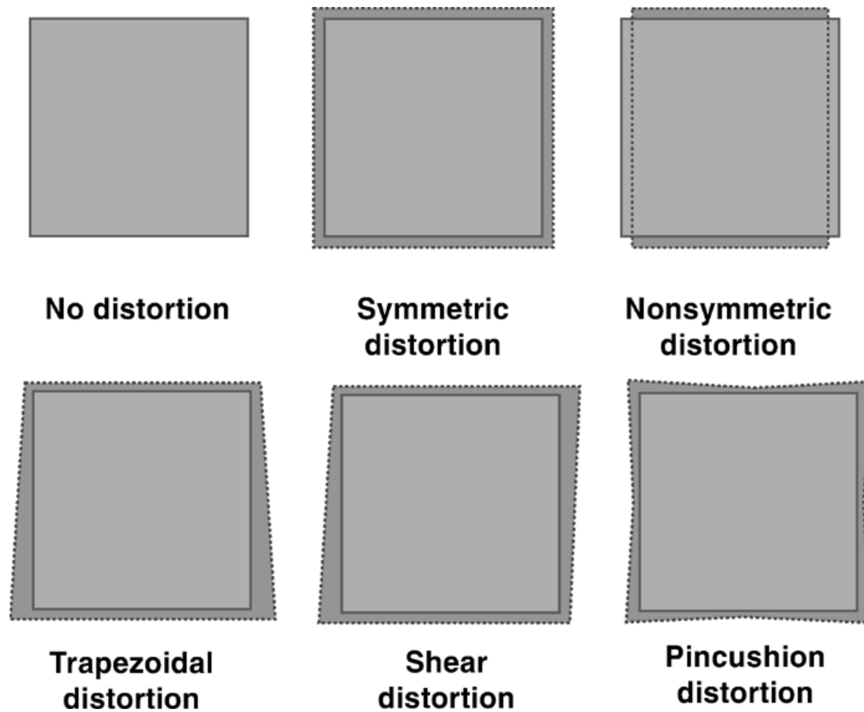

Figure 2.1: Common shape distortions during processing of flexible substrates [34]

. Sources of these web distortions can generally be classified into three categories. Firstly, disturbances from the input control, such as the fluctuation of the roller velocity, web tension, and print pressure, thickness nonuniformity of the web, runout and out-of-roundness of the rollers, and misalignment/installation errors of actuators and sensors. Non-uniform web tension leads to bagginess and slack edges, reducing stability [41]. When the tension variation is considerable, a break [42] may take place in a weak spot on a web, causing the machine to shut down. Further, compressive stresses due to tension variation lead to buckles and troughs [43], which can induce distorted and erroneous patterns and reduce the accuracy of manufacturing.

Second, disturbances induced by processing must be considered, such as temperature change from heating or cooling, print pressure during pattern transferring or forming, thermal energy when producing a laser pattern or heat transfer and radiation pressure in photolithograph. Different temperature and humidity in particular may cause out-of-plane deformations of thin web, such as warpage and twist [44] as a function of both the material properties of the web, which may

vary, and individual process parameters. Unique to R2R manufacturing are defects due to winding and unwinding, e.g. starring and telescoping [45].

Lastly, disturbances from the external environment are also key in understanding R2R process variation such as mechanical vibrations from the ground, air flow around the web, and the variations of environmental temperature and humidity along what can be km scale web lines. In the high speed operation necessary for economically viable high throughput R2R systems, the effects of air-web interaction in particular cannot be neglected [46]. As the speed of the airflow around the web during processing increases web vibrations due to effects like vortex shedding [47] occurs and can cause production quality problems or breaks in the web. Further, increasing production speed also increases the significance of entrained air in any gaps which exist between the web and any rollers, causing traction loss and slippage [48]. This in turn can lead to web wandering and weave [49].

Regardless of source, variations in web tension, deformation, or even slippage at critical stages of processing all must be considered when striving to achieve micron and sub-micron scale precision in R2R manufacturing. As such, any unwanted disturbances, including those small enough that would normally be considered negligible for bulk-scale manufacturing, may have outsized effects on fabrication quality and alignment accuracy for micro- and nanoscale features. Thus, there is significant interest among the research community for high-precision mechanisms to compensate or correct for alignment errors, high-resolution sensing systems to provide accurate position feedback, and appropriate closed-loop control algorithms to simultaneously control web tension, velocity, and position in a stable and robust manner.

2.1.1 Web Models

Roll-to-roll systems are intricate manufacturing lines that are further complicated by the kinetic nature of the components involved, including, but not limited to, the moving rollers, the flexible substrate, metrology subsystems, and the patterning processes themselves. As such, optimizing a R2R system to operate effectively at smaller and smaller scales requires careful consideration of each component. Numerous models have been historically considered by the community to improve the performance of the R2R system by investigating effects such as longitudinal dynamics [50], lateral dynamics [51], winding mechanisms [52], wrinkles [53] and register errors [54].

Campbell [55], Grenfell [56], Brandenburg [54], and Shin [57] conducted some of the seminal studies of longitudinal dynamics in conveyed webs. In the late 1950's, Campbell (1958) [55] assumed that the moving web material obeys Hooke's law. However, web tension in the incident span was not considered in this model. Later, Grenfell (1963) [56] innovated through the consideration of tension in incident and outgoing web spans such that multi-span system modeling was possible. Brandenburg (1976) [54] conducted simulations of dynamic behavior in web handling systems using a solely elastic modeling approach to show that the stress, strain, and velocity in any free spans do not vary with respect to web position under either steady state or transient operation. Shin (1991) [57] furthered this model by systematically distilling complex web handling systems down to combinations of seven base components: unwind roller, free span, driven roller, idle roller, dancer-type tensioning roller, and rewind roller.

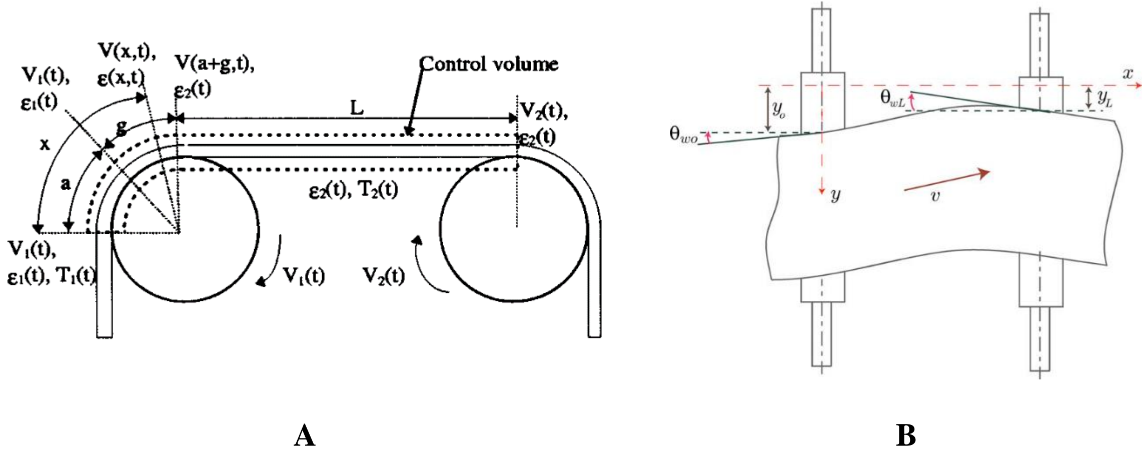

Figure 2.2: Web models in longitudinal dynamics (A) and lateral dynamics (B) [58], [59]

Generally, models for longitudinal tension in web systems focus, as shown in Figure 2.2A, are based on three laws [58]:

(1) Hooke's law, which models the elasticity of the web, as described by Equation (2.1), where T, E, S, ε, L, and L_0 are the web tension, Young's modulus, web section, web length under stress, and web length without stress.

(2) Coulomb's law, which describes tension disturbances due to the friction between web and rollers, as described by Equation (2.2), where a and g represent the arc length of the sticking zone and sliding zone, respectively, and μ, x, and t represent the friction coefficient, position on the web, and time.

(3) Conservation of mass, which defines the relationship between web velocity and strain, as described by Equation (2.3), where ρ and V represent the density and web velocity.

$$T = ES\varepsilon = ES\frac{L - L_0}{L_0} \tag{2.1}$$

$$\varepsilon(x,t) = \begin{cases} \varepsilon_1(t) & 0 \le x \le a \\ \varepsilon_1(t)e^{\mu(x-a)} & a \le x \le a+g \\ \varepsilon_2(t) & a+g \le x \le a+g+L \end{cases} \tag{2.2}$$

$$\frac{\partial \rho}{\partial t} + \frac{\partial(\rho V)}{\partial x} = 0 \tag{2.3}$$

These fundamental models, however, fail to accurately portray certain aspects of a modern R2R system. While Hooke's law remains valid for most common web materials, the relationship between strain and tension is far more complex when using viscoelastic materials such as the polymeric substrates often employed in R2R fabrication due to their low cost. Using springs and dashpots to represent the elastic modulus E and viscosity η, respectively, Sakamoto (1995) [60] considered the viscoelastic characteristics of the web and compared the Maxwell, Voigt, and 4-element Voigt models. On the other hand, Tree (1998) [61] modeled the dynamic behavior of viscoelastic webs using the White-Metzner rheological equation of state and found that while a single span model showed litter difference in accounting for viscoelastic effects, these properties significantly alter the magnitude and even sign of the calculated tension in subsequent spans, demonstrating the importance of accounting for these properties.

Moreover, the Young's modulus will also vary with respect to both temperature and relative humidity. Therefore, the elasticity properties of the web may change considerably during different processes. Kim (2008) [62] considered thermal effects and gravity for web transport in a continuous annealing process. Pagilla (2014, 2017) [63], [64] developed a model of temperature distribution in moving webs under varied heating and cooling conditions by considering three mechanisms of heat transfer: convection due to ambient air; conduction through direct contact with rollers; and radiation from the substrate and electric heaters or gas burners.

If the tension varies significantly, a sliding zone at the roll entry can form. When this occurs the contact between the web and roller may be divided into three sections: entry slip, a middle region of adhesion, and exit slip [65]. Further, Pagilla (2013) [66] modeled the effect roller eccentricity and out-of-roundness errors on web tension and velocity, and accurately predicted the periodic oscillations due to these sources of error. Moreover, Ross (2009) [67] from MotionPort has utilized a commercial, off-the-shelf, multibody dynamics (MBD) software to simulate web behavior.

Taking a different approach for lateral dynamics, Shelton (1971) [51] used a Euler beam model to calculate the quasi-static equilibrium of a single web span, while a string model [55] was in use at the time. The downstream boundary conditions in that model, called "normal entry rule", showed how moving webs "climb" rollers. The Shelton model, as described by Equation (2.4), has become the foundation of web lateral dynamics, where x, y, T, and EI represent the distance along length of the web, web lateral deflection, web tension, and bending stiffness, respectively. Later, Sievers (1987) [68] modeled a span of web as a beam with shear flexibility – a Timoshenko beam - as described by Equation (2.5), where GA and n represent the shear stiffness and correction factor for minimizing the error in the calculation of the shear force, respectively. Shelton (1988) [69] later extended his work to multiple spans with center or end pivoted guides, and utilized state estimation to predict lateral web position based on a downstream sensor. Lastly, based on the deterministic model and experimental data, Young (1990) [70] introduced a new stochastic model for lateral web dynamics, which includes an autoregressive integrated moving average (ARIMA) model to describe disturbances and improve state estimation through initial value generation for measurement and process covariance.

$$\frac{\partial^4 y}{\partial x^4} - K^2 \frac{\partial^2 y}{\partial x^2} = 0,\ K^2 = \frac{T}{EI} \tag{2.4}$$

$$\frac{\partial^4 y}{\partial x^4} - K^2 \frac{\partial^2 y}{\partial x^2} = 0,\ K^2 = \frac{T}{EI\left(1+\frac{nT}{GA}\right)} \tag{2.5}$$

As with the modeling effort for longitudinal dynamics, web models for lateral dynamics would have been expanded in recent years to account for more phenomena. For example, Benson (2002) [71] developed a quasi-static Timoshenko beam model to predict the lateral dynamics in webs with in plane geometrical imperfections, including spliced, warped, or cambered webs, separately. The web material's viscoelastic damping property [72], line mass density [73], or web tension variation [74], were also considered to build models for lateral dynamics. More recently, Pagilla (2010) [59] investigated lateral dynamic models for pivoted guide and offset-pivot guide web steering, and further (2018) [75] derived spatially dependent transfer functions for web lateral dynamics, which aid in the control of lateral position and slope in any web span not in contact with a roller.

2.1.2 Tension and Velocity Control

Given the complexity with which researchers have been able to model the dynamics of a moving web, control systems have also been developed alongside these models in order to stabilize web tension, minimize the impact of both intrinsic and extrinsic disturbances, and control the R2R system to optimum conditions for fabrication. Web-based system control mainly includes tension and speed control based on longitudinal dynamics, and lateral position control based on lateral dynamics. In conventional R2R systems, driven rollers are utilized for web tension/speed control and a web guide subsystem is used to control lateral web position. There are two primary feedback signals typically used for tension control: tension feedback from a load-cell mounted on idle rollers

and displacement feedback (either linear or rotational) from a dancer (moving roller) tensioning subsystem.. The control schemes most commonly used in R2R systems are either a “single-loop” pure speed control or a “double-loop” cascaded tension control, where speed control is in the inner loop and tension control is in the outer loop. Further, the motors which control the driven rollers are most often run in either velocity or torque control mode.

For large scale systems, two general types of control hierarchies are employed [57]: centralized control and decentralized, or distributed, control. Centralized control is typically non-trivial to design and requires processing relatively large quantities of data from all web subsystems involved, often resulting in the highest performance possible. That said, failures or loss of data connectivity from any individual subsystem may disrupt the centralized system as a whole and lead to global instabilities. In decentralized control data related to only immediately adjacent subsystems is necessary, and implementation is comparatively straightforward. Further for complex, high order systems consisting of many interconnected web spans, decentralized control is significantly less difficult to implement compared to a centralized control architecture.

Amongst distributed control techniques, two primary techniques are most commonly used for tension control [57]: (1) open-loop "draw control", where web tension is regulated by controlling the velocities of rollers within a span, but due to the "tension transfer" effect between spans, this approach does not lead to precise tension regulation within an individual span; or (2) closed-loop tension control based on a "progressive set-point coordination" scheme, where the inputs of downstream driven rollers will automatically change according to the input of an upstream driven roller, and with this control technique, tension in each web span can be controlled independently in a multi-span web transport system. In order to overcome these deficiencies, Kee-Hyun Shin (1991) [57] developed an approach to the design of a distributed tension control systems

in multi-span web systems which can reject disturbances due to inter-span tension transfer. The structure of such a distributed tension control system is shown in Figure 2.3, where the auxiliary controllers $U_{n\,n-1}$ decouple the dynamics of the web in a multi-span system, U_n and Y_n are the local control and performance of the *n*th subsystem.

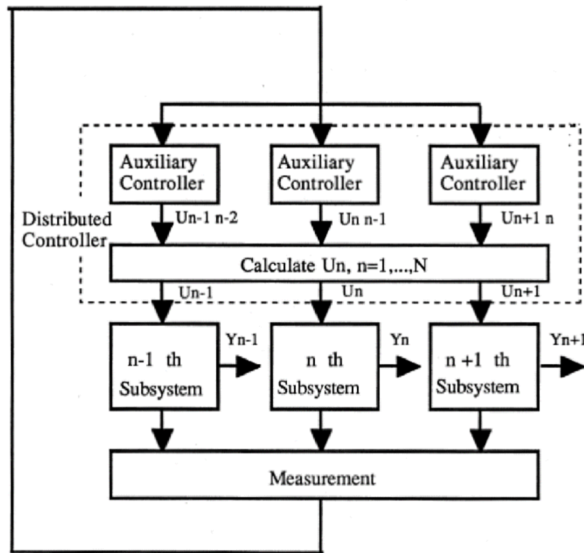

Figure 2.3: Structure of distributed tension control system [57]

The structure for decentralized control can take two forms: disjoint (or non-overlapping) and overlapping decomposition structures. In the disjoint decomposition method, each subsystem controller generates control signals by considering only the corresponding subsystem, while overlapping decomposition considers the interactions between adjacent subsystems or web spans. Sakamoto (2000) [76], [77] derived the transfer functions of the decentralized control and evaluated the interactions by using robust stability and output errors. The results showed that the disjointed decompositions may lower control performance due to mutual interactions, while overlapping decompositions leads to minimized mutual interactions thus improving the performance.

The traditional PID controller, a mainstay in a plethora of control systems, has of course also been applied to web systems. In its most simple configuration however, a fixed gain PID controller, extensive tuning is required to achieve performance goals and re-tuning every time there is a change in material properties or operating conditions. Conversely, a variable PID gain control [78] can stabilize the tension of the winder roller regardless of the continuously variable system constants such winder roller radius. Fuzzy-PID control [79] where the PID gains based on fuzzy logic rules varied according to the unwinder roller radius successfully improves the response of rewinder system, and stabilized the web transport. This self-tuning PID control [80] can effectively reduce overshoot and improve settling time. Pagilla [81] also furthered this research with two adaptive PI control schemes in a R2R system for varied conditions without requiring extensive tuning and retuning. The direct adaptive PI control scheme based on the reference model requires some knowledge of system parameters for initializing the adaptive gains, while the indirect adaptive PI control can automatically initialize the adaptive gains.

Due to the susceptible nature of R2R webs to both outside disturbances and varying substrate material properties and thickness, robust control techniques have also been considered for R2R systems. A robust multivariable control using the H-∞ loop shaping method [82], was combined with a gain scheduling approach and applied to a tandem cold rolling process where it improved quality. Further an estimated decoupled state feedback control based on a Luenberger observer [34] was created for the linearized dynamics of controlled spans, and the convergence of the state and estimation errors was shown. An H-∞ robust control scheme with varying gains, combined with a linear parameter varying (LPV) control [58], was then utilized for a winding system in reducing coupling between web tension and velocity in addition to robustness to roller radius and inertia changes. Later, multivariable, H-∞ control with two degrees of freedom (2DOF)

[83] was proposed to allow for weighting of controller synthesis effort for controller qualities such as disturbance rejection and reference tracking in winding systems. Web-winding systems are often modeled as linear time-invariant (LTI) systems, but at least two nonlinearities are common in these systems: (1) the reel radii and moments of inertia change as the web spools from one reel to another subject to the precision of the rotary bearings employed and (2) air entrainment between the web and roller, altering system characteristics nonlinear by changing the length of web which may vibrate freely. Thus, a Lyapunov-based feedback nonlinear control [84] was proposed, which was robust to air entrainment and uncertainties in motor torque and friction parameters. A multi-model industrial PI controller adjusted with evolutionary algorithm, and a multi-model H-∞ controller [85] were both implemented to an electric motor driven accumulator and obtained good robustness against mechanical parameter variations. The multi-objective robust design optimization methodology was applied to a fixed order and structure LTI H-∞ controller [86] for a large scale R2R system and showed more robust than the commercial one.

In R2R systems, some external disturbances are periodic, a primary example being roll eccentricity. Internal model control (IMC) is effective when some aspects of system disturbances are partially or completely known. An exemplary IMC which consists of a proportional controller and an internal model of sinusoidal tension disturbance with a known frequency and unknown amplitude, was implemented in an active dancer system for periodic tension disturbance attenuation in web process lines [87], [88]. Repetitive control [41] has also been applied to compensate for roll eccentricity disturbances and is often composed of multiple periodic components that may not be rationally related to each other. A discrete-time repetitive controller [89] was also successfully used for the rejection of periodic load disturbances with an unknown period in the continuous steel casting process. A H-∞ modified repetitive controller with periodic

event-based dynamic output feedback [90] was also tested, which updates when needed so that saves communication resources and alleviates burden on control signal transmissions, actuators, etc. An active disturbance rejection control (ADRC) strategy [91], [92], which accounts for dynamic changes in the system in addition to unpredictable external disturbances, was proposed and demonstrated remarkable disturbance rejection capability in the web transport processes.

Recently, neural network based approaches have been utilized in various control systems including R2R systems. An adaptive neural network control based on a recursive least squares learning algorithm [93] compensated for roll eccentricity without any information about the position of the rolls. A multiple-page-mapping backpropagation neural network (BPNN) algorithm [94] was used for speed-tension control of a metal-film coating machine and successfully isolated the speed and tension control paths and avoided the interference between both paths. BPNN [95] was also utilized for speed and tension control in the unwinding roller driven motor. A general regression neural network (GRNN) [96] was used to learn an optimal compensation signal and improve performance when implemented in parallel with a conventional controller by suppressing periodic disturbances. Recurrent neural network [97] approaches were used to design an estimator for estimating system uncertainties including system parameter variations, unmodeled errors, and external disturbances. Neural network was also combined with fuzzy logic control in a neuro-fuzzy system [98], [99] for tension control. During the operation, the parameters of the fuzzy controllers were adjusted by using the back-propagation method. Artificial neural networks can also be used to identify the faulty rollers and diagnose the degree of fault in the rollers [100] by using the characteristic features of tension signals for training, such as RMS, peak value, and power spectral density.

2.2 EXISTING MULTI-LAYER ALIGNMENT METHODS IN R2R MICRO/NANOFABRICATION SYSTEMS

While modern R2R fabrication systems have achieved a rather high resolution, i.e., tens of nanometers [101], their overlay accuracies remain relatively low, i.e., micron level, which cannot satisfy the requirements of emerging multi-layer functional flexible devices, for instance, complex flexible electronics and metamaterial absorbers [102]. Precise layer-to-layer alignment is a challenging requirement for manufacturing multi-layer flexible electronics; the issue is difficult to address as flexible substrates, unlike conventional rigid substrates, are prone to deformation during different manufacturing processes and loading conditions as previously discussed. There are several existing methods to register moving webs achieving tens of micron resolution. Some alignment strategies are "passive", e.g., using individual photomasks to compensate for dimensional changes in the substrate before each layer [103], or developing models to study the overlay alignment process [104]; others alignment methods are "active" and usually more costly. For example, real-time imaging of registration marks on the web through a CCD vision system and adjusting of the print roller or web [1] or tuning the velocity of the roller [105] to improve overlay error. In the following sections, state-of-the-art multi-layer roll-to-roll systems will be introduced and reviewed. An understanding of the achievable, and aspirational, overlay error specifications will inform the required measurement precision needed in any new tool for use in developing new R2R nanofabrication systems or processes.

2.2.1 Scale Compensation

One of the major barriers to high-resolution layer-to-layer alignment in R2R systems is the dimensional instability of flexible substrates, i.e., dimensional changes induced by mechanical tension or thermal shrinkage during processing. To overcome this problem, scale compensation

methods measure the dimensional changes in advance through calculation, simulation, or experiments, then compensate the changes during or before the manufacturing.

There are several ways to compensate for process-induced substrate distortions [40]:

1) Laser direct write patterning may be used to compensate for any dimensional changes. However, this approach is limited in throughput due to the significant time cost associated with the serial nature of the process.

2) Distortion is measured in advance through experiments and a compensated mask is fabricated. Strohhöfer et al. [103] measured the dimensional changes of different layers on different processing conditions and print masks were adjusted to compensate for substrate dimensional changes. In this manner, the misalignment was successfully reduced from 250 μm to 25 μm per 10 cm substrate so that the registration accuracy was increased by an order of magnitude. This technique is suitable for compensating systematic dimensional changes due to processing, while it can be time-consuming, and high cost if glass masks are used. Film masks are much less-expensive to manufacture, but they are also susceptible to changes in size due to temperature or humidity variations.

3) Symmetric scale compensation, or magnification or demagnification of the image by the same amount in the *X*- and *Y*-dimensions. This method is limited in effectiveness as the substrate changes may not be symmetric. Jain et al. [40], [106] performed automatic scale compensation via an optomechanical system (shown in Figure 5), which provides independent correction of substrate dimensional changes in the *X*- and *Y*-directions, without compromising the throughput. Their new R2R lithography systems achieved high-precision alignment (±2.5 μm) over large exposure areas

(300 × 300 mm). Moreover, this technique can be developed to compensate the higher-order shape distortions, such as trapezoidal, shear, and pincushion varieties.

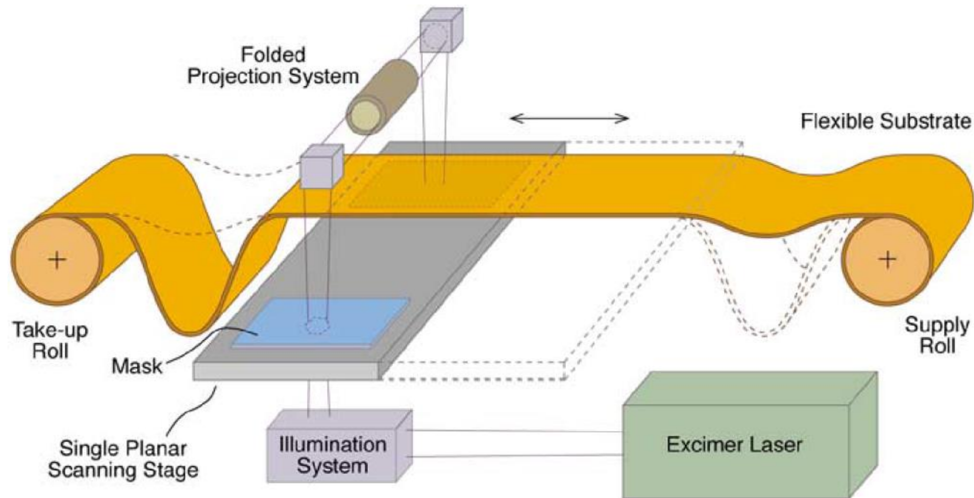

Figure 2.4: Schematic diagram of a large-area high-throughput roll-to-roll patterning system [40]

Kim et al. [107] measured the plate roller engraving accuracy to predict the magnitude of register errors prior to actual printing, and indicated that high register accuracy requires high engraving accuracy.

Scale compensation methods are important even for single-layer R2R manufacturing. However, most of them are "passive" for multi-layer alignment and only deal with alignment errors in two directions, i.e., web or machine direction (MD) and cross direction (CD). Furthermore, they cannot address the alignment errors due to disturbances on the flexible web or statistical fluctuations that are inherent to the fabrication process. Therefore, scale compensation methods are often utilized together with other alignment methods.

Researchers	Scale compensation methods	Alignment accuracy	Throughput
Anvik (2005) [40]	Automatic scale compensation	±2.5 μm	0.6 m/min
Fraunhofer IZM (2007) [103]	Compensated print masks	25 μm	0.5~2 m/min

Kim et al. (2017) [107]	Measure engraving accuracy and predict register accuracy	10s µm	0.6 m/min

Table 2.1: Summary of scale compensation methods utilized in R2R manufacturing systems

It is well-known that precise multi-layer R2R fabrication systems require precise layer-to-layer alignment, while self-aligned methods utilize special process steps, unique material properties, or specific mask structures for high-resolution self-alignment, thus eliminating the need of complex alignment systems.

2.2.2 Self-Alignment Using Back-Substrate Exposure (SABSE)

The basic fabrication process of self-alignment using backsubstrate exposure (also called back-surface exposure or substrate reverse side exposure) is shown in Figure 2.5 [108]. First, a gate metal electrode is evaporated and patterned on transparent substrate, e.g., glass or plastic, then a gate insulator is deposited. Next, backsubstrate exposure is carried out, where the gate electrode is used as a photomask (Figure 2.5a), then an ohmic metal electrode is evaporated (Figure 2.5c) and the lift-off process is carried out (Figure 2.5d). Finally, a semiconductor is evaporated (Figure 2.5e) and a self-aligned organic field-effect transistor is obtained.

Using the back substrate exposure method, source and drain electrodes are self-aligned to the gate electrode. Similarly, source/drain electrodes can be also used as a photomask to define the gate electrode [109]. SABSE requires the optical transparency of substrates and contrary relationship between two pattern layers, such as gate layer and source/drain layer, so that one pattern layer can be deposited first and act as an opaque mask to define the other pattern layer.

In 2008, Kim et al. [110] from Korea Institute of Machinery and Materials (KIMM) combined this self-aligned process with R2R printing system for fabricating organic thin film transistor.

Based on their R2R system, a self-aligned OTFT having ~60 µm channel length was fabricated, and its transfer and output characteristics were tested. Gold et al. [111] have fabricated self-aligned OTFTs having channel lengths between 10 and 0.5 µm on plastic substrates through nanoimprint lithography. Vilkman et al. [112] from VTT Technical Research Centre of Finland Ltd also utilized the SABSE method on continuous R2R techniques for the production of organic bottom-gate transistors with self-aligned electrodes, allowing sub-5 µm layer-to-layer overlay registration. The improved registration minimized overlap between the source and drain electrodes and the gate electrode which therefore also minimized the parasitic capacitance of the TFT.

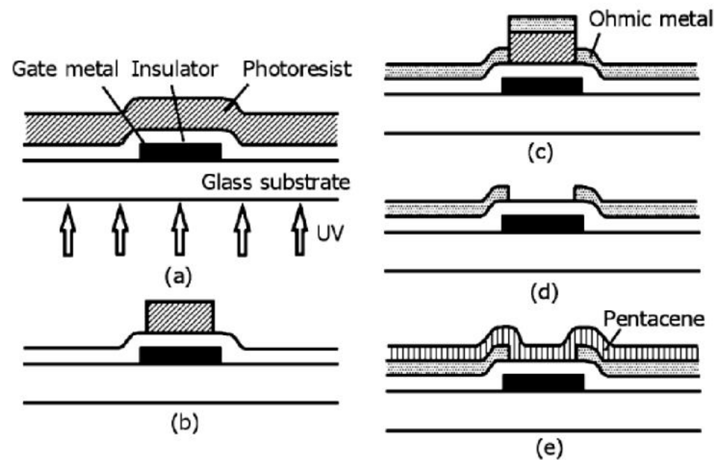

Figure 2.5: Fabrication steps of self-aligned organic field-effect transistor using back substrate exposure [108]

2.2.3 Self-Aligned Inkjet Printing (SAP)

In 2005, Sele et al. [113] invented a lithography-free, bottom-up, self-aligned inkjet printing technique that utilizes the flow properties of small liquid droplets on heterogeneous surfaces to define sub-100 nm critical features with high yield and uniformity without the need for precise layer alignment. Later, Zhao et al. [114] extended this method to fabricate field-effect transistors (FETs) with high conductivity electrodes and to achieve channel lengths from 4 µm down to 60 nm.

The self-aligned printing (SAP) method for fabricating a top-gate thin-film-transistor (TFT) architecture is shown in Figure 2.6. Figure 2.6A illustrates that a hydrophobic self-assembled monolayer (SAM) lowers the surface energy of the first electron; then a small self-aligned gap (L) is formed after the flow-off and drying of the second electron. Figure 2.6B demonstrates that by exposing the structure with UV light through the back of the glass substrate, a trench structure in the photosensitive dielectric layer can be developed as the gate electrode, which is self-aligned with respect to the edges of the source and drain electrodes.

Likewise, Tseng et al. [115] applied the concept of wetting-based self-alignment to fabricate an all inkjet-printed bottom-gate transistor, as shown in Figure 8. During the process, decreasing the surface energy of the poly(4-vinylphenol) (PVP) layer and increasing the surface tension of the S/D ink were performed to better control the self-alignment.

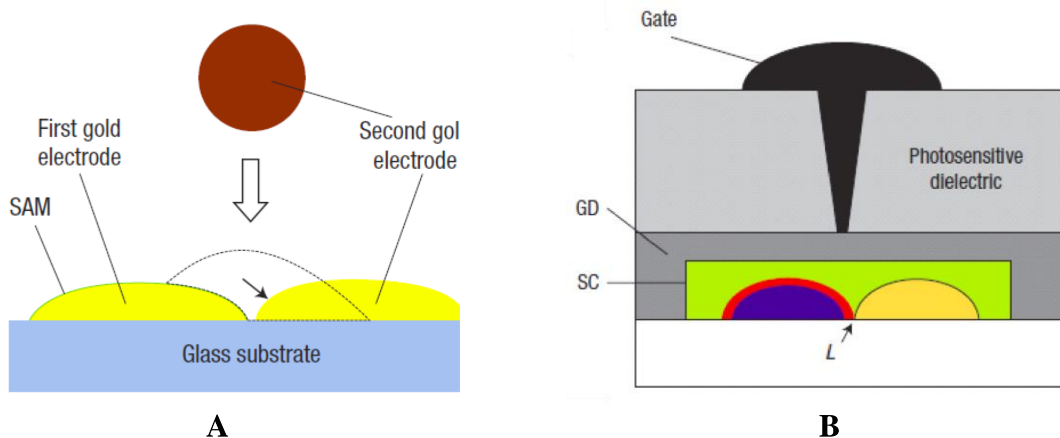

Figure 2.6: Self-aligned inkjet printing. A: Schematic of the SAP process. B: Schematic of the process to form a self-aligned gate (SAG) structure [116]

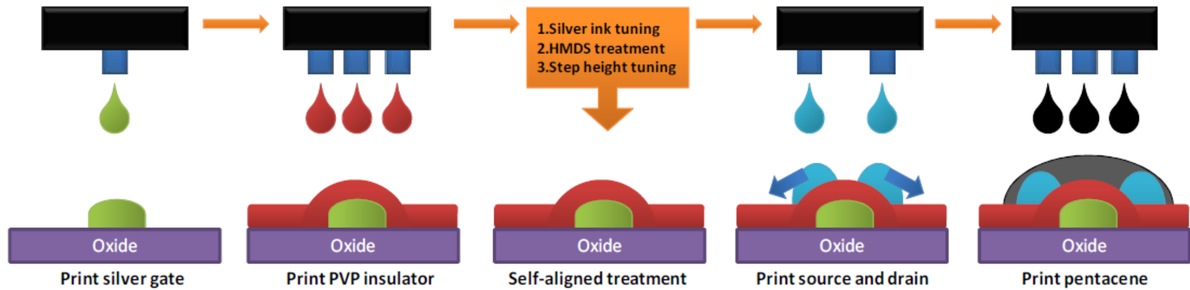

Figure 2.7: All inkjet-printed transistor process with self-aligned S/D [117]

2.2.4 Self-Aligned Imprint Lithography (SAIL)

In 2009, Kim et al. [118] from Hewlett-Packard (HP) invented self-aligned imprint lithography (SAIL), which enables patterning and alignment of sub-micrometer scale features on meter-scale flexible webs in a R2R fashion. SAIL addresses overlay error and registration on a moving web by encoding all geometric information required for patterning into a monolithic masking structure. The multi-level 3-D mask is produced by imprint lithography on a blanket-deposited substrate in one step before etching to pattern the underlying layers into the desired structures. The pre-aligned multiple-step mask structure maintains its alignment regardless of subsequent process-induced substrate distortion. Figure 2.8 below the SAIL method for fabricating a bottom-gate TFT with submicron alignment accuracy.

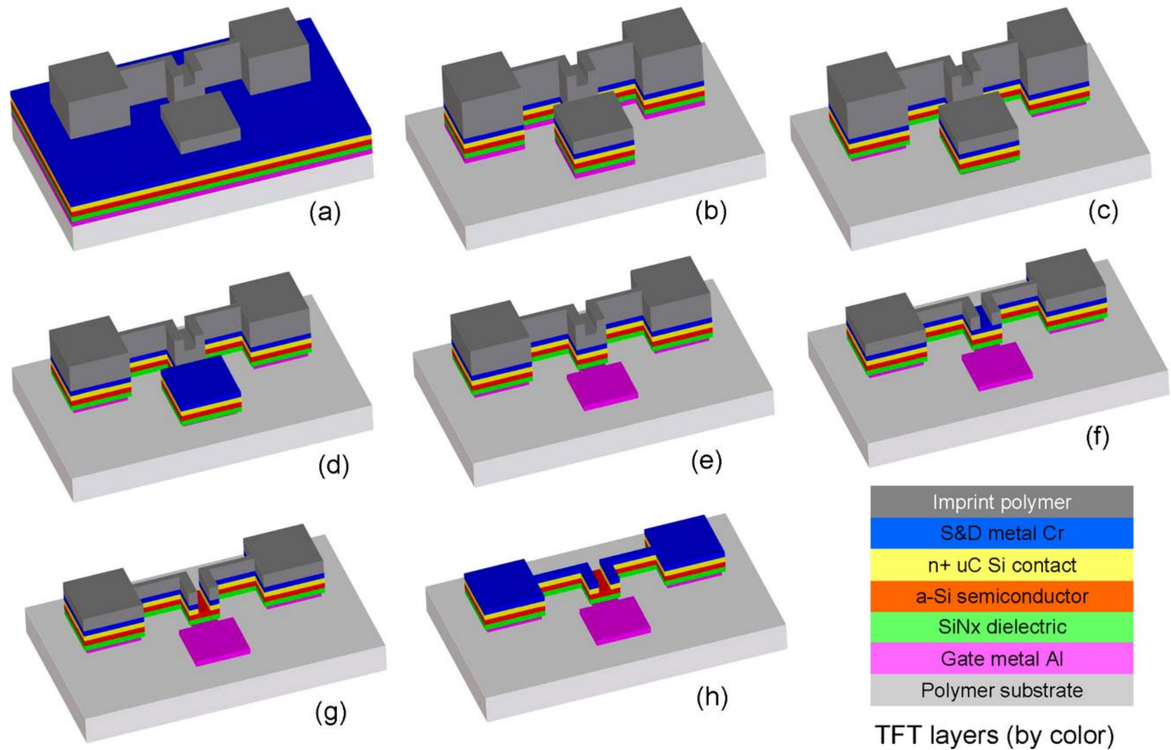

Figure 2.8: Schematic diagrams of the SAIL process flow for fabricating TFTs [118]

Later, Maury et al. [119], [120] from Holst Centre pointed out some issues in the SAIL process, such as the residual layer removal and metal evaporation on foil, and developed a new approach to address these issues. Unlike the top-down approach developed by HP, this bottom-up method is based on multi-level to induce super hydrophobicity on some levels and thus enable selective patterning. The advantage of this approach is that there is no temperature requirements for the fabrication and no etching of the residual layer of the imprint is required.

Lausecker et al. [121] developed SAIL for top-gate TFTs, while original SAIL is applied to conventional bottom-gate transistors. Wan et al. [122] then developed a planar self-alignment imprint lithography (P-SAIL) to fabricate metallic and dielectric structures on the same plane, enabling designs which manipulate propagation of light through the devices.

Additionally, imprint techniques, such as ultraviolet (UV) imprinting [123] and embossing [124], can be assisted for self-alignment because it can generate 3D complex structures. For example, Li et al. [125] utilized imprinting to define the channel length, and then the gate electrode could be self-aligned according to the 3D structure, as shown in Figure 2.9. Jeon et al. [126] demonstrated short channel and self-aligned OTFTs on a flexible substrate by imprinting a prism-like pattern, as shown in Figure 2.10. The self-aligned structure enabled accurate alignment between electrodes, reducing parasitic overlap capacitance by 80% \compared to conventional top-contact OTFT structures.

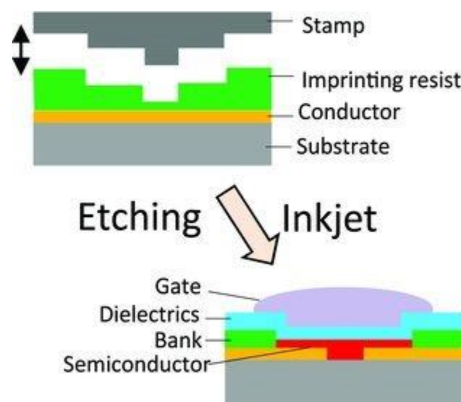

Figure 2.9: Schematic of a TFT fabrication process by a self-aligned, imprint-assisted inkjet printing [125]

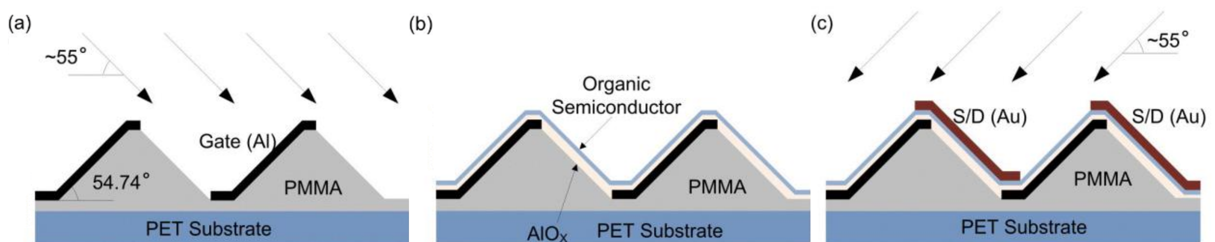

Figure 2.10: Scheme of self-aligned prism-OTFT fabrication process [126]

2.2.5 Summary

Self-aligned methods achieve relatively high layer-to-layer alignment; however, they have their own limitations: SABSE requires that two pattern layers have reversed patterns and is usually inapplicable to fabricating more than two pattern layers. SAP is only applicable to specific

structures, such as FET architecture. Although SAIL can fabricate 3D structures, the fabricated structures are not arbitrary and should be "ziggurat-like". Therefore, self-aligned processes are impractical for fabricating complex 3D structures, and precise layer-to-layer alignment systems are the mainstream in R2R printing process.

Researchers	**Self-aligned methods**	**Alignment accuracy**	**Throughput**
Gold et al. (2015) [111]	SABSE	~500 nm	-
VTT (2016) [112]	SABSE	<5 μm	10 m/min
Sele et al. (2005) [113], [116]	SAP	<100 nm	~Inkjet
Zhao et al. (2007) [114]	SAP	<60 nm	~Inkjet
Tseng et al. (2009) [115], [117]	SAP	~1 μm	~Inkjet
HP (2009) [118]	SAIL	<100 nm	5 m/min
Holst (2011) [119], [120]	SAIL	800 nm	0.35 m/min
Li et al. (2007) [124]	Imprint-assisted	<10 μm	~Inkjet
Li et al. (2011) [125]	Imprint-assisted	<100 nm	~Inkjet

Table 2.2: Summary of self-aligned methods compatible with R2R processing

2.3 VISION-BASED ALIGNMENT

Vision-based methods, or so-called "active" alignment methods, usually utilize optical imaging systems to monitor the alignment marks on the web and then calculate the position of the web or the alignment errors between the pattern layers. Vision-based methods are the most common and popular approach for multi-layer alignment in R2R systems because they can directly provide misalignment feedback and actively compensate the errors. These vision based methods represent the existing systems utilized to measure overlay and registration errors which may compete, and likely complement, the targeted measurement data from the new tip-based system proposed in this dissertation.

2.3.1 Machine Vision

In machine vision-based methods, the most typical conventional alignment mark is usually a cross shape or a polygon, and the sensing resolution is determined by the imaging system, often limited to several microns. High magnification optical lensing can increase the resolution but sacrifices field of view, often rendering this approach to resolution improvement impractical.

In 2009, Yang et al. [127], [128] first introduced a flexure-based multi-axis positioner into a R2R fabrication system to control the print roller for multi-layer alignment. They also utilized two microscopes to monitor the alignment marks and align the position of the flexible substrate. Due to the manual control of the roller positioner, the alignment accuracy is relatively low, i.e., 1017 μm in machine direction and 113 μm in cross direction.

Liu et al. [129] designed a novel roller-reversal imprint (RRI) system, which is similar to microcontact printing or microtransfer molding, for manufacturing large-area active microelectronics. Figure 2.11 illustrates the alignment system: two CCD cameras detect the two alignment marks pre-fabricated on the flexible substrate, individually, and one additional CCD camera detects the alignment mark on the mold roller. Through a static detection and adjustment approach, misalignments in x, y, θ, and Φ axes can be corrected. By using the CCD of 8×8 μm^2 pixel size, a 10× optical amplifier, and a subpixel image-match algorithm, the RRI system has achieved a detection resolution of up to 0.2 μm and an overlay accuracy of 5 μm.

In the R2R imprinting system of Choi et al. [130], a CCD camera was attached over the roll to analyze error in position of the alignment marks on the roll mold, and a microscope attached to an X-Y linear stage with a resolution of 0.1 μm was used as a position measurement system. Utilizing thin glass roll mold increased the average overlay accuracy by an order of magnitude compared to using polymer roll molds.

Koo et al. [131] designed a system with three CCD cameras to control the registration accuracy to a level of ±20 μm in both MD and CD. The first camera detected the printed registration markers after passing through the first printing unit; The second camera detected the registration markers on the gravure cylinder at the second printing unit; And the third camera monitored the alignment of the two subsequent markers to provide feedback to the control program.

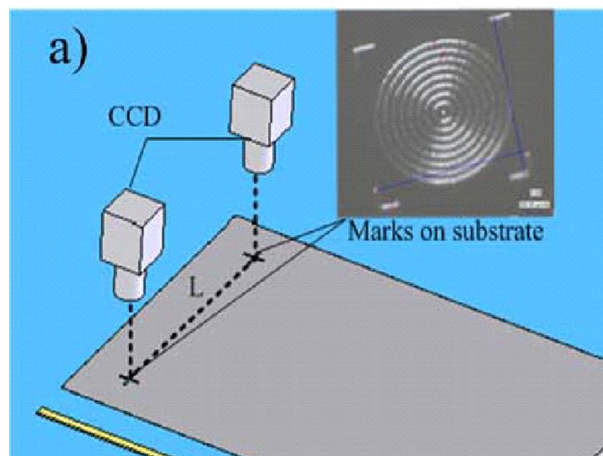

Figure 2.11: Alignment system for the RRI process [129]

In the multi-layer R2R printing equipment of Kim et al. [132]. The register and trigger marks were printed on the flexible substrate together with the desired feature patterns. And the line-scan camera in the second printing unit was activated to capture the register marks when the trigger marks pass through a first trigger sensor (mark 1). Then, the misalignment is calculated by the positions of register marks 1 and 2, and the additional linear motor controls the axial movement of the plate cylinder to compensate for the measured misalignment.

Lin et al. [133] also utilized the combination of a trigger sensor and camera in their multi-layer R2R manufacturing system. A photoelectric sensor senses the Print/Go mark and generates a signal to trigger the actuation of the printing and a line-scan camera was used to detect the

alignment mark. The MD registration was measured through in-line imaging of the alignment mark and determining the onset moment of printing. The CD registration was measured through real time image processing to calculate alignment mark offset and compensate for any deviation.

Similarly, Lee et al. [105] used an optical sensor for triggering; an area-scan camera for capturing the register marks; two programmable logic controllers (PLC1, 2) and register control software for calculating the register errors in their multi-layer R2R system, as shown in Figure 13. By applying appropriate register algorithms and adequate register models, their R2R system achieved a register precision of ±30 μm. In summary, the layer-to-layer alignment procedure in both multi-layer R2R systems of Kim and Lee, is to (1) print, (2) measure, and (3) compensate.

In machine vision-based methods, using printed register marks for register control is necessary. However, inherent printing defects in creating the register marks inevitably lead to measurement errors that reduce the registration accuracy. Lee et al. [134] investigated the effect of register mark design on measurement error and verified that measurement error is increased by any widening or agglomeration of the register mark ink. In order to achieve high-precision register control, it is important to improve the printing quality of the register mark itself, often through selection of an optimized geometry with respect to printability, and utilize an edge-detection algorithm in the control program. Later, Lee et al. [135] investigated smearing defects in register marks, which can increase the register error and degrade the quality of printed layers. The study determined that the three printing conditions - ink viscosity, web speed, and doctor pressure - affect the degree of smearing and suggested that optimizing these printing conditions can reduce smearing and improve the alignment accuracy.

Lee et al. [136] from KIMM also investigated the effects of mark geometry errors on overlay measurement accuracy. To improve the measurement accuracy of the positions of the printed

patterns, the pattern registration algorithms and type of overlay marks were optimized. As a result, measurement repeatability was reduced to 1.0 μm and 2.0 μm in the CD and MD directions respectively in the gravure offset printing process.

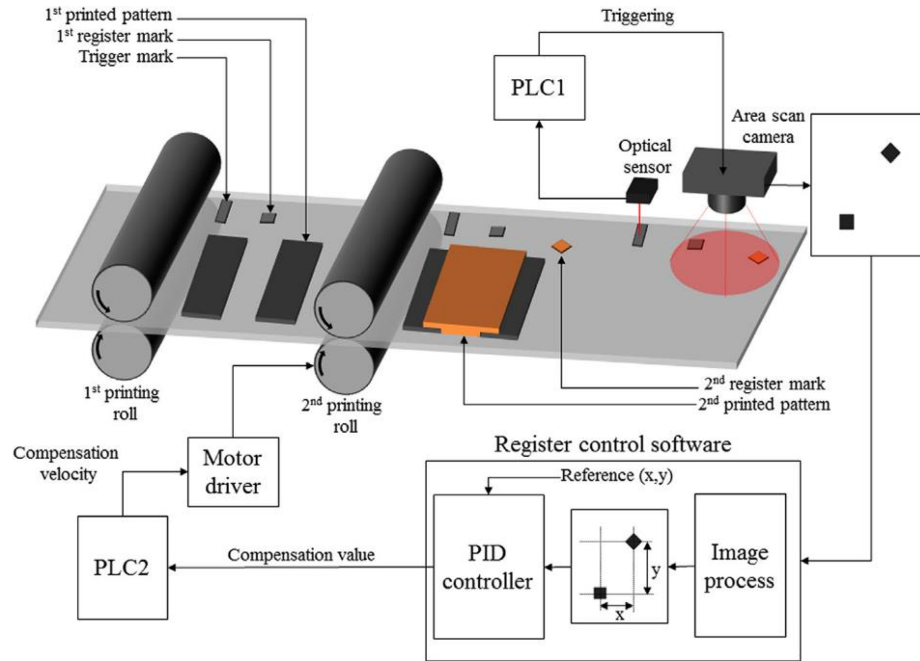

Figure 2.12: Register control in Lee's R2R printing system [105]

Researchers	Vision-based methods	Alignment accuracy	Throughput
Yang et al. (2009) [127], [128], [137]	2 microscopes	1017 μm in MD 113 μm in CD	122 m/min
Liu et al. (2010) [129]	3 CCDs (2 for web + 1 for roller)	5 μm	0.1 m/min
Choi et al. (2016) [130]	Thin glass roll mold + CCD	~3 μm	0.18 m/min
Koo et al. (2015) [131]	3 CCD camera system	±20 μm	8 m/min
Kim et al. (2012) [132]	2 trigger sensors + 1 line CCD	±20 μm	-

Lin et al. (2014) [133]	Photoelectric sensor + line CCD	100 µm in MD 200 µm in CD	5 m/min
Lee et al. (2015) [105]	Optical sensor + area-scan CCD	±30 µm	5 m/min
Lee et al. (2016) [134], [135]	Register measurement error analysis	-	~5 m/min
Lee et al. (2017) [136]	Pattern registration algorithms optimization	2 µm in MD 1 µm in CD (position measurement)	0.6 m/min

Table 2.3: Summary of machine vision-based methods utilized in current R2R systems.

2.3.2 Diffractive Optics

Some vision-based methods utilize structured light or structured alignment marks to enhance the sensing resolution of web position. The structured light is generated by a specific device or diffraction effect. And the structured alignment marks are usually gratings or grids for 1D or 2D position sensing, respectively. Through analysis of these structured light or structured patterns, the resolution of displacement sensing can be increased to nanometer-level, which is not limited by the diffraction of light.

Doignon et al. [138] developed a structured light stereovision system composed of two high frame rate cameras and a laser stripe line pattern device for simultaneously detecting lateral displacements and out-of-plane vibrations of the web in real time. The laser device projected a predefined structuring element, i.e., quite straight line segments, onto the web surface, and two cameras captured the structured patterns to 3D reconstruct the edges of the web and estimate the displacements and orientation changes of the web. Besides, analyzing the relative depth variations of the web surface with respect to the common camera frame can estimate the out-of-plane web

vibration frequencies and magnitudes. It is a fast and noncontact technique for measuring the web displacements and detecting the web vibrations.

Seo et al. [139] proposed a web position optical measurement system (WPOMS) to measure the displacement and velocity in machine direction, and the lateral angle of the moving web in real time. Later, the authors upgraded the system [140] for simultaneous measuring the longitudinal position, lateral position, lateral angle and lateral deformation of the flexible web. The optical measurement principle is illustrated in Figure 2.13: The optical encoder is composed of a structured detector, light source and index gratings, and the alignment patterns printed on the web consist of reflective and non-reflective gratings and the grating pitch is slightly different from that of the index gratings. The light passing through the index gratings is reflected by the alignment pattern, and the detector measures the light reflected back. This measurement is converted into sinusoidal signals due to the relative motion between index gratings and the alignment patterns, and the web displacements in MD and CD can be derived from the difference in the phases and amplitudes of the signal. Using 100 μm-pitch patterns, the system has achieved a position measurement precision of 23 μm in the MD and repeatability within ±2.5 μm in the CD.

It is worth mentioning that in using periodic patterns as an alignment mark, multiple patterns can be measured simultaneously and thus the precision and reliability of the measurements, in principle, will be not sensitive to printing quality degradation and non-uniformity of the fabricated alignment patterns [140].

In Seo's measurement method [139], Kang espoused that the grating printed on the flexible web cannot be as accurate as a scale grating as there will inevitably be variations in pitch and line-width, leading to incresead variation of pitches in the envelop of the generated moiré image. For this reason, Kang et al. [141] proposed a novel algorithm, which can estimate the variations in

pitch precisely, accordingly generate the sinusoidal encoder signal, and correct the Lissajous curve to improve phase interpolation accuracy as well as the performance of the modified measurement system- leading to a displacement error of less than 2.5 μm and velocity error of roughly 0.25% of full scale.

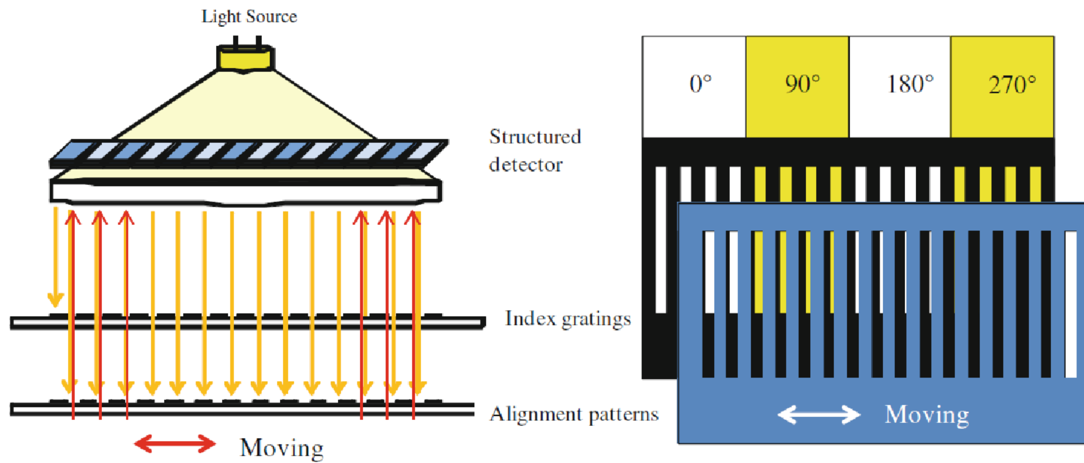

A

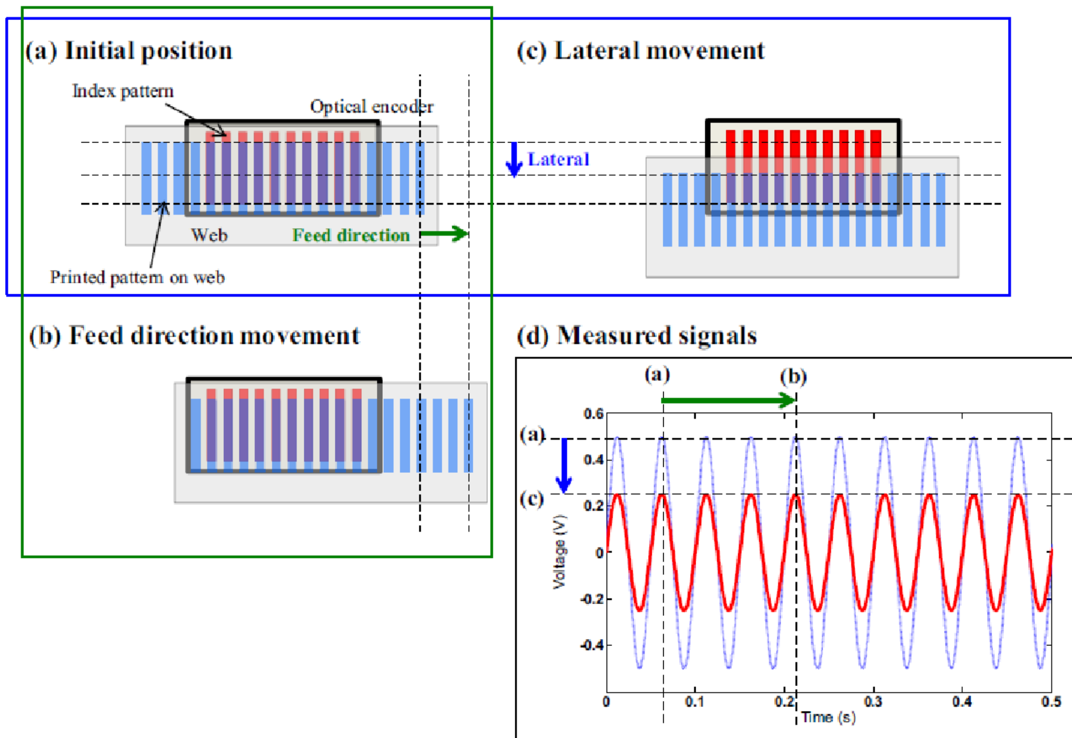

B

Figure 2.13: Principle of optical measurement method for web position in MD and CD [140]

O'Connor et al. [142] designed an interferometric optical encoder for in-line position measurement in a R2R system, achieving sub-micron displacement measurement performance with a high sampling rate of 50 kHz. Figure 2.14 shows the schema of the interferometric optical encoder: a collimated laser beam is focused and then projected through a zero-order suppressing phase grating, e.g., a square profile grating with 50% duty cycle when its amplitude satisfies the condition for destructive interference of light passing through the upper and lower interfaces at the operating wavelength; next, the coherent light is diffracted and interferes on an array of detectors; then the high-resolution displacement can be obtained through measuring the phase of the resulting fringe pattern. Using a line-scan camera or an area scan camera to obtain the fringe patterns at the detector plane, a position measurement accuracy about 30 nm was demonstrated.

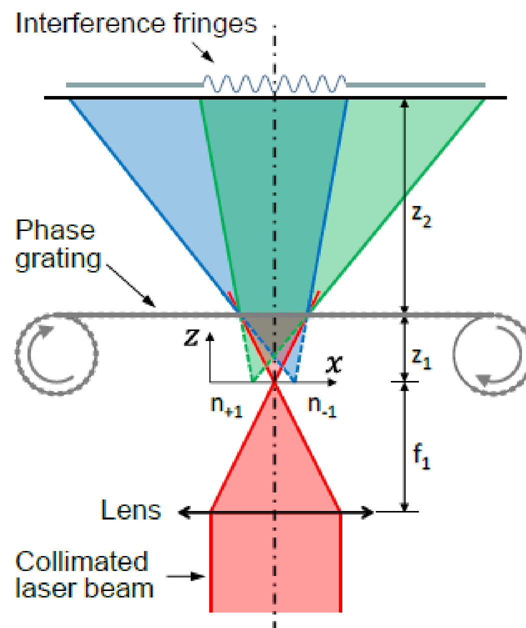

Figure 2.14: Schema of the interferometric optical system [142]

Inspired by the 2D discrete Fourier transformation based phase estimation method for planar position measurement [122], Li et al. [143] designed a vision-based position measurement system for layer-to-layer alignment in a multi-layer R2R manufacturing system. A hybrid alignment mark

was utilized, consists of cross-shaped patterns and 2D grids patterns for measuring absolute position and high-resolution relative displacement of the flexible moving web, respectively. The procedure for real-time web planar position measurement is shown in Figure 2.15: (1) Two cameras image the alignment marks printed on the two edges of the web, then use low-pass filter based processing to identify the cross-shaped mark and apply pattern recognition to obtain the absolute X, Y, and θ_Z positions. (2) Apply a 2-D Fast Fourier Transformation to the current and previous images, then find the two fundamental spatial frequency coordinates in the amplitude spectrum and accordingly calculate the phase changes in the phase spectrums for estimation of the relative displacements, ΔX, ΔY and $\Delta\theta_Z$. Integrated with a flexure-guided five-axis roller positioner for five DOF error correction, the multi-layer R2R system has achieved ~1 μm alignment accuracy.

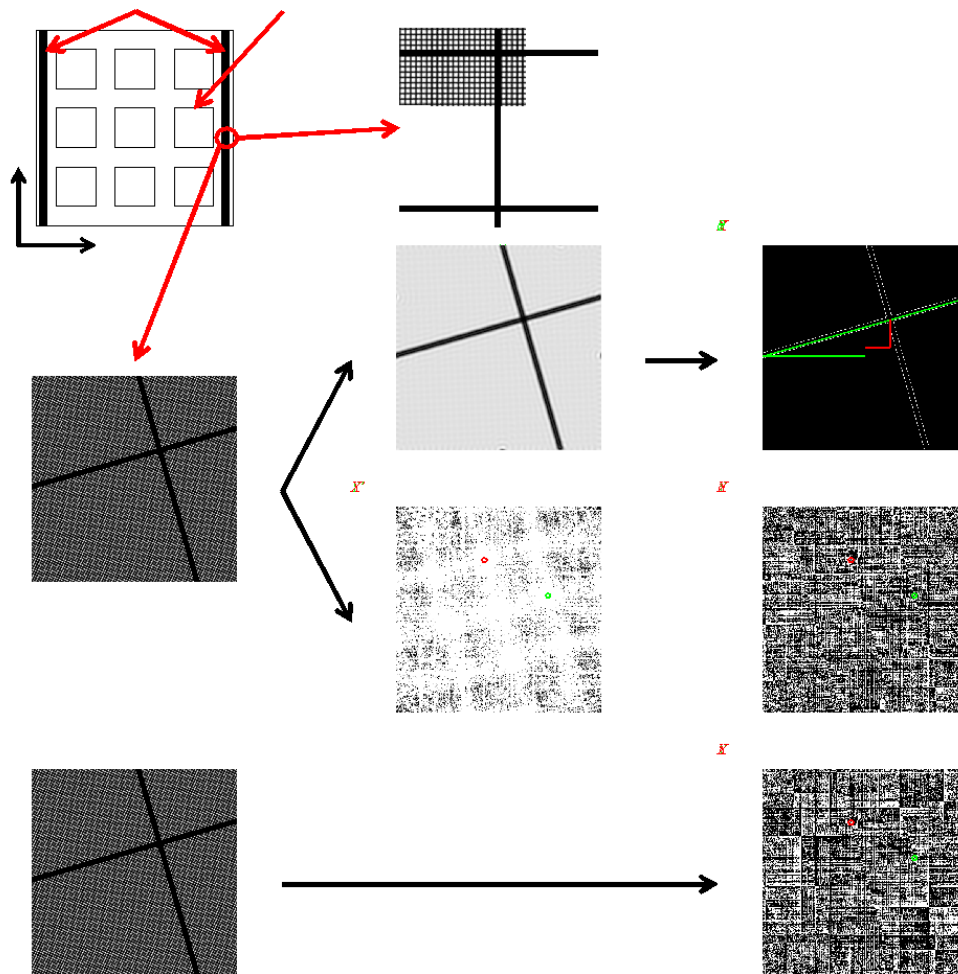

Figure 2.15: The process of web planar position measurement using hybrid alignment marks printed on the two edges of the web [143]

Hu et al. [144] designed an active register control strategy, where a microscope camera measures the register error and a 5-DOF alignment stage adjusts the position of the print header. A motion-based calibration method was also proposed for the microscope to accurately detect register errors by moving the print head in the plane parallel to the web and printing an array of ink dots on the flexible web. The microscope camera then detects the point array and misalignment between web and print head can be calibrated by basic image processing. The experimental results indicated that by adopting the proposed register control strategy, position measurement resolution is better than 4 μm in both MD and CD is achievable.

Using structured light or structured patterns, the resolution and reliability of vision-based alignment systems can be improved. However, the sensing results are usually relative displacements and other methods are required to obtain absolute positions. Besides, most of these techniques were only utilized for web position measurement instead of layer-to-layer alignment in current R2R systems. More efforts are needed so that they can be integrated into multi-layer R2R manufacturing systems.

Researchers	Structured light or patterns	Alignment accuracy	Throughput
Doignon et al. (2008) [138]	Laser stripe line pattern	-	100 m/min
Seo et al. (2013) [139], [140]	Index gratings + alignment patterns	23 μm in MD (position measurement) ±2.5 μm in CD (repeatability)	2 m/min
Kang et al. (2013) [141]	Ronchi grating + printed scale	2.5 μm in MD (position measurement)	6 m/min
O'Connor et al. (2016) [142]	Phase grating	~30 nm in MD (position measurement)	15 m/min
Li et al. (2017) [143]	Cross-shaped marks + 2D grids	~1 μm	0.06 m/min
Hu et al. (2018) [144]	2D array of ink dots	~4 μm (position measurement)	-

Table 2.4:Summary of the performance of the vision-based methods with structured light or structured patterns which is compatible to R2R systems

2.4 Model-based Control

As previously introduced, scholars have built mathematical models for the flexible moving web in R2R systems to improve the performance of winding and manufacturing. Likewise, mathematical models of registers were built and utilized for increasing the registration accuracy in multi-layer R2R systems. The sensing signals from the vision-based system as well as the input

signals, e.g., web tension and roller velocity, physical and environmental parameters such as length of span, radius of roller, and temperature, could be put in the model.

Kee-Hyun Shin's group has derived lots of mathematical models for different registers with different considerations. For example, a MD register model [145] was derived through the mass equilibrium between incoming substrate to a printing cylinder and transported substrate; and a CD register model [104] was also derived using the lateral position of the moving web, translational motion of the printing rolls and time lag (L/V) between printing upstream pattern and downstream pattern. Later, Kang et al. [146] analyzed the correlation between the MD and CD registers, and then derived an oblique-machine direction (OMD) registration measurement, which is more critical in large-area R2R printing because the OMD error is proportional to the width of the substrate. Furthermore, the strain of the moving web was added to the model and a 2D register model was derived [147]. In the above-mentioned research, the MD register (r_x) and CD register (r_y) are defined and illustrated in Figure 17A and Figure 17B, respectively. And the block diagram of the MD and CD register controller are depicted in Figure 17C and Figure 17D, respectively. By utilizing these register models and controllers, an alignment accuracy about ±100 μm in both MD and CD were achieved with a relatively high web speed, i.e., over 40 m/min.

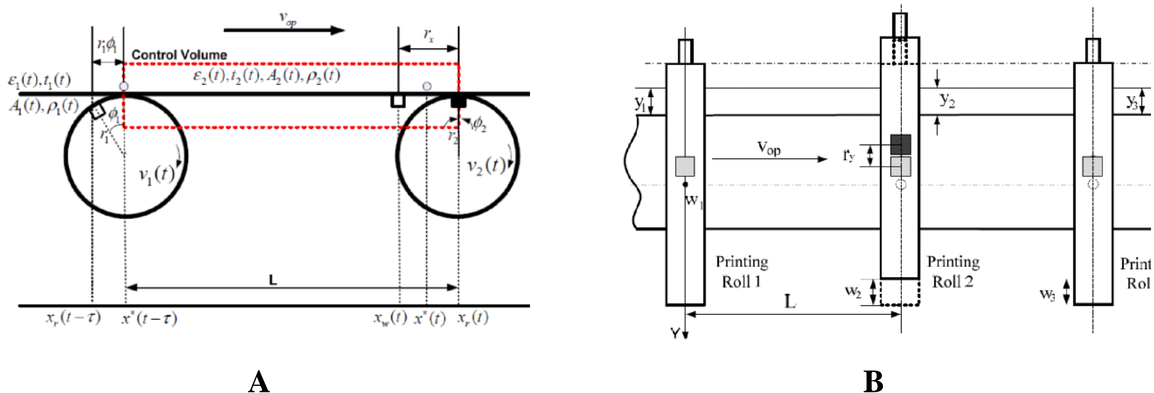

A B

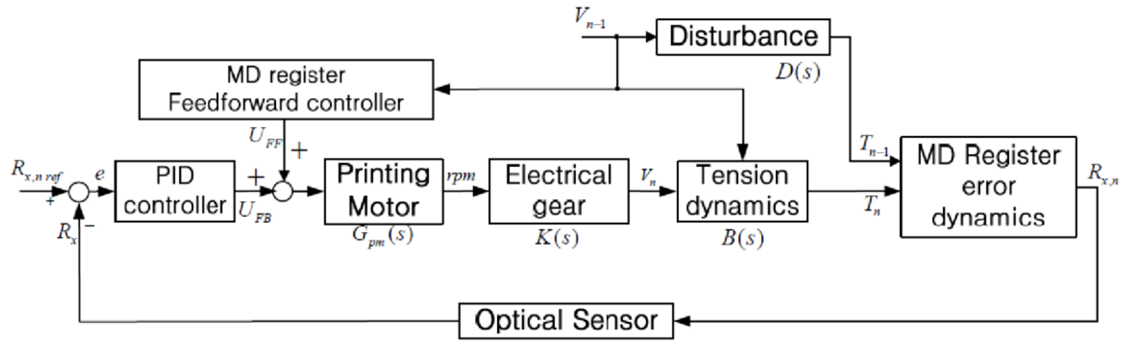

C

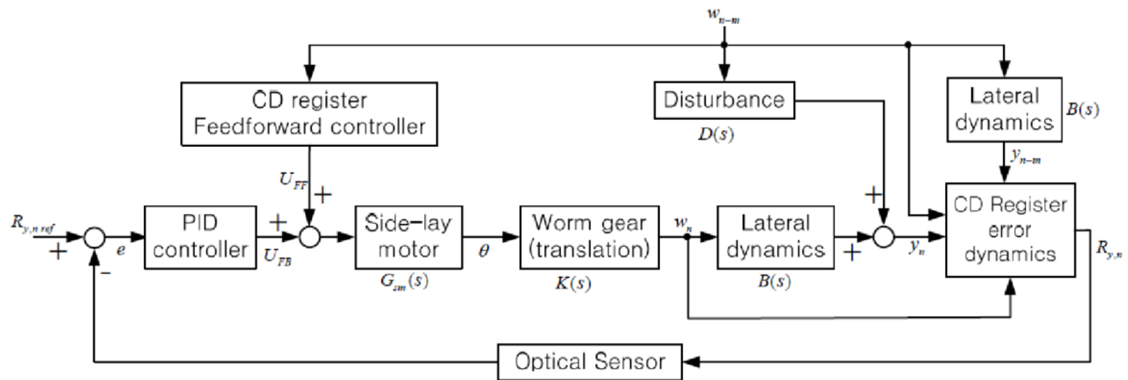

D

Figure 2.16: Register models in MD (A) and CD (B); block diagram of MD (C) and CD (D) register controllers [147]

Apart from building basic register models, K.H. Shin's group also derived mathematical models considering different situations. For instance, Kang et al. [148] derived a MD register model for the hybrid printing systems, which consist of both contact printing and non-contact printing such as gravure and inkjet printing and a linear quadratic controller was utilized to both reject tension disturbances and control for registration error. Lee et al. [149] further analyzed the variations in elastic modulus and web geometry with respect to drying temperature, and correlations among the change in the thermal characteristics of the substrate, tension, and register error were used to developed a model for estimating the overall register error due to thermal and elastic strains. What's more, Lee et al. [150] investigated the inherent characteristics of a R2R

continuous manufacturing system, including the separation of measurement sensor and controller, print quality of the register marks, and flexible nature of the substrates. These inherent factors of register controllers can generate errors which cannot be fully accounted for by theory-based control methods, thus the authors proposed a design for a high-precision register controller, which achieved stable alignment accuracy within ±10-30 μm, through deriving the distance between trigger and measurement sensors, the measurement sensor and controller, and the time interval between measuring the trigger mark and register marks, using high-resolution camera and a load cell at the desired position for measuring the accumulated strain variation.

Other scholars and research groups have also made a significant contribution to develop the register model. As early as 1987, Sugimoto et al. [151] made a mathematical model for a printing press, and simulated the register error by changing printing conditions such as the span length, printing speed, web tension, compensator roller velocity, and print roller radius, then utilized PD control to achieve a registration accuracy within ±0.1 mm.

In a sectional drive system of rotogravure printing presses, where each gravure cylinder is driven by an individual motor, tension perturbations from upstream register control will generate register errors in downstream units. Hence, Yoshida et al. [152] analyzed the dynamics of both tension and register fluctuation, derived a control law based on the nonlinear variable transform of the tension and Lyapunov stability theory, and applied the nonlinear control to an industrial printing press for reducing the downstream propagation of register errors to reduce them to within ±0.1 mm.

Liu et al. [153] derived a MD register model for gravure printing by implementing mass equilibrium equations and considering the fluctuation of tension, speed, and other factors, and achieved a registration accuracy better than 1 mm at a very high printing speed, i.e., 250 m/min.

Later, Liu et al. [154] established a nonlinear model for the multilayer register working principle in gravure printing and linearized this model based on the small perturbation method. Using this they designed a decoupled control strategy based on feedforward control and active disturbance rejection control (ADRC), and realized a high-precision multilayer registration accuracy of between 2 and 20 μm in computer simulation. The control strategy is unique as the feedforward and ADRC controllers actively compensate the register errors caused by the model interferences and unmodeled disturbances in real time, respectively, thus the accuracy of the register controller is greatly improved.

In a printing press with multiple print units as illustrated in Figure 2.17, a primary source of registration errors is the variations in web strain (ε) from one print unit to another. Therefore, web tension variations must be minimized to increase registration accuracy. In this work, registration error is controlled using a compensator roller (x) or by tuning print cylinder angular velocities (ω_1 and ω_2) rather than by regulating the web tension. Seshadri et al. [155] compared compensator based registration control (CRC) with mechanical line shafts (MLS) and print cylinder angular position based control (PARC) strategies with electronic line shafts (ELS), and the CRC strategy resulted in smaller magnitude of tension and registration error propagation. Thus, ELS, i.e., shaft-less drive, together with a compensator roller is recommended for the high-precision registration.

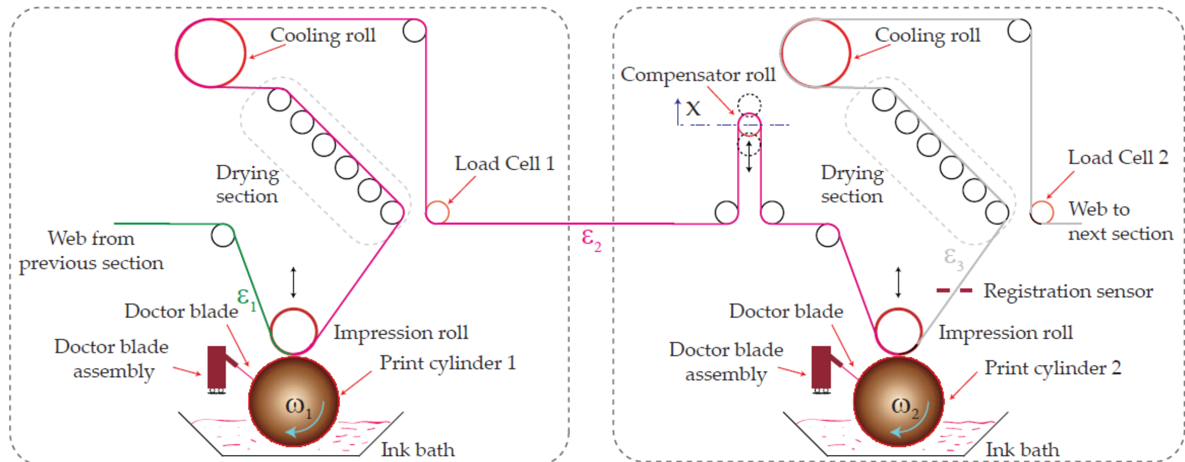

Figure 2.17: Schematic of a rotogravure print unit with two print cylinders using CRC strategy for registration [156]

R2R printing systems under transient conditions are subject to tension fluctuations caused by torque balance of guiding rolls which generate register errors in each printing unit. For this reason, Chen et al. [109] analyzed the dynamics of the speed-up phase in R2R printing and built a mathematical model using conservation of mass and torque balance equations, and then utilized model-based feed-forward PD (MFPD) control to reduce the register errors and maintain the tension at a constant level during the speed-up phase, and a register error within ±0.15 mm was achieved when using the control strategy in an industrial gravure printing press.

Choi et al. [157] proposed a web register control algorithm for a R2R system using a non-linear feedback controller and a set of optimal gains found through a modified genetic algorithm. According to the simulation results, the proposed algorithm achieved a precision of 3 µm register error, and stability with large bandwidth.

Hwang et al. [158] analyzed the process parameters that affect pattern distortion in a R2R NIL system, including substrate bending effects, misalignment angle, thickness of mold and web, and web tension, and then modeled these main parameters into mathematical formulas. Through

compensating for dimensional changes from each parameter, the alignment error was minimized to ~±15 μm in both MD and CD for the area of 200 mm × 150 mm.

Mathematical models improve the performance of vision-based alignment methods, since intrinsic factors such as web strain are constantly monitored, and the alignment systems are more comprehensive than position-related tuning. However, register control becomes much more complicated as the sensing signals are from a vision system, load cell, and control variables are all directly related to web handling i.e. web tension, roller angular velocity, etc.

Researchers	Vision and model-based methods	Alignment accuracy	Throughput
Sugimoto et al. (1987) [151]	MD register model	±0.1 mm in MD	100~405 m/min
Liu et al. (2013) [153]	MD register model	<1 mm in MD	250 m/min
Seshadri et al. (2013) [159]	MD register model	100s μm in MD	50 m/min
Kang et al. (2013) [145]	MD register model	500 μm in MD	60 m/min
Kang et al. (2014) [148]	MD register model	-	180 m/min
Kang et al. (2010) [104]	CD register model	±100 μm in CD	40 m/min
Kang et al. (2011) [146]	OMD register model	300 μm in CD 150 μm in OMD	40 m/min
Kang et al. (2011) [147]	2-D register model	500 μm in MD ±200 μm in CD	40 m/min
Lee et al. (2015) [149]	Dynamic thermal characteristic	-	5 m/min
Lee et al. (2019) [150]	Inherent characteristics	±30 μm	1h (measure)
Hwang et al. (2015) [158]	Dimensional changes	±15 μm	-
Yoshida et al. (2009) [152]	Nonlinear control	±50 μm in MD	100 m/min
Choi et al. (2010) [157]	Nonlinear control	3 μm in MD (simulation)	100 m/min
Liu et al. (2016) [154]	Feedforward + ADRC	2~20 μm in MD (simulation)	200~400 m/min
Chen et al. (2018) [160]	MFPD control	±150 μm	200 m/min

Table 2.5: the performance of the vision-based method using mathematical modelling utilized in current R2R systems

2.5 Modern Control

Based on the vision feedback control, advanced control such as iterative learning control, and additional mechanisms such as active tuning roller and stop-and-go mechanisms were also utilized in multi-layer R2R systems to further improve the alignment accuracy.

In a R2R micro/nano-manufacturing system, registration of the pre-existing features is critical for multilayer fabrication. Non-collocated sensors and web deformation can cause inaccurate feature registration, and direct visual observation helps to circumvent the uncertainty of the feature location on the web. Therefore, Sutanto et al. [161] proposed a two-layer state feedback control architecture, wherein the machine vision provides visual measurement data which correspond to the instantaneous position of the web to the outer loop and inner loop, and $G(s)$, maps the reference signals, i.e., web position, r_1, and web tension, r_2, to the system outputs. The feedback controller is further augmented with norm optimal iterative learning control (NOILC) to improve position tracking and tension regulation of the web, as shown in Figure 2.18.

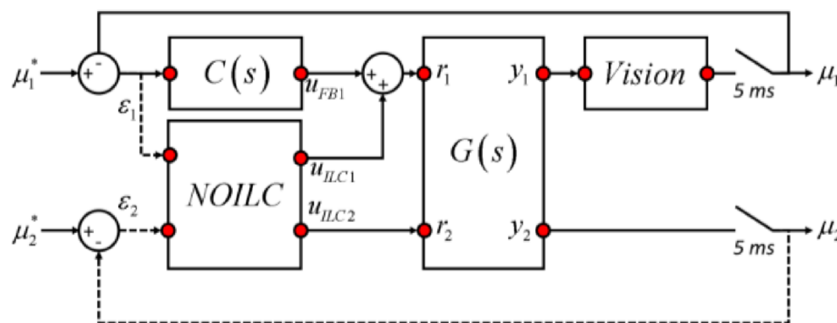

Figure 2.18: Dual state feedback control architecture augmented with NOILC [161]

Some additional mechanisms turn roll-to-roll into roll-to-plate, or turn flexible moving webs into solid static substrates, so that the alignment process becomes much easier and some of the

alignment methods used in semiconductor manufacturing can also be utilized in R2R manufacturing systems.

To avoid time delay in coupled control of speed, tension, and register control, Noh et al. [162] designed a stop-and-go web feeding mechanism rather than the more typical continuous web feeding mechanism. The working principle of the stop-and-go mechanism is illustrated in Figure 20A: during the printing step, the web stops moving, the CCD camera detects the register markers, and the printing stage moves for a precise alignment according to current overlay data before the next roll-to-plate step-and-repeat cycle. This mechanism was adapted into a roll-to-roll gravure offset printing system, as shown in Figure 20B, and average printing overlay errors of 4.2 μm in MD and 2.3 μm in CD were achieved.

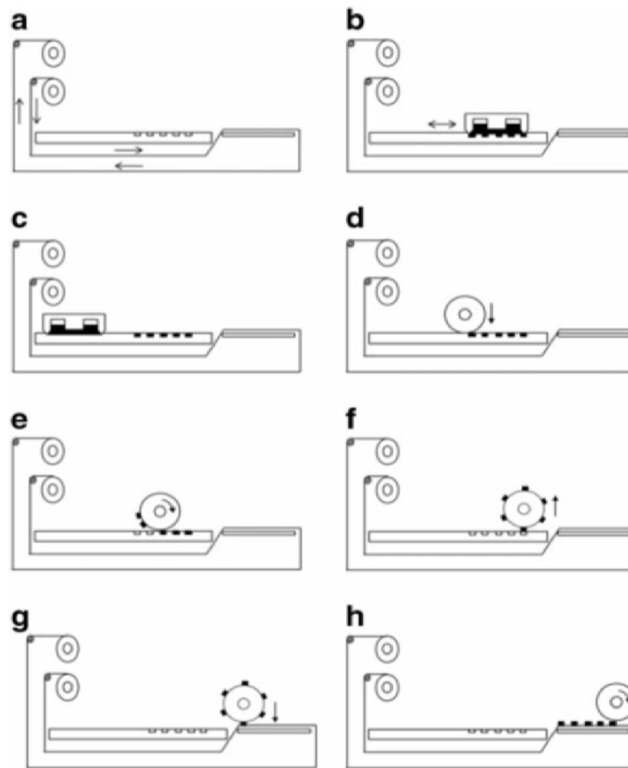

A

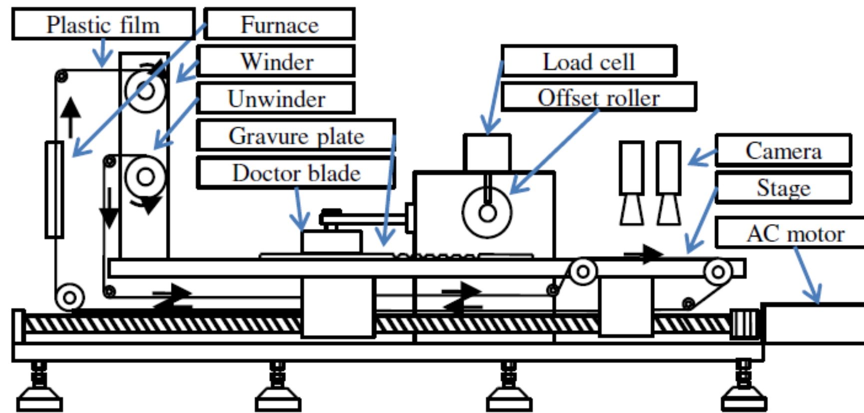

B

Figure 2.19: (A) Working principle of the plate-to-plate gravure offset printing system; (B) Schematic diagram of roll-to-roll gravure offset printing equipment [162]

As flexible webs are inherently susceptible to deformable, the strain induced in webs by the applied tension in R2R handling is a key variable unique to overlay control in R2R manufacturing. Therefore, Zhang et al. [163] investigated the overlay alignment accuracy on PET plastic web using the Azores R2R photolithography system. The R2R overlay process is as follows: First, the web is indexed into the center stepper for exposure and tension is applied, in part, by two vacuum boxes on either end of the system, which helps to manage web slack and permit ease of motion of the substrate vacuum chuck on the stage, as shown in Figure 2.20B. Next, a camera captures the alignment marks, which have been exposed and developed on the substrate along with the first pattern layer, as shown in Figure 2.20A, then a data analysis software compares the measured alignment mark positions with target positions and calculates a set of correction values - *X*, *Y*, rotation, *X*-scale, *Y*-scale and the angle between *X* and *Y*. Finally, the overlay patterns are exposed with the adjusted magnification of the lens of the image system and the step distance of the stage. Meanwhile, appropriate tension is applied to the web to help maintain the flatness of the substrate. Using only three global overlay alignment markers, the achieved overlay accuracy was 2 µm.

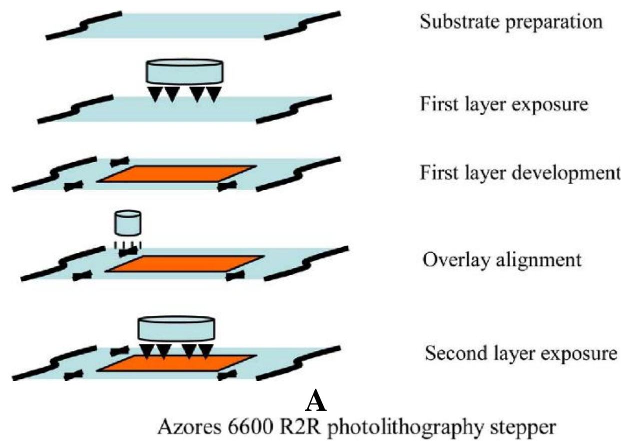

A

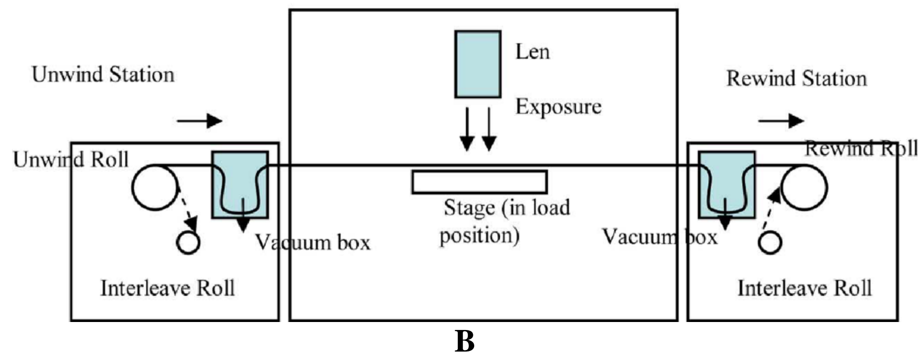

B

Figure 2.20: Schematic of (A) process flow of overlay alignment, and (B) the R2R processing of substrate (side view) [163]

Another approach to account for the challenges due to the inherent web flexibility, developed by Chang et al. [164], is a successive chucking mechanism for web handing and a layer-to-layer overlay of ±5 μm on a 500 mm-wide film was achieved in a continuous R2R printing process. Figure 2.21 shows the schematic of the deformation-free successive chucking mechanism which can remove wrinkle or tension irregularities in the web. This chucking mechanism achieved a positioning deviation in the flexible web that was within ±0.8 μm with repeatable chucking.

Further, Kim et al. [165] proposed a novel precision reverse offset printing system and presented methods of controlling synchronization and printing force to reduce positional errors caused by web flexibility. After compensating for master registration error, a position accuracy of 1.12 μm and 0.70 μm in the CD and MD respectively was achieved.

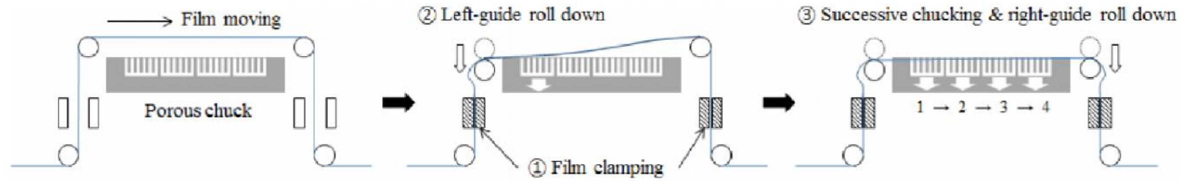

Figure 2.21: Schematic of the successive chucking mechanism [164]

On the other hand, some additional mechanisms introduce more degrees of freedom for correcting the position of the web or print roller, such as the multi-axis positioner for inkjet printer in [118]. Choi et al. [119] implemented a precise lateral control system for R2R fabrication process of organic photovoltaic (OPV). A line pattern printed using inkjet printing rather than the web edge was used as a reference mark for CD control. CD displacement of the pattern was measured with a camera and calculated with a pattern recognition algorithm. A PID controller was implemented and results indicated that the lateral displacement of a web may be controlled within ±50 μm with 200 m of web transfer at the web speed of 15 m/min.

Jung et al. [120] utilized an active motion-based roller (AMBR) in R2R gravure printing to reduce register error, as shown in Figure 2.22A, which is a 1-DOF mechanical device and can compensate for web elongation without introducing undesired tension disturbance. Figure 2.22B shows the block diagram of the MD register control system, where the register error measured by the optical sensor is amplified and used as a reference displacement for the AMBR controller. The AMBR provides precise simultaneous control of the tension and span length by controlling the dancer roller motion with micrometer precision, thereby reducing the register error. Experimental results indicated that the overall register error can be controlled to within ±15 μm in this work.

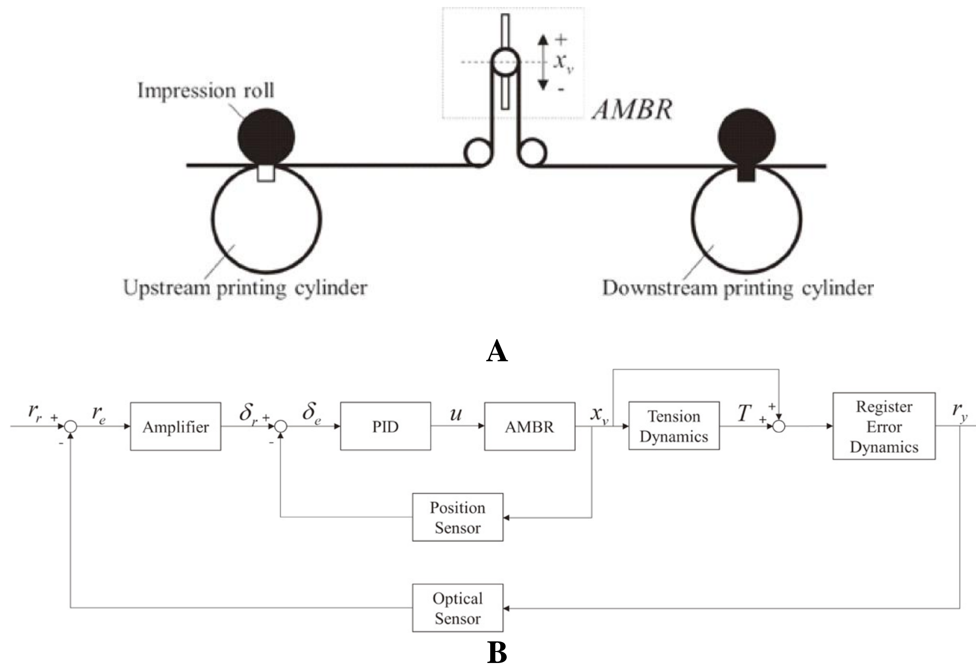

Figure 2.22: (A) Configuration of the register control system using the AMBR; (B) Block diagram of the MD register error controller using the AMBR [120]

Group	Advanced control & mechanisms	Alignment accuracy	Throughput
Sutanto et al. (2013) [113]	Iterative learning control	-	0.3 m/min
Noh et al. (2013) [114]	Stop-and-go mechanism	4.2 µm in MD 2.3 µm in CD	3 m/min
Zhang et al. (2009) [115]	R2R photolithography	2 µm	0.2 m/min
Chang et al. (2015) [116]	Successive chucking mechanism	±5.0 µm	0.6 m/min
Kim et al. (2016) [117]	Synchronization and printing force control	0.70 µm in MD 1.12 µm in CD	0.6 m/min
Choi et al. (2014) [119]	Lateral control system	±50 µm in CD	15 m/min
Jung et al. (2018) [120]	Active motion-based roller	±15 µm	2 m/min

Table 2.6: Summary of the performance of vision-based methods with advanced control or mechanisms utilized in current R2R systems

2.5.1 Summary

Three categories of alignment methods for multi-layer R2R manufacturing systems were introduced and discussed: (1) Scale compensation methods are "passive" and focus on compensating deformations of the flexible substrates. They are important for obtaining single-layer accurate features and achieving high multi-layer alignment accuracy in R2R manufacturing. However, they cannot address the alignment errors due to external disturbances and stochastic errors. Therefore, they are often utilized with other "active" alignment methods. (2) Self-aligned methods are also "passive" and achieve relatively high alignment accuracy without using alignment systems. They utilize the uniqueness of the manufacturing process, material properties, and device structures to achieve high-resolution self-alignment. However, that is also why they are only suitable for few manufacturing methods, and simple structures. (3) Vision-based methods are "active" and the most versatile and widespread technique for layer-to-layer alignment. They use optical imaging systems to monitor the web position or misalignment, then actively adjust or compensate the alignment errors by tuning the position of the manufacturing tools. Though the alignment systems are complicated and costly, they have the possibility to fabricate arbitrary complex 3D structures and are the mainstream in multi-layer R2R manufacturing systems.

Vision-based alignment methods can be applied to all kinds of R2R manufacturing systems. Different manufacturing systems require different compensation methods. Table 8 summarizes the compensation methods for multi-layer alignment in R2R manufacturing systems. Conventionally, a compensator roller adjusts the span length between two print cylinders, thus compensates the alignment errors in MD can be controlled directly by tuning the phase and angular velocity of the print cylinder. On the other hand, a lateral guide or web guide is used for cross-machine direction registration. Also, a side-lay motor with worm gear, or a linear motor installed on the plate cylinder

controls the axial movement of the plate cylinders and regulates the CD register. For non-contact manufacturing methods, compensation could be much easier. For example, a stepper or mask aligner moves the mask into alignment with the substrate in R2R photolithography, or a planar stage adjusts the printer head according to the alignment errors in inkjet printing. Using extra mechanisms such as chucks, flexible substrates could be treated as a plate, then precise multi-axis stages can tune the position of the substrate table for multi-layer alignment, just like roll-to-plate. In above-mentioned special situations, it is convenient for them to correct the alignment errors in planar DOFs, i.e., X, Y, and θZ. However, submicron level correction cannot be achieved by utilizing traditional compensation mechanisms. Recently, flexure-based multi-axis positioner were implemented into R2R systems for high-accuracy alignment. Moreover, synchronizing the web speed, alignment system, and compensators can further improve the alignment accuracy.

2.6 Measurement Challenges Towards Multilayer R2R Nanomanufacturing

In practice, a combination of measurement approaches is necessary to measure critical parameters such as overlay error and regulate process parameters to maximize yield in based HVM, with fast acquisition methods like optical metrology and DBM dominating in-line and real time process control and slower methods such as SEM or AFM used to verify critical dimensions

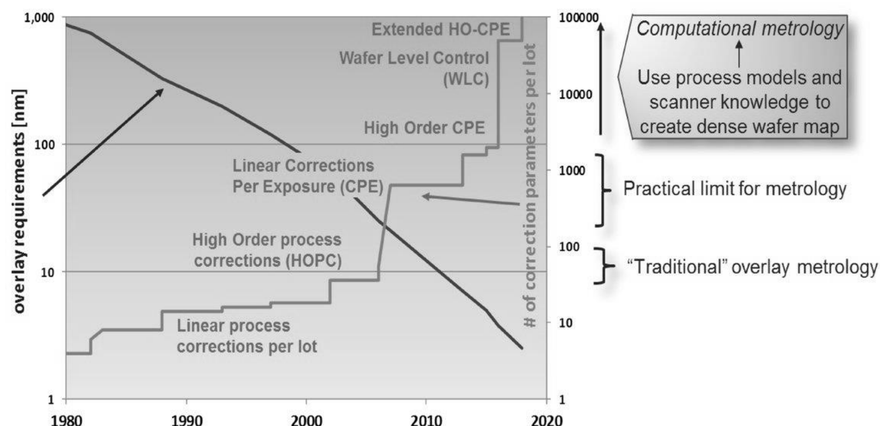

Figure 2.23: Silicon wafer manufacturing overlay requirements and process corrections per lot with respect to time

within specific sensitive areas of the pattern and generally used to inform lot-to-lot or run-to-run process control. With ever increasing demands on these critical dimensions, a corresponding increase in the demand for metrology performance and throughput is also seen. Figure 2.23 roughly quantifies this evolution as related to the overlay requirements in wafer based fabrication. Similarly, as R2R nanomanufacturing increases in scope and volume, there exist equally significant and challenging requirements for R2R process metrology. The difficulty in extending existing wafer-based approaches lies in the inability to quickly and periodically take samples out of a R2R line for inspection without disturbing or negatively impacting the speed of the manufacturing process as a whole. This delay in sampling ability for traditional SEM and AFM tools when applied to R2R nanopatterning practically excludes the use of one of the most effective new process control methods in the wafer semiconductor manufacturing toolbox – hybrid metrology [166].

In a hybrid metrology scheme, multiple measurement sources, each with disparate advantages and disadvantages inherent to their sampling approach, are used as inputs to a machine learning algorithm to both improve throughput and decrease overall measurement uncertainty [167]. Figure 2.24 outlines the basic structure of both traditional and hybrid metrology approaches. In this typical application the ease of sampling of optical inspection is combined with a slower but higher resolution high vacuum SEM tool to bring the best of bother worlds. Applying hybrid metrology to R2R nanomanufacturing would bring about a significant increase in overall performance and allow for the useful implementation of increased measurement and process correction speeds. The overall goal of this approach is the creation of an algorithm to seamless integrate information from multiple tools in order to inform automated process regulation [168]. This could thus also aid in improving yields to the point of economic viability for R2R processes,

often in their nascent stages. However, the incompatibility between available high-resolution measurement tools and a R2R architecture has prevented widespread adoption of hybrid metrology frameworks in literature.

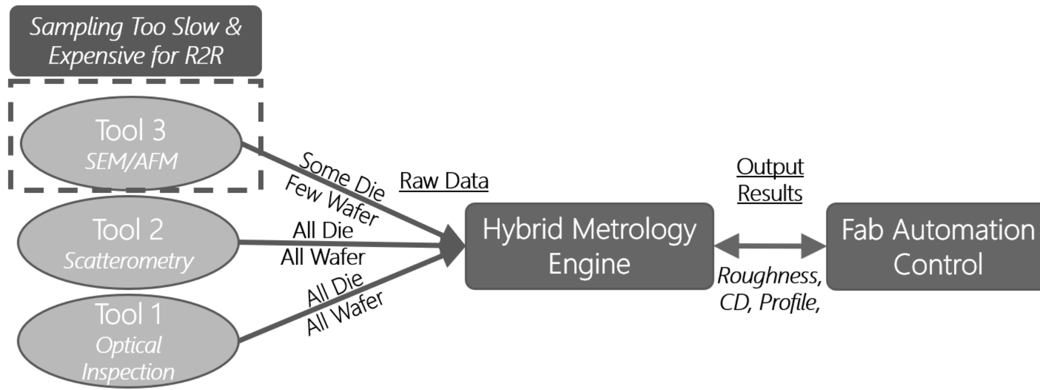

Figure 2.24: Basic hybrid metrology schema involving three tools of varying precision and throughput

CHAPTER 3 – INITIAL R2R METROLOGY PROTOTYPE DESIGN

To address this gap in measurement capabilities for R2R nanofabrication and accomplish the topography sampling and eventual process tuning typically handled by out-of-line AFM and SEM measurement, a new metrology framework was proposed and a proof-of-concept prototype constructed to implement the sc-AFM in a R2R environment [169]. While compared to some traditional AFM tools the cantilever actuation range of the sc-AFM is quite high, ~10 μm, a method to regulate both the vertical separation between sc-AFM and the sample surface on the mm-scale is required in order to easy enable tip exchanges and prevent destructive tip-sample crashing due to any measurement roller eccentricity or runout. Further, as a stand in to demonstrate the compatibility of this framework with respect to true in-line operation with fab modules, full regulation of a flexible web including velocity and tension control must also be accomplished by the prototype tool.

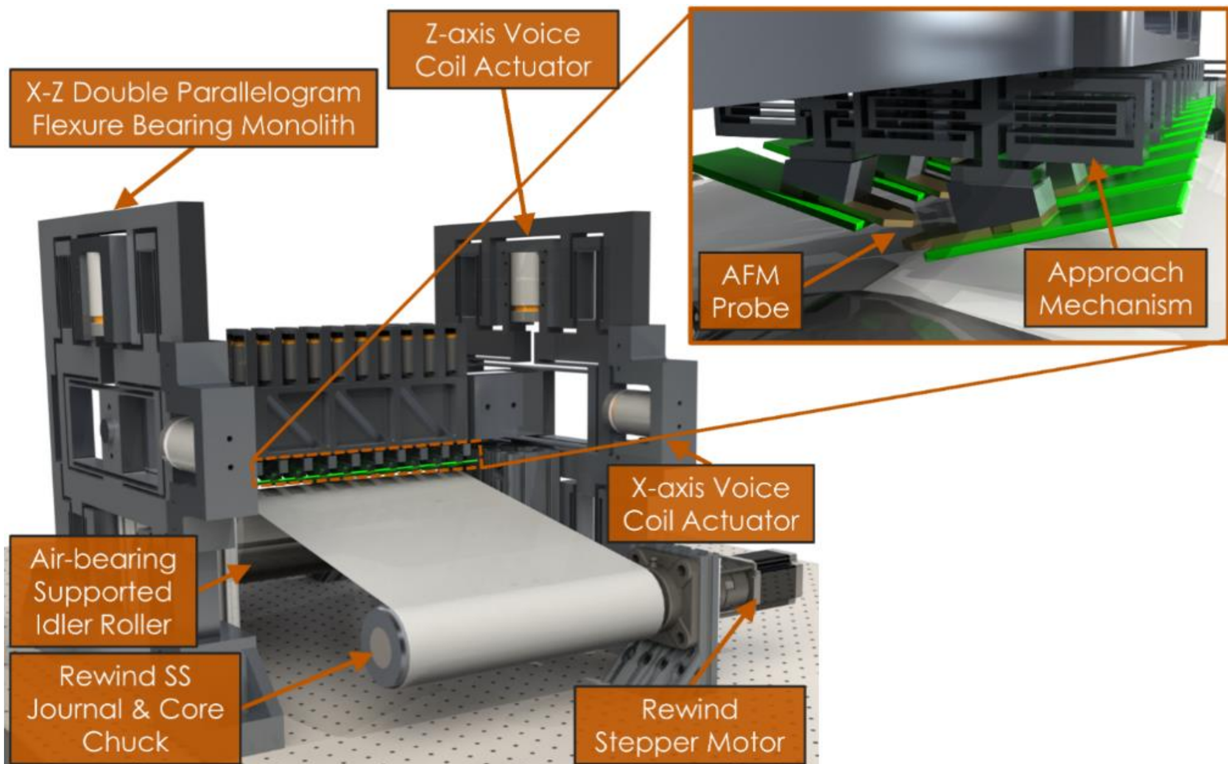

Figure 3.1: CAD rendering of initial tool design with a proposed throughput-maximized configuration of parallel sc-AFM probes

This tool configuration was initially intended to operate in a step-and-scan fashion with a single measurement cycle time budget to match that of an existing prototype roll-to-plate jet and flash nanoimprint lithography tool – ~60 seconds (Molecular Imprints LithoFlex 100). As such, the sc-AFM must be retracted and re-approached after each scan to allow for web movement, necessitating a high-speed and nanometer scale precision positioning system. A prototype was designed to include both these two principal sub-systems – the web handling subsystem and the sc-AFM positioning subsystem – and is shown with major components captioned in the render in Figure 3.1. In this initial CAD model, the maximum overall throughput was explored, however the preliminary prototype was intended to house only one sc-AFM probe.

3.1 WEB HANDLING SUBSYSTEM

Regulation of the flexible substrate to be measured is accomplished by the web handling subsystem. To simplify control of web position, velocity, and tension as much as possible for this prototype, the subsystem was designed to consist of just three rollers: an unwind stand, idler metrology roller, and a rewind stand. A rough graphic of this subsystem layout is shown in Figure

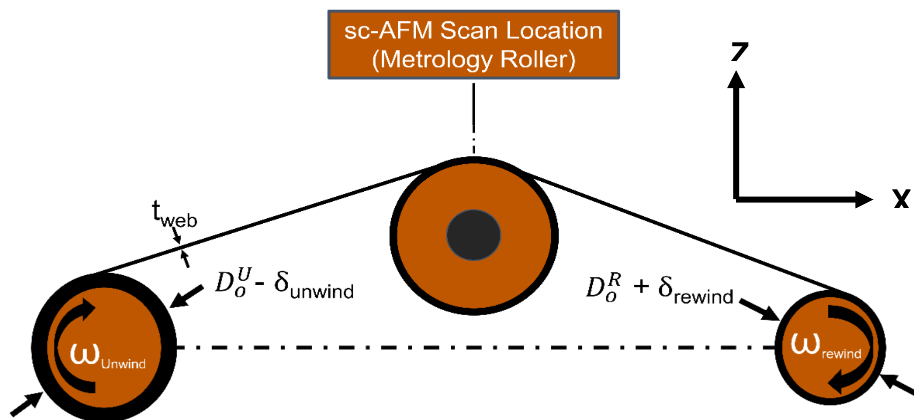

Figure 3.2: Diagram of the Geometric Layout of the Web Handling Sub-system showing unwind and rewind diameters, angular velocities, web path, and the location of scanning

3.2 where web direction corresponds to the x-axis and the vertical direction from web to sc-AFM the z-axis. At the critical sc-AFM scanning location the web is supported by a 100 mm diameter stainless steel idler roller supported by a radial air bushing and a thrust and radial air bearing at each end respectively. Further, as can be seen in Figure 3.3, the unwind and rewind stands are constructed identically, consisting of a smiple extruded aluminum body with flange mount roller bearings supporting a stainless steel journal to which a pneumatically actuated, expanding core chuck is attached via C-clamps. This extrusion is then bolted directly to the optical table via angle brackets. Driving the stands is a simple timing belt transmission actuated by a brushless DC stepper motor and controlled such that the difference in drive velocities tensions the web.

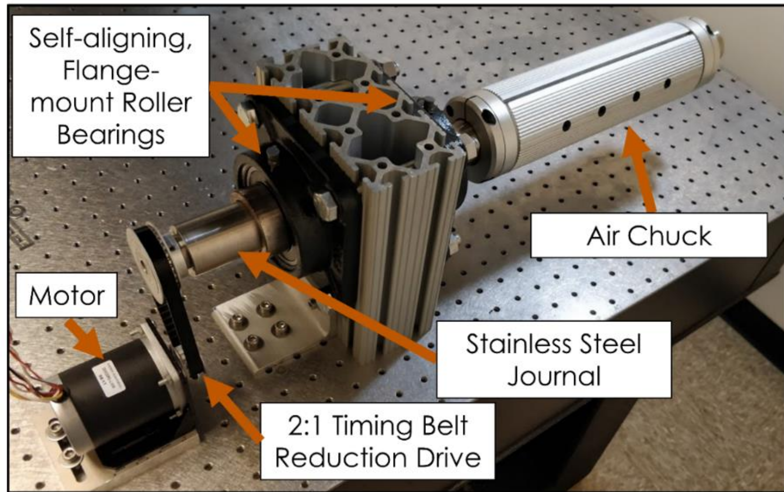

Figure 3.3: Initial prototype unwind/rewind stand assembly

3.2 sc-AFM Nanopositioning Subsystem

The most critical component of the prototype tool is the sc-AFM nanopositioning subsystem. This subsystem must regulate the position of the sc-AFM such that it can retract a large enough distance to prevent destructive web-tip crash during startup, high speed web movement, or when replacing the sc-AFM chip itself. Further, the subsystem must sufficiently isolate the sc-AFM from external disturbances such that the cantilever does not contact the web. This is accomplished by means of two coupled positioners, one which moves the gantry arm to which the sc-AFM is

attached and one which regulates fine sample approach. These systems each consist of a double parallelogram flexure mechanism coupled to voice coil force actuators, both of which can be seen in Figure 3.1 [39]. This layout allows for any future expansion of the tool to multiple probes without a heavy and expensive system for mechanically leveling multiple probes across the width of the web.

For the gantry arm positioner, position feedback is provided by a set of two perpendicular capacitance sensors on each flexure monolith while for the fine sc-AFM positioner the cantilever deflection signal from the piezoresistor on the sc-AFM is used to control approach. Control of these systems is calculated and coordinated by a field programmable gate array (FPGA) based real-time control system (NI cRio-9032) which both deterministically acquires position data sc-AFM scan data and calculates and records control system outputs.

The design of the flexure geometry was determined by parametric modeling of ideal double parallelogram flexure mechanisms (DPFMs), as shown in Figure 3.4, through simple beam theory. The intent of this guess-and-check process was to ostensibly maximize the stiffness of the Z- and X-axis flexure mechanisms while also meeting minimum range requirements. In this case a relatively significant payload, or moving mass, is required to move the entire sc-AFM gantry. As such, minimum flexure depth (H) of 25.4 mm and flexure thickness (B) of 1.25 mm was enforced. Eq. 3.1 through 3.4 describe how flexure stiffness and maximum range can be derived. The chosen geometric design variables are detailed in Table 3.1.

$$EI\,Y'' = M + FL \tag{3.1}$$

$$k_z = \frac{24EI_x}{L_x^3} \tag{3.2}$$

$$k_x = \frac{48EI_z}{L_z^3} \tag{3.3}$$

$$\mathrm{Disp}_{\mathrm{Max}} = \sigma_y * \frac{L^2}{3E*H*FOS} \tag{3.4}$$

These linear parametric equations, however, can neither easily not accurately estimate dynamic response of the flexure stages. Therefore, finite element analysis (FEA) methods (ANSYS Mechanical ADPL) were utilized to verify resonant modes, especially those which cannot be controlled (i.e. in any direction other than the primary axis of motion of the individual flexure stage). Further, the stiffness of each access of the as-designed flexure monolith is evaluated to both verify the parametric model and ensure the yield stress of the chosen material, 6061-T6 aluminum,

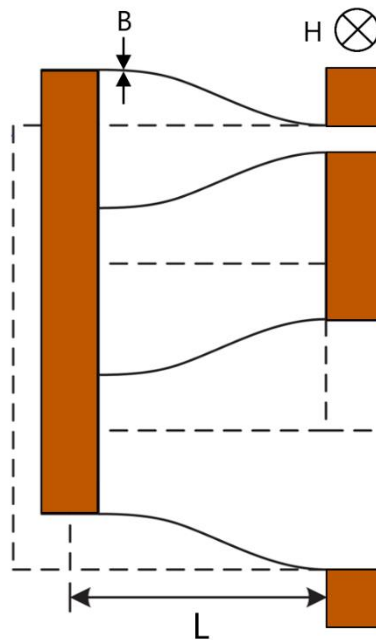

Figure 3.4: Flexure mechanism geometric layout

Parameter	Value	Parameter	Value
L_X	80 mm	K_X	46.1 N/mm
L_Z	95 mm		
H_X	25.4 mm	K_Z	32.7 N/mm
H_Z	25.4 mm		
B_X	1.5 mm	Maximum Range (X)	2.8 mm
B_Z	2 mm		
FOS	3	Maximum Range (Z)	4.18 mm

Table 3.1: Double parallelogram flexure mechanism design variables

is not exceed within the given safety factor of 3. The results of this static simulation can be seen in Figure 3.6.

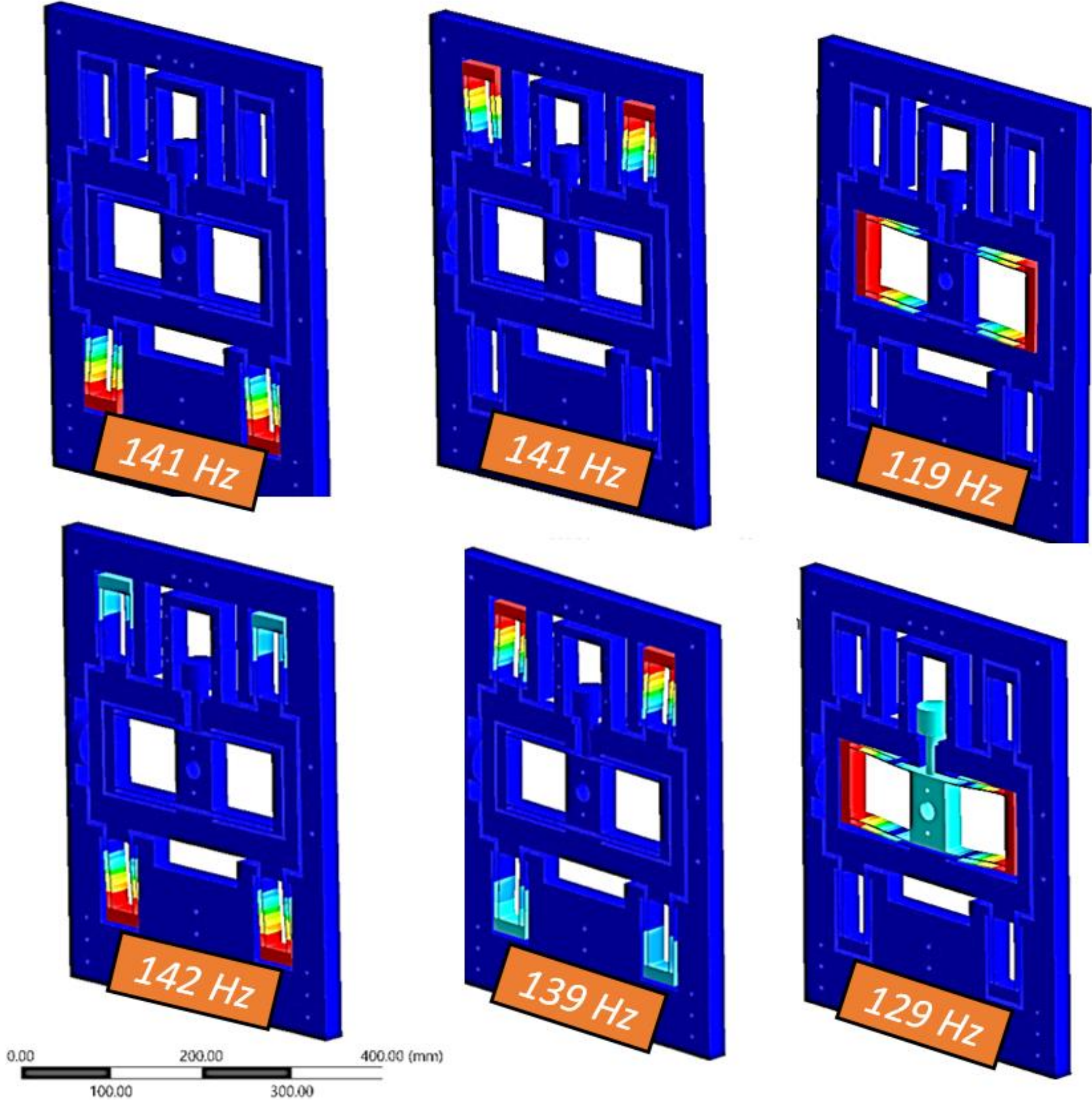

Figure 3.5: FEA simulation of out of plane flexure resonant modes

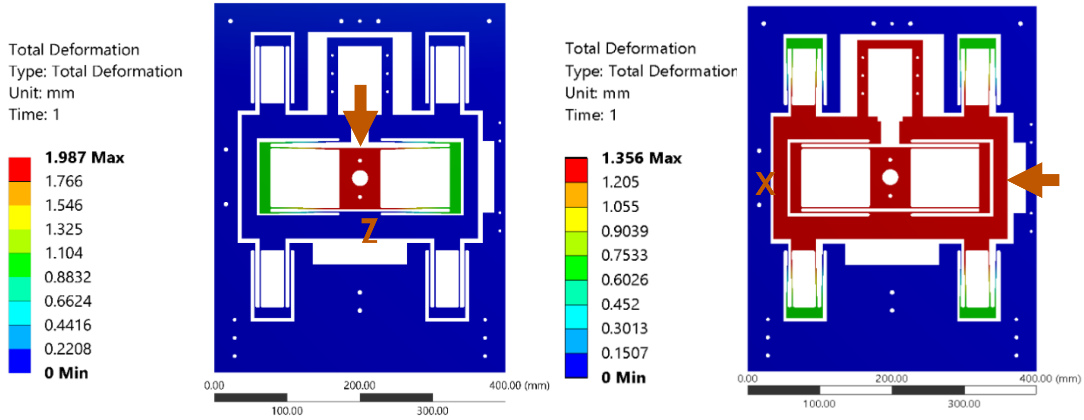

Figure 3.7: FEA Simulation of static maximum range and stiffness simulation of Z-axis (left) and X-axis (right) linear flexure bearings

Despite the enhanced accuracy of FEA methods, by fabricating the flexure plates through abrasive water jet cutting (AWJC), an additional source of error is introduced – kerf. This taper in the cut edge alters the moment of area of the flexure beams, which was assumed to be perfectly rectangular in the previous two modeling approaches. An example of this effect in one of the as-fabricated Z-axis DPFM modules is shown in Figure 3.7. The effect of this taper on the moment of area of the beams can be expressed as a correction factor for both the analytical and FEA calculated stiffness and first resonant mode as shown by Eq. 3.1 through 3.4.

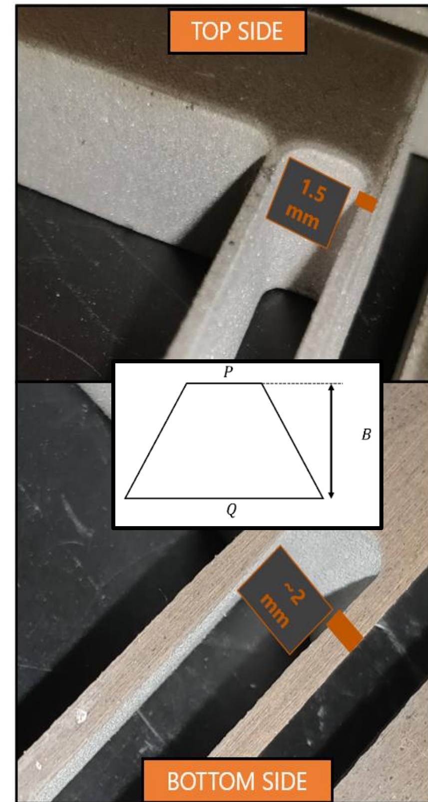

Figure 3.6: Kerf, or vertical taper, in the as-fabricaed flexure beams

$$I_{yc} = B * (P + Q) * \frac{P^2+Q^2}{48} \quad (3.5)$$

$$Correction\ factor\ (Cf) = \frac{I_{trapezoidal}}{I_{rectangular}} = \frac{(P+Q)(P^2+Q^2)}{4B^3} \quad (3.6)$$

$$K_{corrected} = K_{rectangular} * Cf \quad (3.7)$$

$$f_1^{kerf} = sqrt(Cf) * f_1 \quad (3.8)$$

Kerf Corrected Analytical		Kerf Corrected FEA		Experimental	
Parameter	*Value*	*Parameter*	*Value*	*Parameter*	*Value*
K_X	68.04 N/mm	**K_X**	74.01 N/mm	**K_X**	75.018 N/mm
K_Z	33.29 N/mm	**K_Z**	34.85 N/mm	**K_Z**	33.138 N/mm
First Mode X	23.6 Hz	**First Mode X**	24.6 Hz	**First Mode X**	20.83 Hz
First Mode Z	41.4 Hz	**First Mode Z**	42.4 Hz	**First Mode Z**	36.51 Hz

Table 3.2: Kerf corrected parametric and FEA values vs. as-fabricated flexure modules

With the kerf correction, we can see that the models are more in line with experiment, however the actual kerf is a function of the tool pathing, speed, and location within the cutting bed of the AWJC tool, so the overall effect is that without automated coordinate measuring machine data of kerf along each individual beam, the corrected values remain an estimate.

3.3 Proof-of-Concept Results

Initial results from the proof-of-concept prototype, detailed in Figure 3.8, focused on evaluation of the nanopositioning subsystem and validation of the step-and-scan metrology acquisition framework. Design goals called for positioning performance to exceed the minimum pixel size of sc-AFM scans, ~100 nm, a cross-coupling ratio between X and Z axis of the gantry nanopositioner that would allow for independent control of each axis, ~ -35 dB, and a first resonance mode for each positioning axis which exceeds double the theoretical maximum approach-measure-retract cycle as limited by the sc-AFM scan speed (0.15 s per line), 13.3 Hz [170]. By achieving these design goals, the aim is to minimize the contribution of low frequency noise from the surrounding environment to positioning noise floor in addition to maximizing the eventual bandwidth of the positioning sub-system.

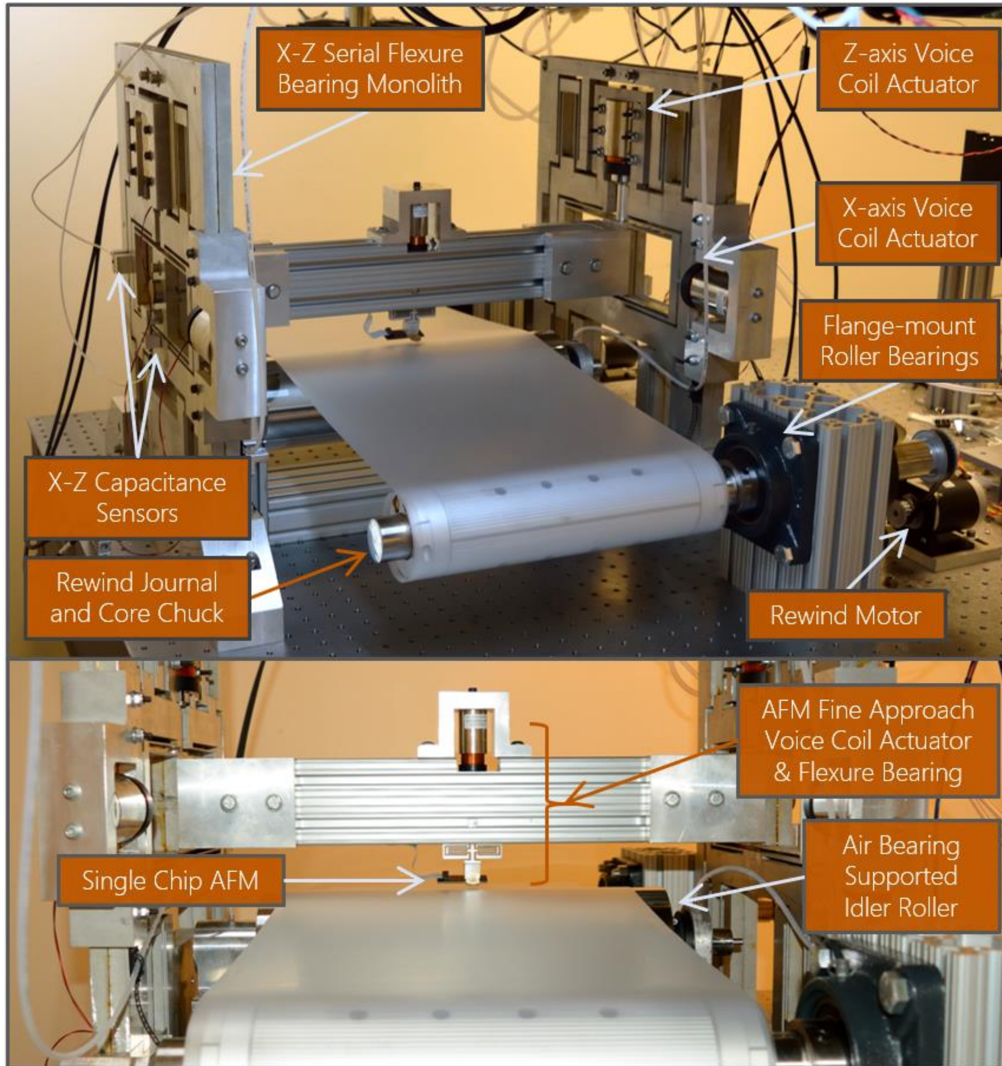

Figure 3.8: Photographs of the initial concept prototype with major sub-systems labeled

3.3.1 Open-loop Nanopositioning

Open loop results for the gantry nanopositioner, which employ an experimental setup as outlined in Figure 3.9, shows that a 2σ confidence interval for sc-AFM position will exceed the ±

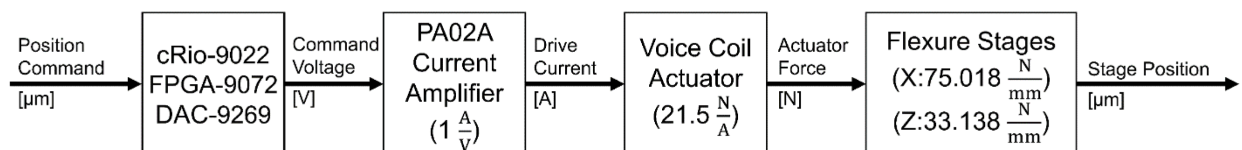

Figure 3.9: Initial experimental power electronics and control apparatus

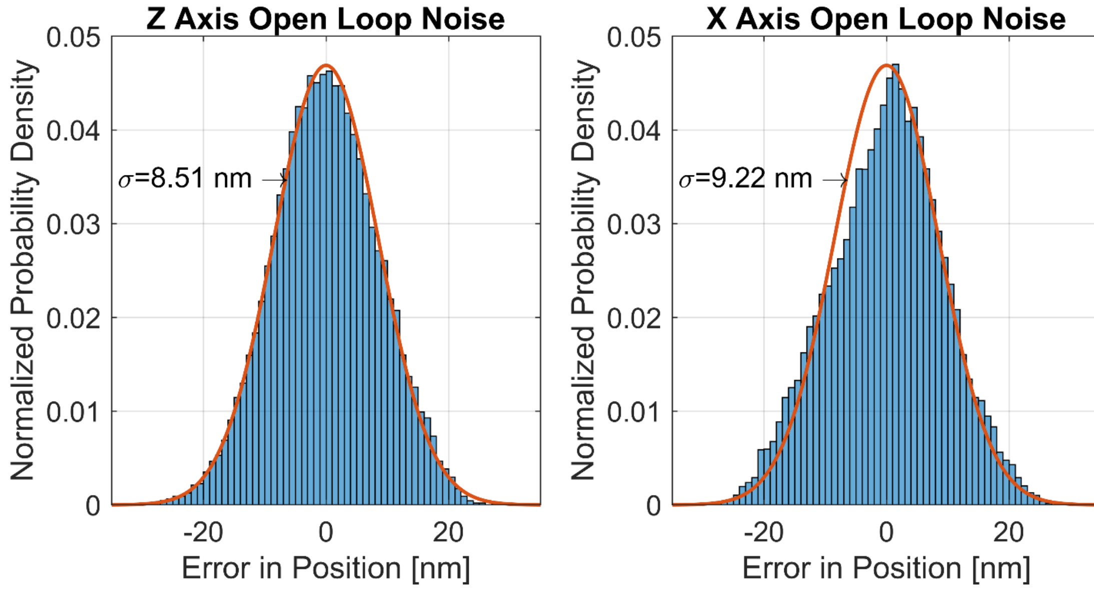

Figure 3.10: X- and Z-axis open loop noise floor in a single DPFM monolith

50 nm goal, with the Z and X axis achieving 2σ envelopes of ± 17 nm and ± 18.5 nm respectively, as shown in Figure 3.10. Further, in a cross-coupling experiment where one axis is held at a constant voice coil force while the other axis is stepped through the 200 um range of the capacitance sensor, the measured ratio between desired and parasitic motion is shown to fall significantly below the -35 dB necessary for decoupled control as shown in Figure 3.11, where the confidence interval listed is the 2σ interval. This is critical as control of gantry positioner is greatly simplified if each DPFM monolith it can be treated as two separate dynamic systems, one for each motion axis, as opposed to a single, coupled system. Lastly, an experimental identification was carried out to measure the frequency response of each axis of the fabricated double parallelogram

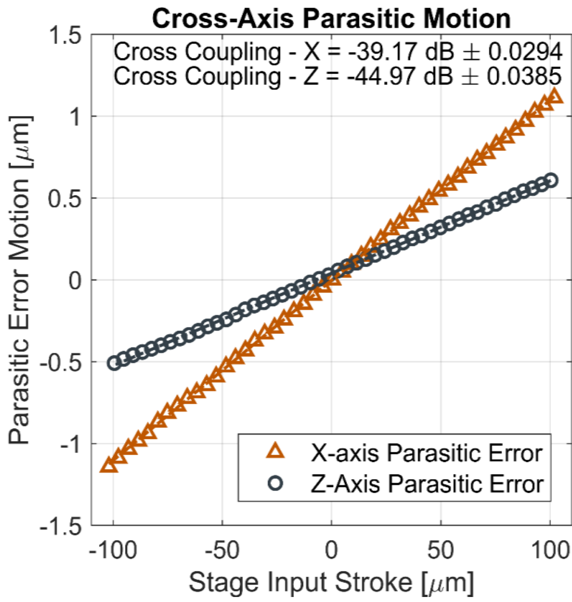

Figure 3.11: Cross-coupling ratio between independent axis within an individual flexure monolith

flexure mechanism monolith. To quickly measure frequency dependent effects over a relatively broad spectral band, a white noise signal was input to each axis of the system and output response measured. Then, using Welch's averaged periodogram method, a frequency response function is reconstructed from the experimental data [171]. This bode response is shown in Figure 3.12, and it demonstrates that both gantry positioning axis achieve a first resonance peak, a major limiting factor in high bandwidth positioning performance, is greater than the desired 13.3 Hz for each axis.

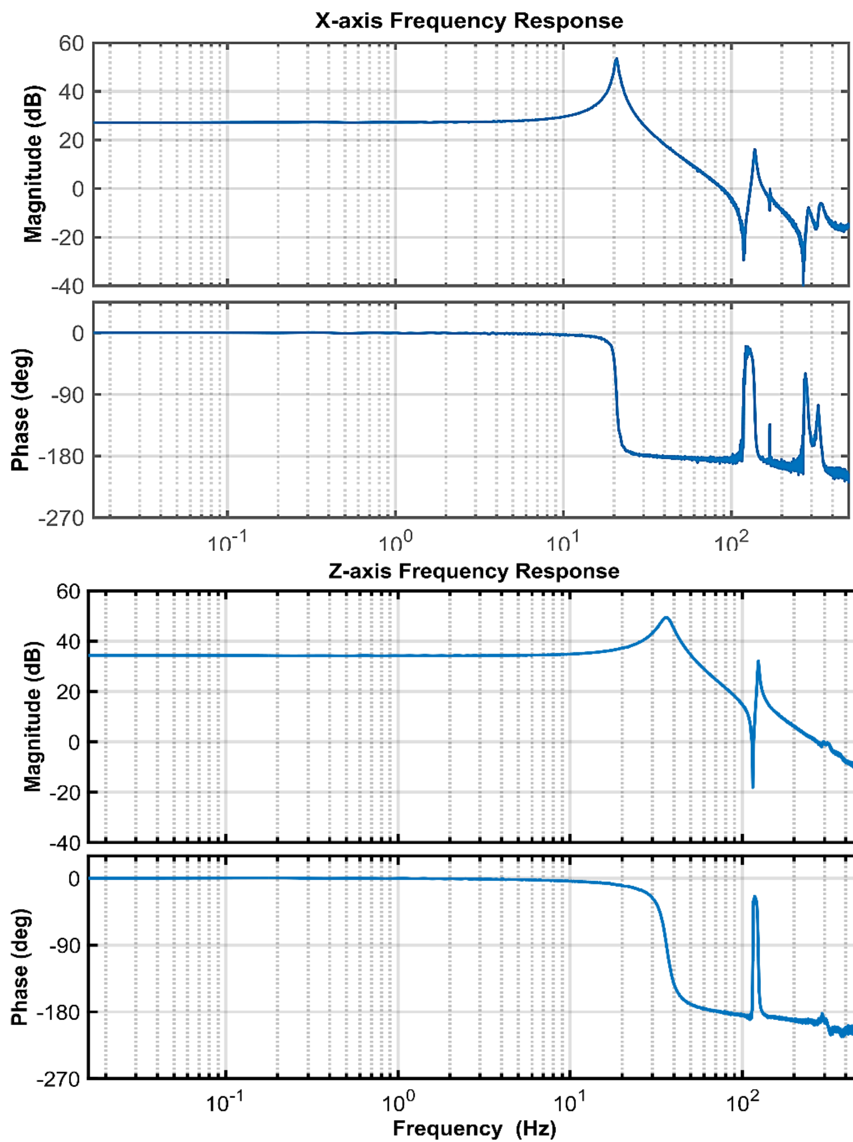

Figure 3.12: Experimental system ID Bode response of X- and Z-axis DPFM flexure bearings

3.3.2 Step-and-scan Operation

The final tests of the proof-of-concept prototype revolved around demonstrating the periodic, but discontinuous, step-and-scan sampling of nanopatterns on a flexible polycarbonate web. The first test artifact considered was chosen for its ease of acquisition, minimal (zero) cost, and multi-scale hierarchical structure – the wing of a queen butterfly. On this biological nanomaterial, the color seen in Figure 3.13 comes not from a naturally occurring pigment, but the diffraction of incident visible light due to the nanostructures which make up the wing. To provide a measurement baseline, SEM scans at micro and nanoscale magnification levels are taken to qualitatively measure feature sizes and layout of the nanopatterns. While precisely the same location is not scanned for both the SEM and sc-AFM measurements, the structure is regular enough that variation between each "feather" should be relatively minimal, and both samples were taken from the same wing specimen. Figure 3.14 shows both how the specimen was adhesively mounted to the polycarbonate web and the

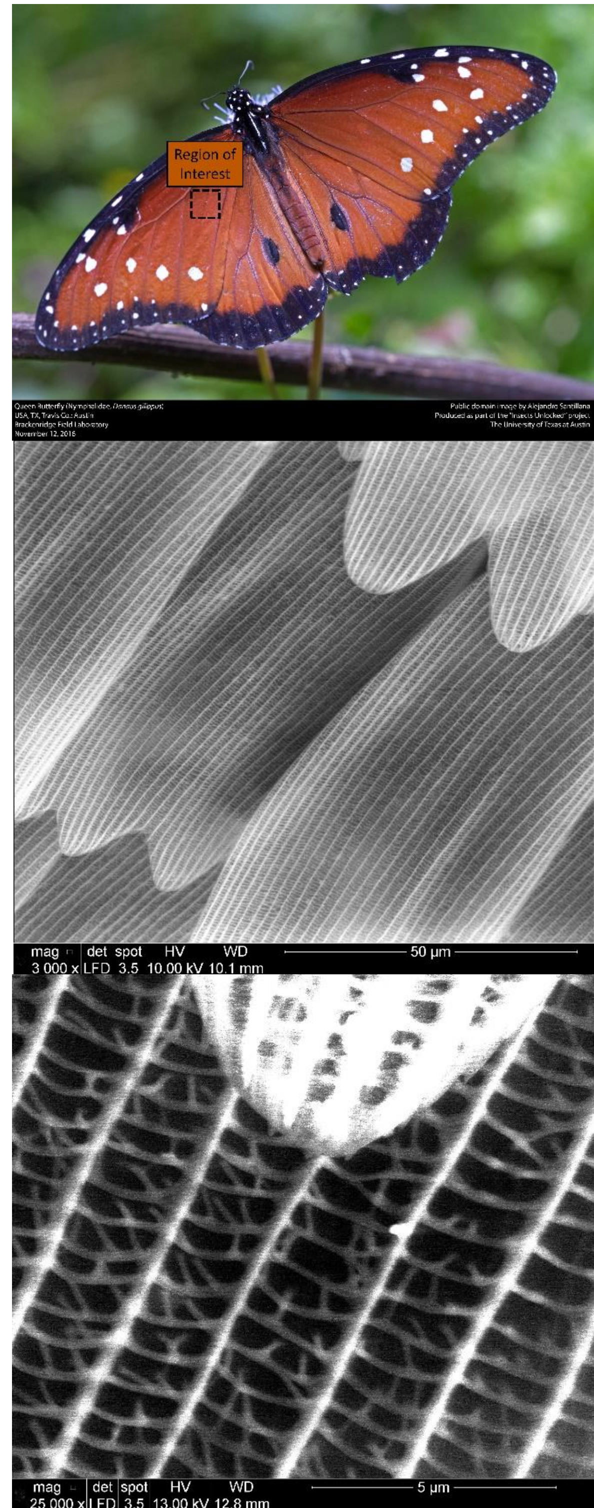

Figure 3.13: Photograph and SEM micrographs of the nanostructures which make up the wing of the queen butterfly

subsequent sc-AFM scans of the surface of a single scale on the butterfly wing. As can be seen, the wing ribs in the transverse and longitudinal directions in the SEM and the sc-AFM images appear to match. A zoomed in subset of the sc-AFM scan is reproduced below where each colored line in the figure corresponds to a line scan topography shown in the plot to the right. As can be seen, features ranging from the micrometer scale to the nanometer scale in both lateral and vertical dimension are successfully resolved.

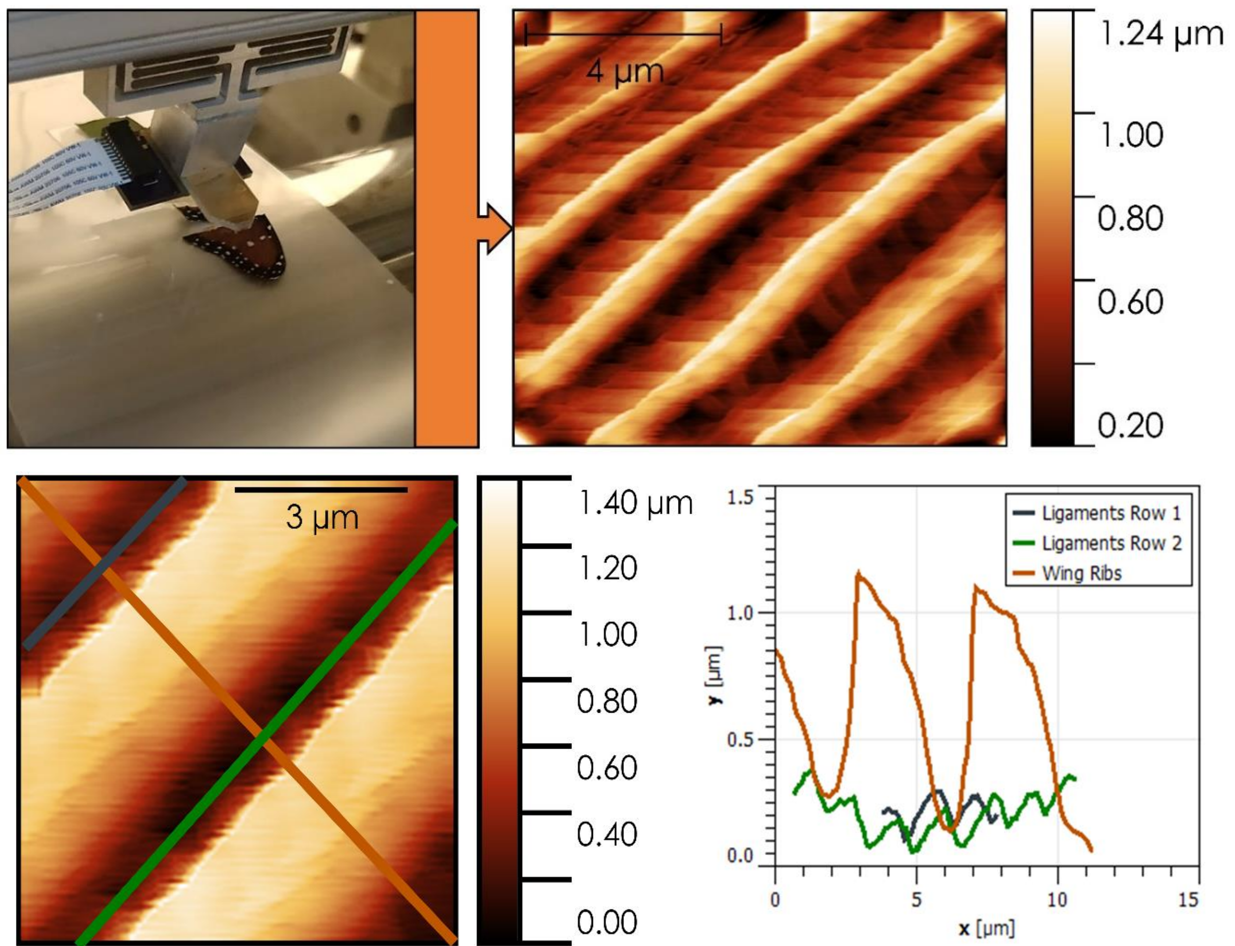

Figure 3.14: Detailed view of sc-AFM scans of the wing of a queen butterfly

To further test the prototype, SEM and sc-AFM measurements of the same ~150 nm tall nanoposts on a polycarbonate web are shown in Figure 3.14. Comparison to both the SEM image shown and a tabletop AFM showed that the sc-AFM data matches the expected fabrication

parameters of the features. A variety of sc-AFM scan settings are demonstrated here, showing the tradeoff between dwell (averaging) time at each raster pixel location, overall image field of view (FOV), and the scanning throughput. Regardless of the scan type, the nanoposts are fully resolved by the sc-AFM.

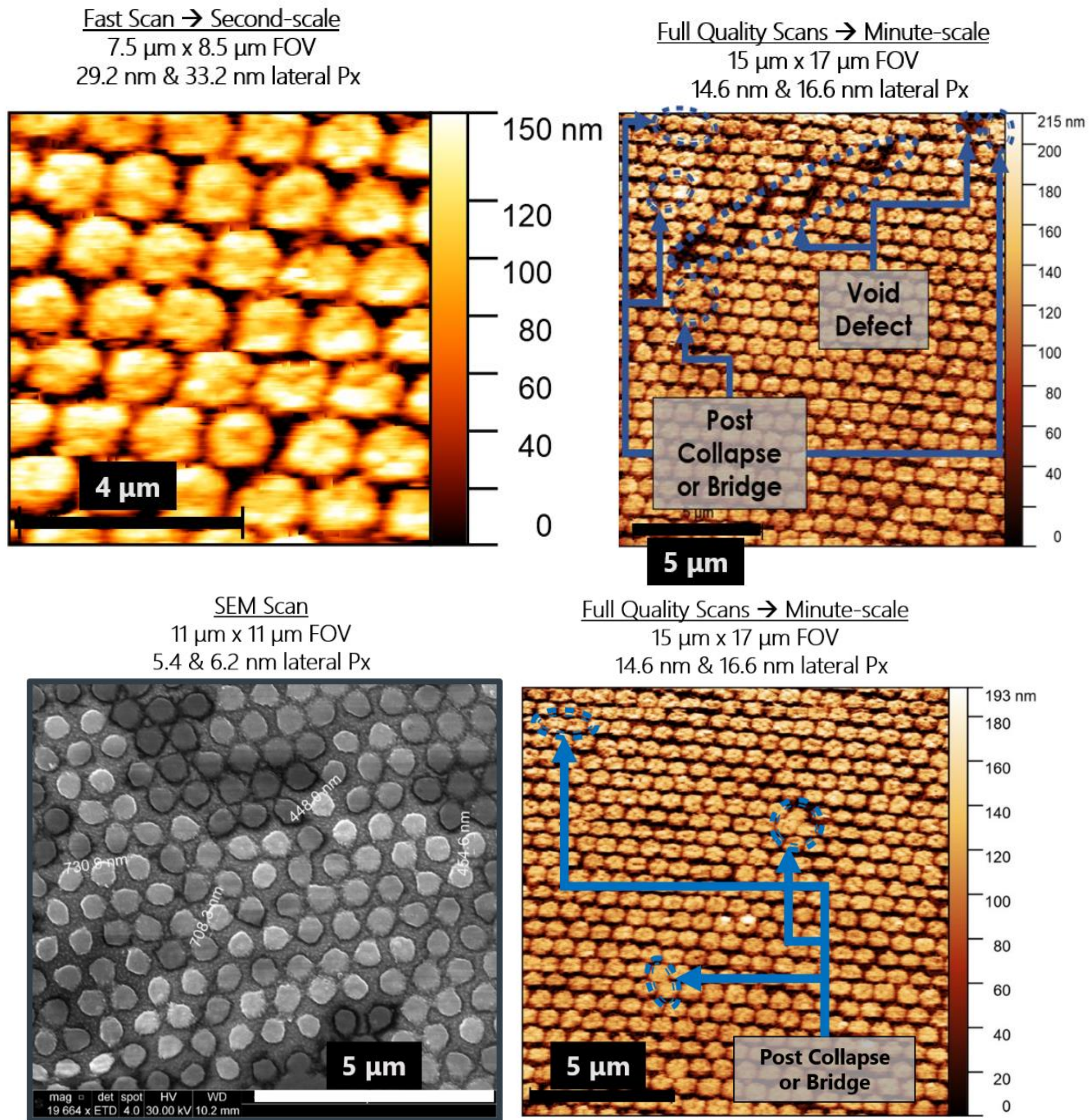

Figure 3.15: sc-AFM scans of gold nanoposts on a polycarbonate web

Finally, to test another sample which exemplifies the type of features which may be expected in R2R fabrication, an interference lithography patterned structure manufactured at UT's NASCENT center [172] . As is illustrated in Figure 3.15, the sc-AFM measured surface

topography and nano-hole arrays appear qualitatively similar to measurements taken with a calibrated table-top SEM tool in roughly the same location on the same sample and void defects are readily apparent.

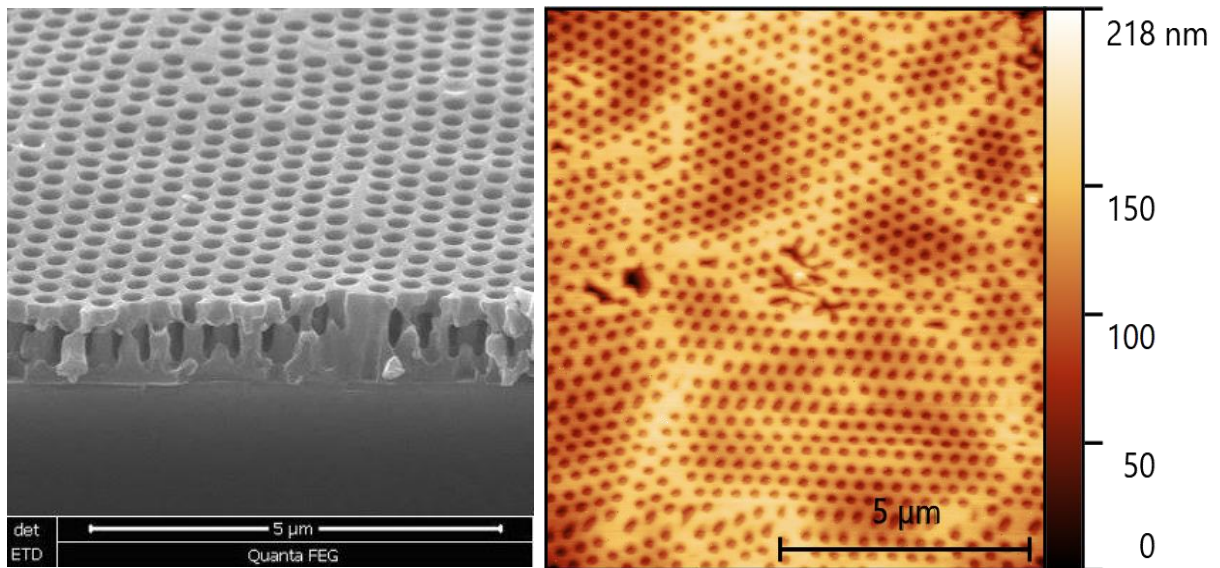

Figure 3.16: SEM micrograph (left) and sc-AFM result of R2R-capable interference lithography Nanopattern

CHAPTER 4 - IMPROVED R2R NANOMETROLOGY TOOL DESIGN

The refinement of the proof of concept prototype focuses on extending the demonstrated step-&-scan measurement operation of the prototype tool towards a future operational mode where the web to be measured does not need to be halted for sc-AFM sampling to occur. This process is outlined in Figure 4.1 where the area of performance improvement focus is highlighted. In order to accomplish this, the open loop nanopositioning system demonstrated must be improved to achieve high bandwidth, precise web velocity tracking in addition to the previous nanoposititoner functions which must be accomplished. Further, the web handling subsystem must be upgraded to minimize noise and vibration in the web while also greatly increasing the precision with which web position, velocity, and tension may be measured and regulated.

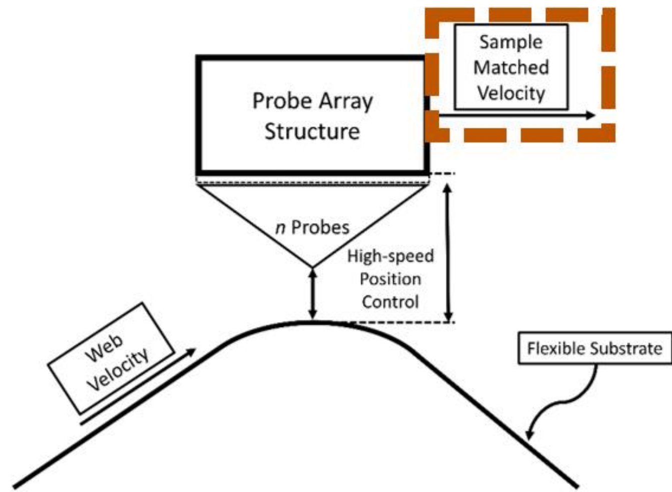

Figure 4.1: Schematic outline of quasicontinuous scanning framework

4.1 IMPROVED WEB HANDLING AND TENSION CONTROL

Upgrades for the web handling sub-system focus on achieving semicontinuous sc-AFM scanning. Along this vein, the web handling subsystem must be improved to minimize noise and vibration added by the motion components of the system, improve certainty in the measurement of web position, and improve control of web velocity and tension.

4.1.1 Improved Unwind/Rewind Spindle Design and Web Sensing

To minimize the effect of random errors linear velocity and tension commands, super precision class cartridge bearings (SKF BEAM 025075-RS) were chosen to replace the low cost, self-aligning roller bearings used in the preliminary prototype tool as shown in Figure 4.2. A cartridge bearing was selected as the mechanical fabrication machine tools, specifically precision grinding tools, which were readily accessible for the fabrication of a bearing housing would not be able to meet the dimensional tolerance specification typically required for super precision class roller bearings. Further, by selecting a heavily preloaded – 1.92 kN – back-to-back bearing architecture, stiffness to both applied moments and tensioning force is high –200 Nm/mrad and 790 N/μm respectively. Unlike typical super precision bearings, the only requirement for the chosen cartridge bearing is the flatness of the mounting plate. In this

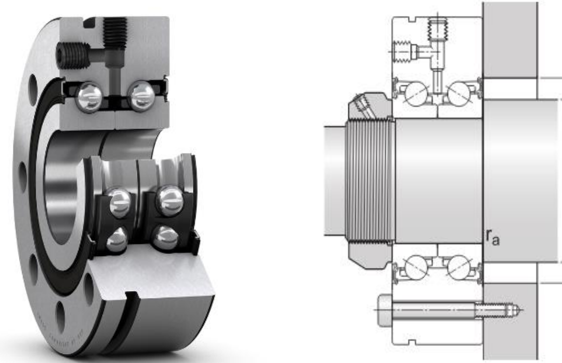

Figure 4.2: Super precision class back-to-back angular contact ball bearing cartridge

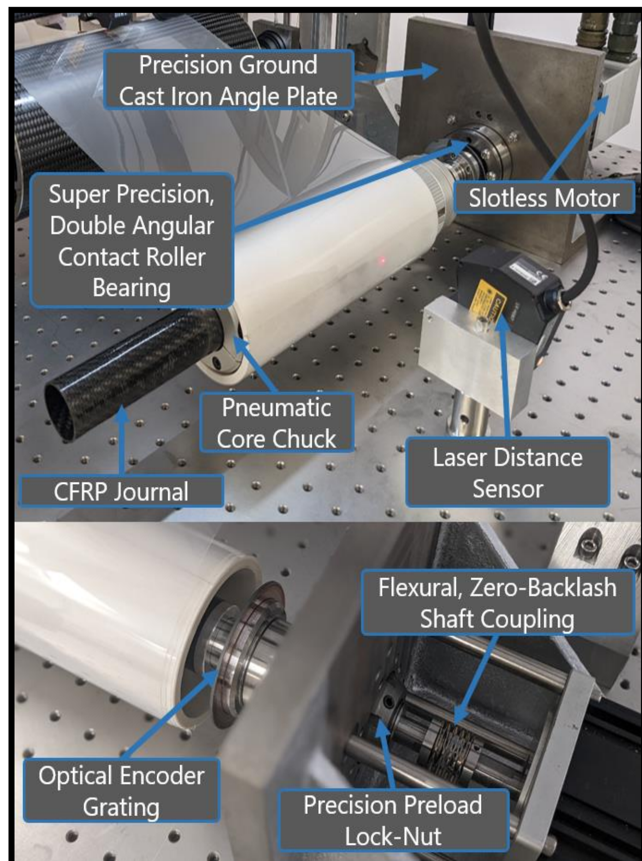

Figure 4.3: Upgraded rewind stand with major components labeled

case, cast iron precision ground angle plates with flatness of less than 0.0005” were chosen for both their ease of modification in addition to the perpendicularity to aid in alignment between the unwind and rewind stands bolted to the optical table breadboard surface.

Further, instead of relying on initial roll diameters and turn counting to convert from angular velocity and torque to linear web velocity and web tension, high-speed, precision laser triangulation sensors with 100 nm repeatability (Keyence LK-H087) are added to sense roller diameter change from an initially measured value on startup. Moreover, for the rewind stand which controls web velocity, a 30,000 period per revolution sin-cos optical angular encoder (Heidenhain ERP 1080 - 30000) Additional improvements include the replacement of the inexpensive, brushless DC stepper motor with precision, high-torque slotless, brushless, DC motors directly

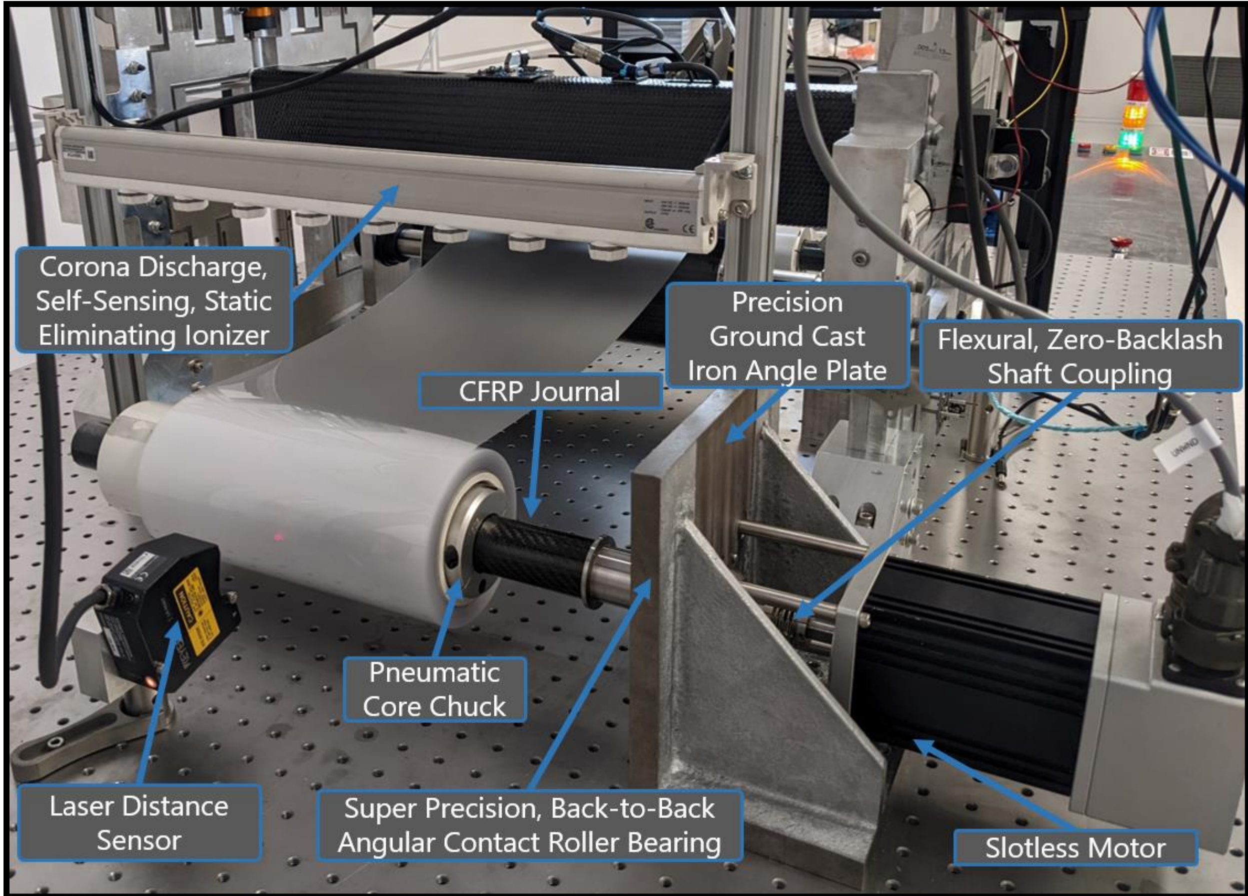

Figure 4.4: Upgraded unwind stand with major components labelled

coupled to the unwind/rewind chuck journals with a zero-backlash, stainless steel flexural shaft coupling to account for any shaft misalignments as depicted in Figure 4.3.

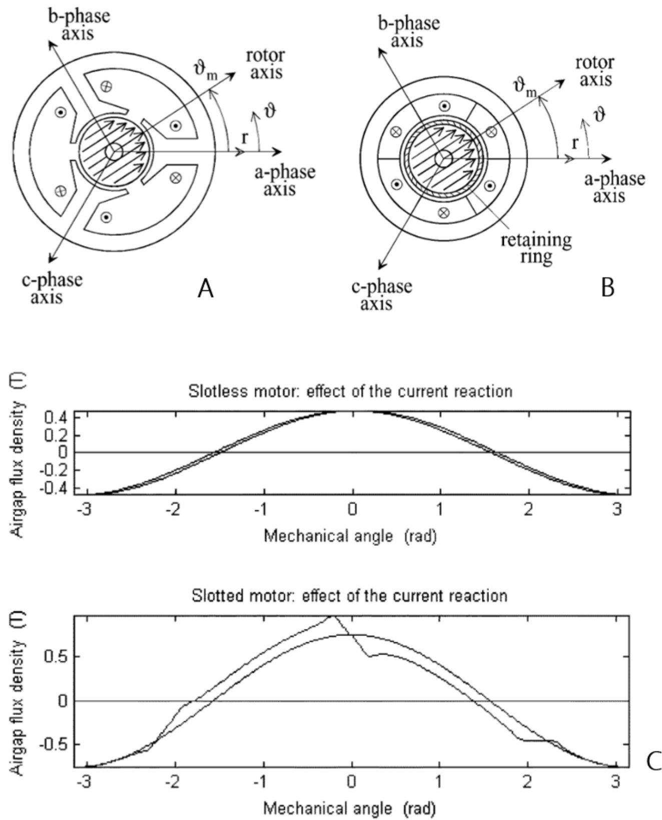

Figure 4.5: Schematic diagram of a typical brushless DC motor (A), a slotless DC motor (B) and the difference in torque ripple under load between the two motor confirgurations (C)

To take full advantage of the benefits of the new super-precision roller bearing unwind and rewind spindles, the rotary actuators and sensors coupled to the spindles must also be upgraded. To minimize noise in velocity control, a switch to "slotless", or ironless, DC motors was made. In a slotless motors rather than winding coils about iron teeth as shown in Figure 4.5A, a method that saves on manufacturing costs and achieves high torque density, slotless motor coils are either potted in a thermoset such as epoxy or wound about nonmagnetic cores as can been seen in Figure 4.5B [173]–[175]. While doing so increases costs and lowers power density, it all but eliminates the torque ripple due to the flux density channeled due to the ferritic teeth of a traditional brushless dc motor, as is depicted in Figure 4.5C.

Lastly, to eliminate any surface charging effects which might impart a force on the sc-AFM cantilever and thus skew the measured topography from the ground-truth of the sample surface due to interleave films and the unwinding of the roll of material, a cleanroom compatible, self

sensing static eliminator (Keyence SJ-H060A) based on the corona discharge effect from sharp tungesten tips is installed immediately after the unwind stand, as shown in Figure 4.4.

4.1.2 Improved Metrology Idler Roller

To reduce any noise inducing slip between the moving web and the idler roller on which sc-AFM scans are taken, a new light weight and high stiffness idler roller with minimized angular moment of inertia was fabricated. This roller consists of a 6 in diameter CRFP drum with billet stainless steel hubs bonded to each end. This has the secondary advantage of reducing the coefficient of thermal expansion compared to the previous stainless steel construction. Attached to these hubs are bearing journals for the same combination of radial air bushing and thrust air bearing used in the initial prototype, albeit with improved billet stainless steel bearing blocks for `increased stiffness and lowered coefficient of thermal expansion. The air bushing is mounted in the housing through a tight fitting series of fluorocarbon O-rings such that any misalignment due to optical table flatness or angular misalignment is taken up by the compliance of the O-rings. The thrust air bearing is prese fit into its' respective housing. This improved sub-system is outline in Figure 4.6 with the major components labelled.

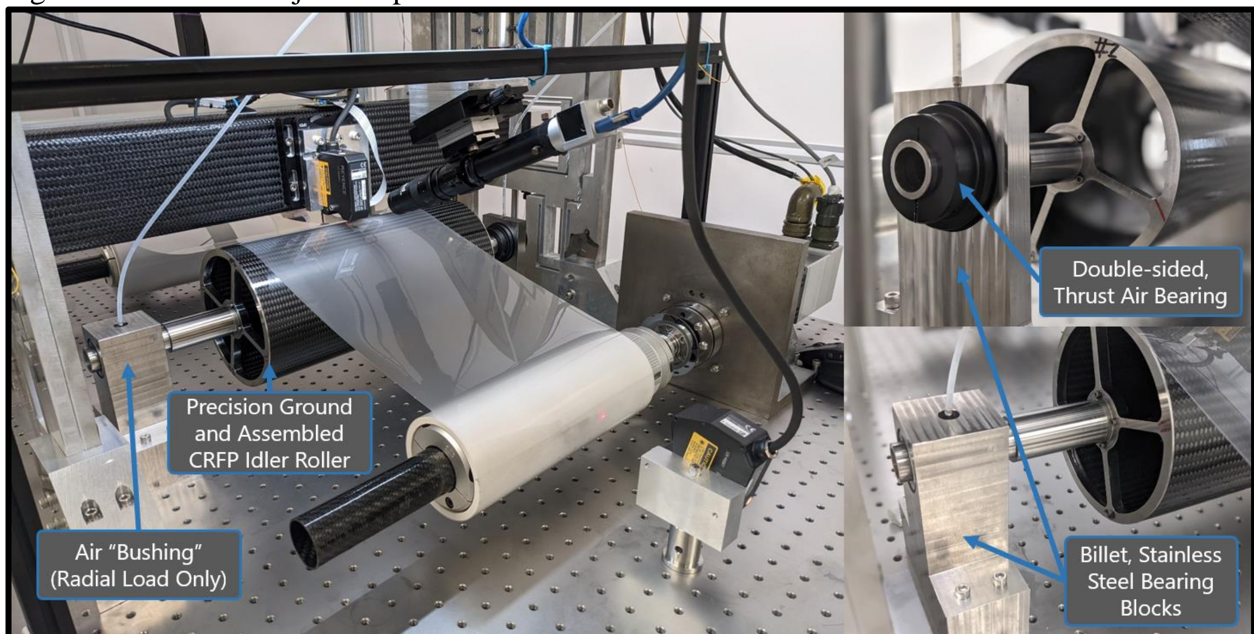

Figure 4.6: Upgraded air-bearing supported metrology idler roller

4.2 IMPROVED NANOPOSITIONING SUB-SYSTEM

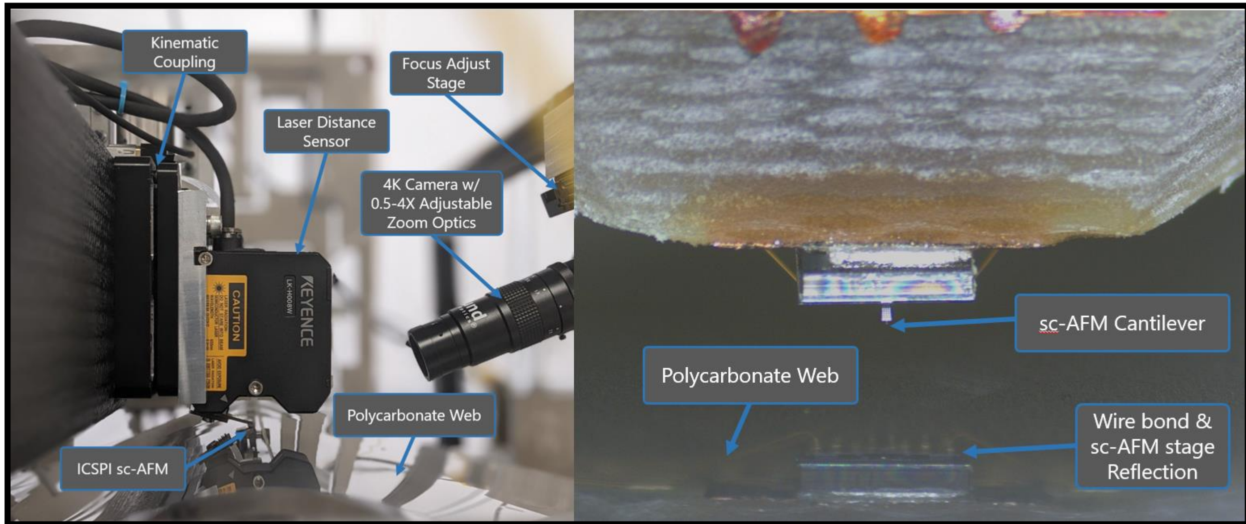

Figure 4.7: Side-view of the metrology module in the upgraded prototype (left) and view from the tool observattion camera (right)

In order to enable the high speed tracking of the top surface of the sample web, a 5 nm repeatability laser triangulation distance sensor (Keyence LK-H008W) is added next to the sc-AFM probe such that active feedback control can be implemented to lock on to a specific tip-sample separation during scans and compensate for roller runout, X-axis position above the roller metrology roller, and web thickness nonuniformities. As this design is only intended for use with a single sc-AFM, the fine approach DPFM bearing and linear voice coil motor were removed to minimize compliance in the metrology from of the sc-AFM. A process monitoring camera with 4K resolution and 0.5X to 4X adjustable zoom optics (Edmund Optics VZM 400i) is also added.

4.2.1 Structural Upgrades

To maximize the specific stiffness of the gantry structure (i.e. the stiffness normalized to mass), the previous prototypes aluminum extrusion was replaced with a CRFP rectangular structure with bonded and threaded aluminum end-attachments. The CRFP in this case is primarily made with unidirectional carbon fibers to maximize the bending stiffness of the gantry arm. A locking, kinematic coupling (Newport BKL-4) is then attached to a machined flat on the CRFP gantry arm by means of bonded, threaded inserts to facilitate fast and easy sc-AFM tip exchange without significant realignment of the system.

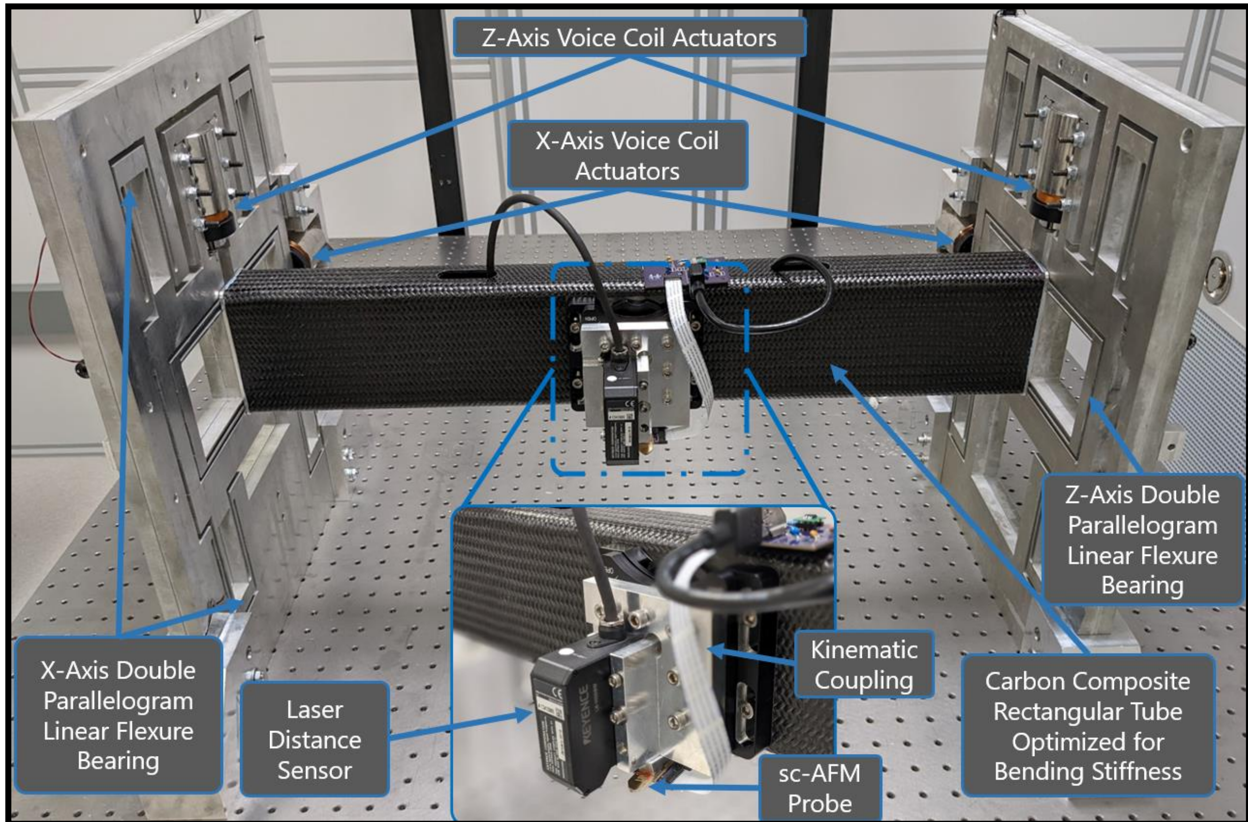

Figure 4.8: Structural upgrades to the sc-AFM positioning sub-system

4.2.2 Sensing upgrades

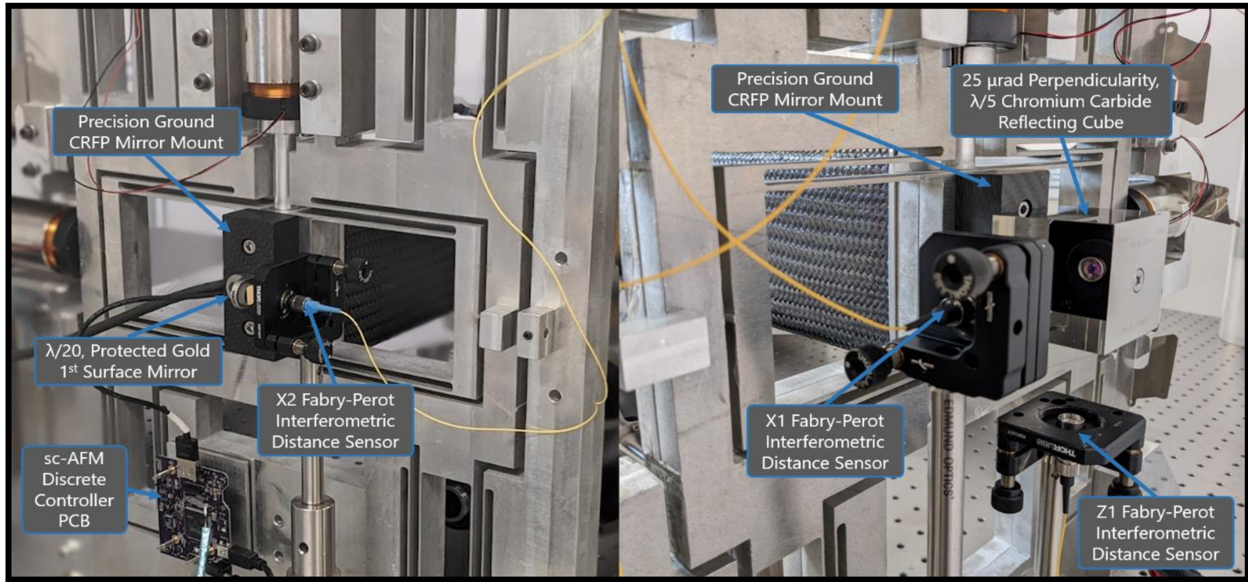

Figure 4.10: Sensor heads and mirror targets for the interferometer distance sensors

While the initial prototype tool utilized capacitance guage based sensing measure the position of each axis on each side of the sc-AFM gantry, in order to fully take advantage of the range of the flexure mechanisms, a longer range sensing solution was required. Whereas the capacitance gauges could only reliably measure 250 μm of range, a new system of Fabry-Perot interferometric distance sensors (Attocube FPS3010) is implemented with mm-scale range well beyond the maximum reach of either the Z- or X-axis flexure stages and a maximum stage velocity of 2 m/s. Further, the bandwidth of the interferometer sensing system exceeds 100 kHz when interfacing with the FPGA control system through a custom high-speed digital communication protocol (Appendix A10) compared to the ~1 kHz bandwidth of the previous sensors used. As only

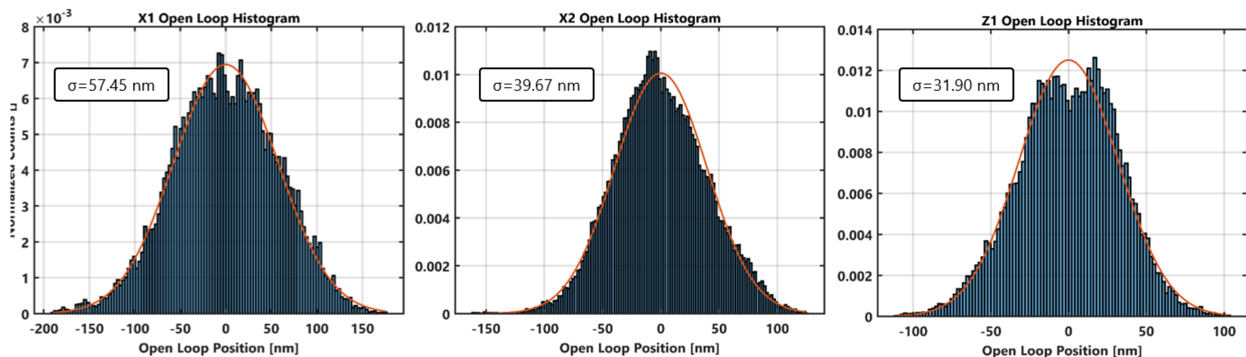

Figure 4.9: Open loop noise levels in all three measured axis with the improved interferometric distance sensors

three channels are available, both X-axis flexure stage positions are measured and the Z-axis on only one side of the system, as shown in Figure 4.9. For the flexure stage with two channels, a perpendicular, chromium carbide reflecting cube (Starrett-Webber, 2”, 5 arc-sec) is used. On the single-measurement side, a small 0.5” diameter protected gold first surface mirror is employed. Open loop noise floors from these new high-bandwidth sensors, and in the new tool installation location of the NASCENT cleanroom facility are shown below in Figure 4.10. While these noise floors are greater than the initially reported, single-sided data, this is likely due to the reduced first resonant modes caused by the increase in moving mass when both flexure monolith plates are connected via the sc-AFM gantry.

4.2.3 Power and Control Electronics Upgrades

To make best use of the new sc-AFM and web positioning systems, an upgraded cRIO real-time control system with significantly increased FPGA size and resources (cRIO-9038) in addition to low noise, 5 kHz bandwidth current transconductance amplifiers to drive both the linear voice coil motors and the rotary slotless BLDC motors (Trust Automation TA310 & TA330). In this case the amplifier for the X-axis voice coil motors is sized for maximum turnaround throughput

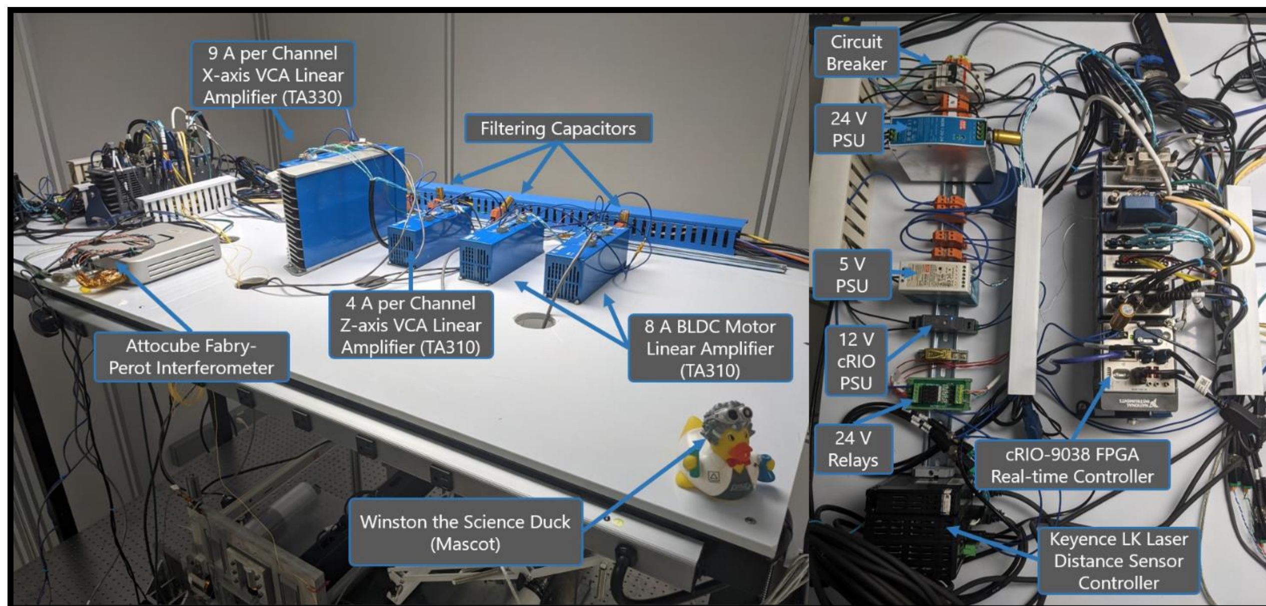

Figure 4.11: Upgraded system power amplifiers and control electronics

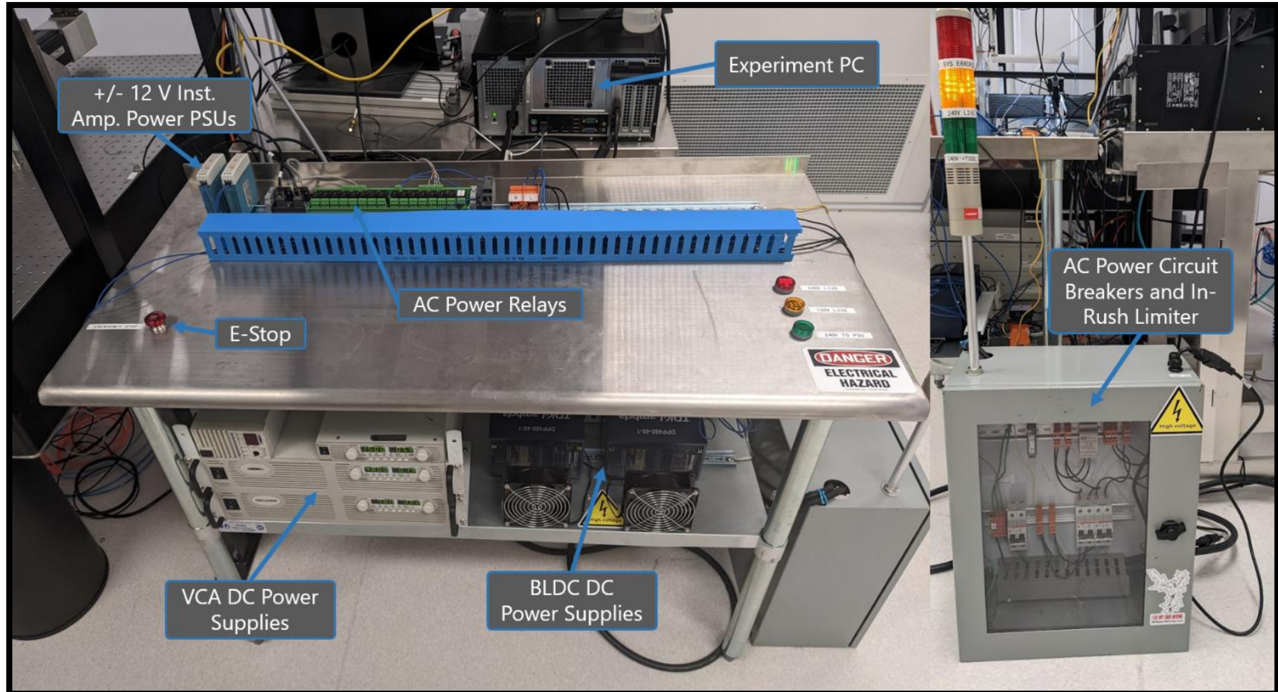

Figure 4.12: Upgraded DC power supplies, control relays, and protective circuitry

during quasicontinuous scanning operations of ~5 g acceleration (9 A per coil). To support these upgraded power electronics, high reliability, programmable, low-noise switching DC power supplies (TDK-Lambda GenSys and DPP480-48) are implemented to supply then linear transconductance amplifiers. Lastly, high voltage supply is routed through circuit protection and controlled by a series of relays actuated by the cRIO controller. A diagram of the various control loops may be found in Appendix A.

CHAPTER 5 - SYNCHRONOUS CONTROL SYSTEM DEVELOPMENT

5.1 Advanced Motion Control for Moving Scans

The first step in implementing a new closed loop control system is successful modelling of the multiple-input-multiple-output (MIMO) dynamic "plant" made up of the two DPFM monoliths connected by the sc-AFM gantry. While design stiffness, geometry, mass, and damping could be used to construct a linear time invariant model of the system according to the layout shown in Figure 5.1, due to the method of flexure fabrication – abrasive water jet cutting – there is a non-insignificant difference between as-designed and as-fabricated values. To compensate for this effect, an iterative numerical method was used to estimate the 4th order MIMO transfer function matrix given the expected number of poles and zeros from the model shown in Figure 5.1 and experimental input-output data [176], [177]. Again, a 1 kHz white noise input was applied to each side of the gantry positioner in series, and the time synchronized output data used to drive the fitness function of this grey box transfer function estimation. Results of this estimation in comparison to the frequency response function of the open loop system, again estimated with

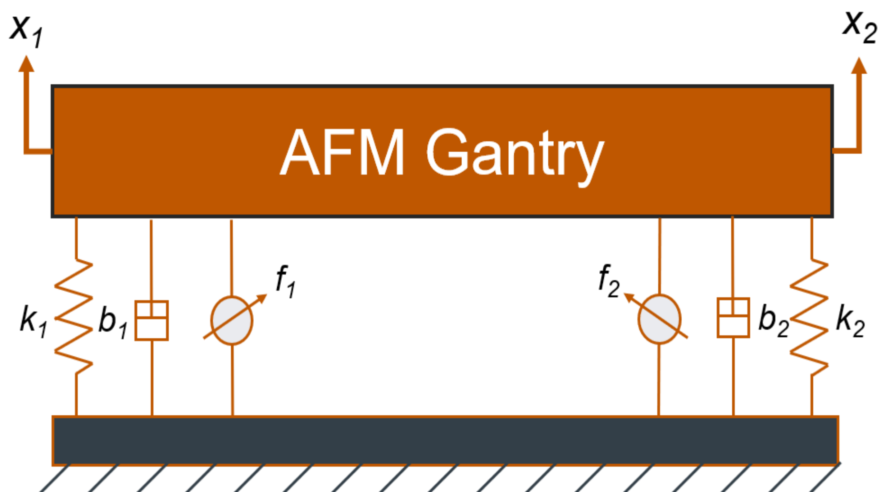

Figure 5.1: Schematic of single-axis MIMO model of sc-AFM gantry positioning system

Welch's averaged periodogram method, are shown in Figure 5.2. Some of the difficulties involved with designing a control system for this plant include the closely spaced, yet disparate, 1st resonant modes of the individual AWJC flexure monoliths caused by the variation of kerf, and thus stiffness, with each cut. Further, the stiffness of the gantry structure supporting the sc-AFM means that the cross-coupling between the different flexure monolith sides is rather strong in comparison to the magnitude of the on-diagonal bode response. These factors play a role in increasing open loop noise floor for the interconnected system due to self-resonance from side-to-side and increasing the difficulty in improving system bandwidth beyond open loop levels.

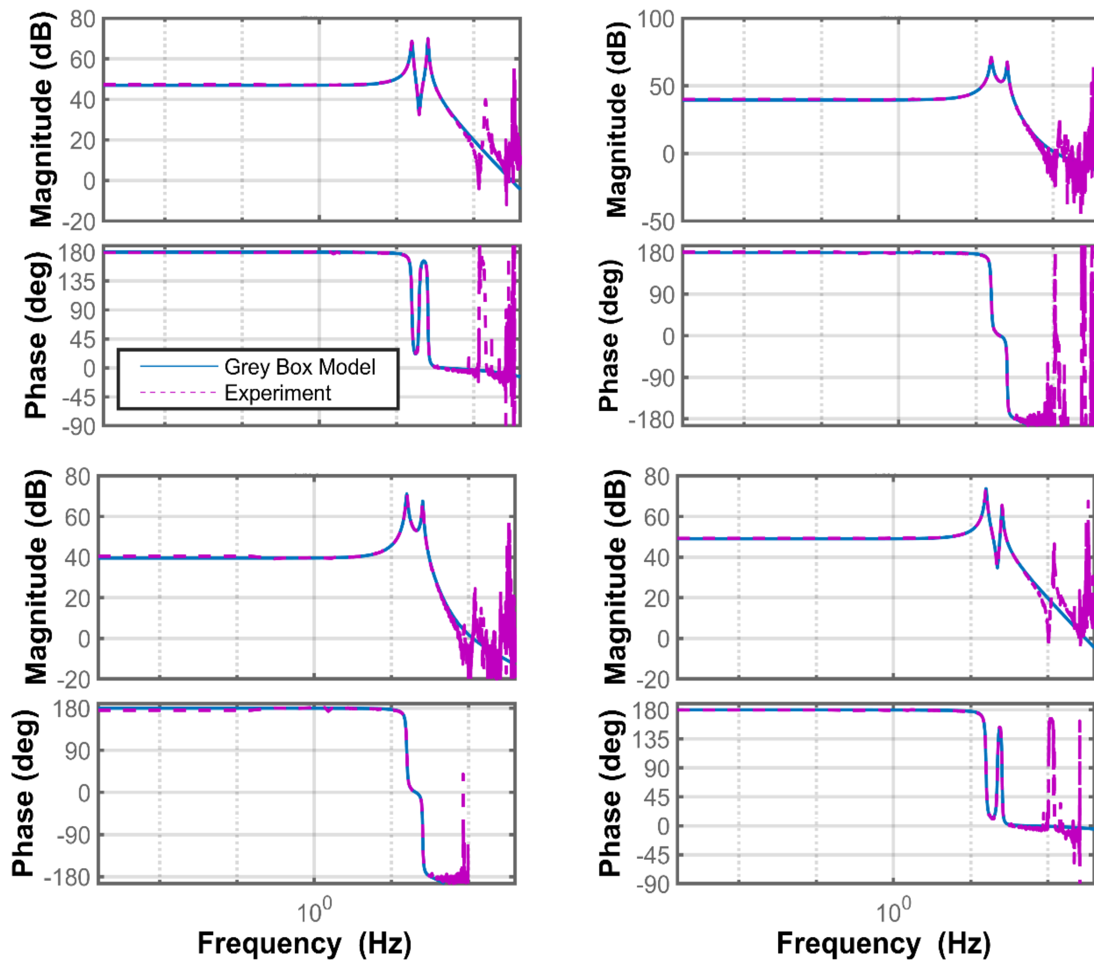

Figure 5.2: Open loop frequency response function and grey-box model for MIMO system of X-axis sc-AFM positioner

5.1.1 H-infinity Control for Nanopositioning

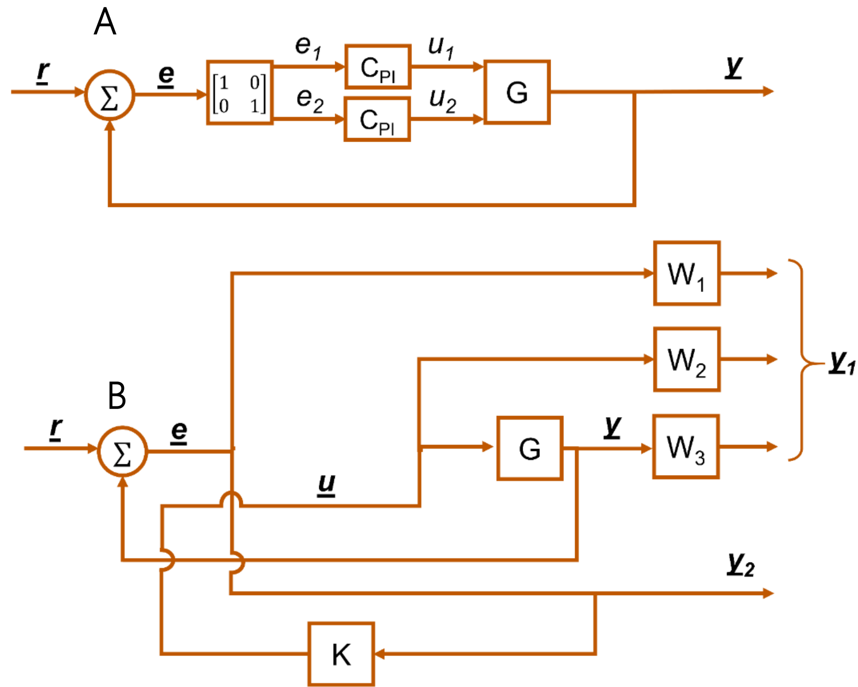

Figure 5.3: Control system block diagram for (a) decoupled MIMO PI control and (B) H-Infinity control

With an experimental model for the open loop system in place, control design can begin in earnest. Two main approaches were originally considered: (1) a classic implementation of MIMO, decoupled proportional-integral (PI) control and (2) H-Infinity based closed loop controller synthesis. The block diagram control structures for both approaches are shown in Figure 5.3A and 5.3B respectively, where G is the open loop plant model, C_{PI} the transfer function for each decoupled PI controller, K the stabilizing synthesized controller, and W_1, W_2, W_3 the weighting functions used in the H-Infinity generation. In the case of Figure 5.3B, these weighting functions, typically taken to be first or second order filter transfer functions, are most commonly determined through prior experience and general, empirical "rules-of-thumb" [178]. From the first examples of applied H-Infinity control to control of unstable airplane platforms for the military, the most common explanation for how weighting functions are chosen is simply "by inspection". However,

while the H-Infinity framework will always synthesize a stabilizing controller which satisfies the norm shown in Eq. 5.4, there is no guarantee that the weights applied to the sensitivity function (Eq. 5.1), complementary sensitivity function (Eq. 5.2), and closed loop transfer function (Eq. 5.3) will produce an *optimal* controller for a given open loop system and specific system performance goal or performance under specific setpoints and operating conditions. Moreover, without extensive controls design experience working with the H-Infinity method, it can be difficult to balance the tradeoffs for reference following, robustness to modeling errors and external disturbances, and controller effort and saturation. To aid in resolving this issue and ensuring an optimal controller, a new method must be developed.

$$\boldsymbol{S} = (1 + GK)^{-1} \tag{5.1}$$

$$\boldsymbol{R} = K(1 + GK)^{-1} \tag{5.2}$$

$$\boldsymbol{T} = GK(1 + GK)^{-1} \tag{5.3}$$

$$\left\| \begin{bmatrix} W_1 S \\ W_2 R \\ W_3 T \end{bmatrix} \right\|_{\infty} \leq \mathbf{1} \tag{5.4}$$

5.1.2 Heuristically Optimized MIMO H-Infinity

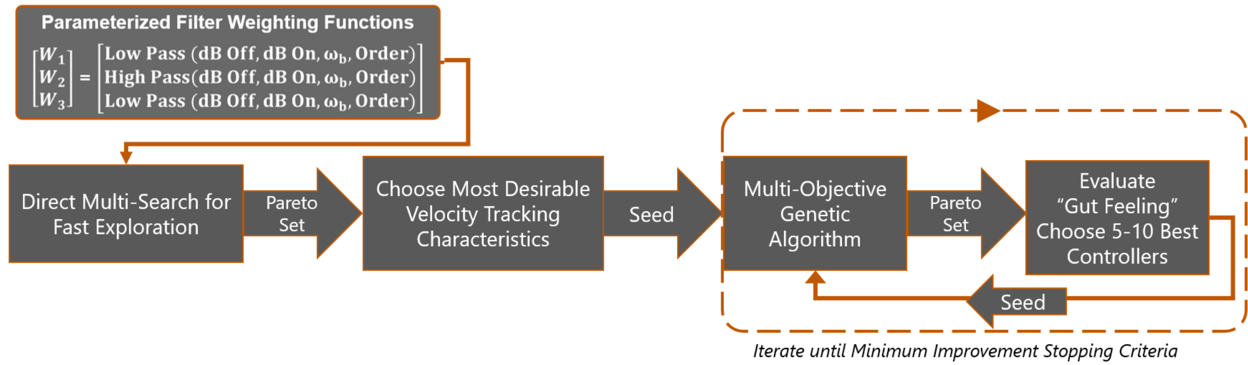

Figure 5.4: Flow-chart for the proposed "H-Optometry" algorithm

In lieu of picking weighting functions by simple trial and error, a multi-objective heuristic optimization approach is taken instead. Fitness of closed loop controller performance is measured by three figures of merit driven by the intended application of the control system: high-speed tracking of constant velocity web movements. Thusly, the performance objectives for minimization were chosen to be: (1) the standard deviation of velocity error and (2) the maximum velocity error. Further, to lower the number of infeasible controllers generated with unrealistically high gains and controller response effort, the maximum control force applied to the system during constant velocity commands is also minimized. The representation of these performance goals for minimization is shown in Figure 5.5.

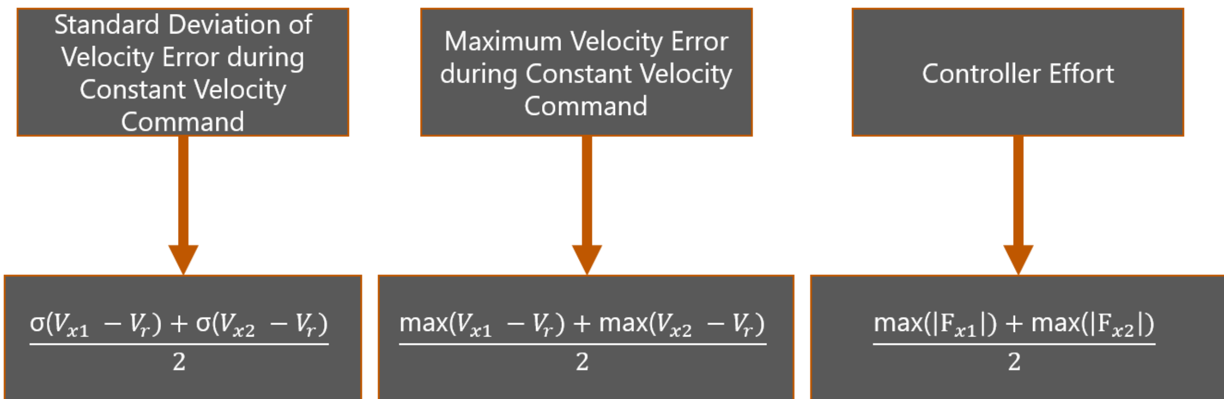

Figure 5.5: Optimization goals for the applied H-Optometry process

These are measured for each candidate controller through a linear time invariant simulation of 500 ms of system operation at a maximum sc-AFM sampling speed of 5 Hz and full flexure motion range positional reset moves after each line scan. The optimization is formatted such that each of the three H-Infinity weighting functions are generated from 4 parameters each, high and low magnitude, corner frequency, and filter order.

These 12 inputs are first varied by a direct multi-search algorithm to quickly and efficiently explore the easily reached portions of the pareto response space. However, instead of choosing from this space, a human operator next selects a set of between 5 and 10 candidate controllers based upon a quick "gut-judgement" visual inspection of reference tracking and frequency response performance. This preferred set is then, in turn, used as a seed to a secondary multi-objective genetic algorithm (NSGA-II), iterating with new pareto sets and new operator-selected seed sets until a minimum improvement stopping condition is reached [179]. This process, a modified version of the optometrist's algorithm, allows for heuristic selection of candidate controller designs which perform well in a manner not easily or fully captured by the chosen figures of merit [180]. A flow chart outline of this process is shown in Figure 5.4. In this case the initial direct multi search algorithm is quick and efficient at exploring a large area of the optimal set of solutions, while the more traditional genetic algorithm, when seeded through the optometrist's process, is more adept at exploring the extremes of the pareto optimal solution space. Through this process, and without an extensive and nuanced background in H-Infinity control design, robust stabilizing controllers may be algorithmically synthesized to best fit the performance scenario for a specific application. The initial and final pareto spaces from this optimization, with optometrist chosen pareto solutions, are show in Figure 5.6.

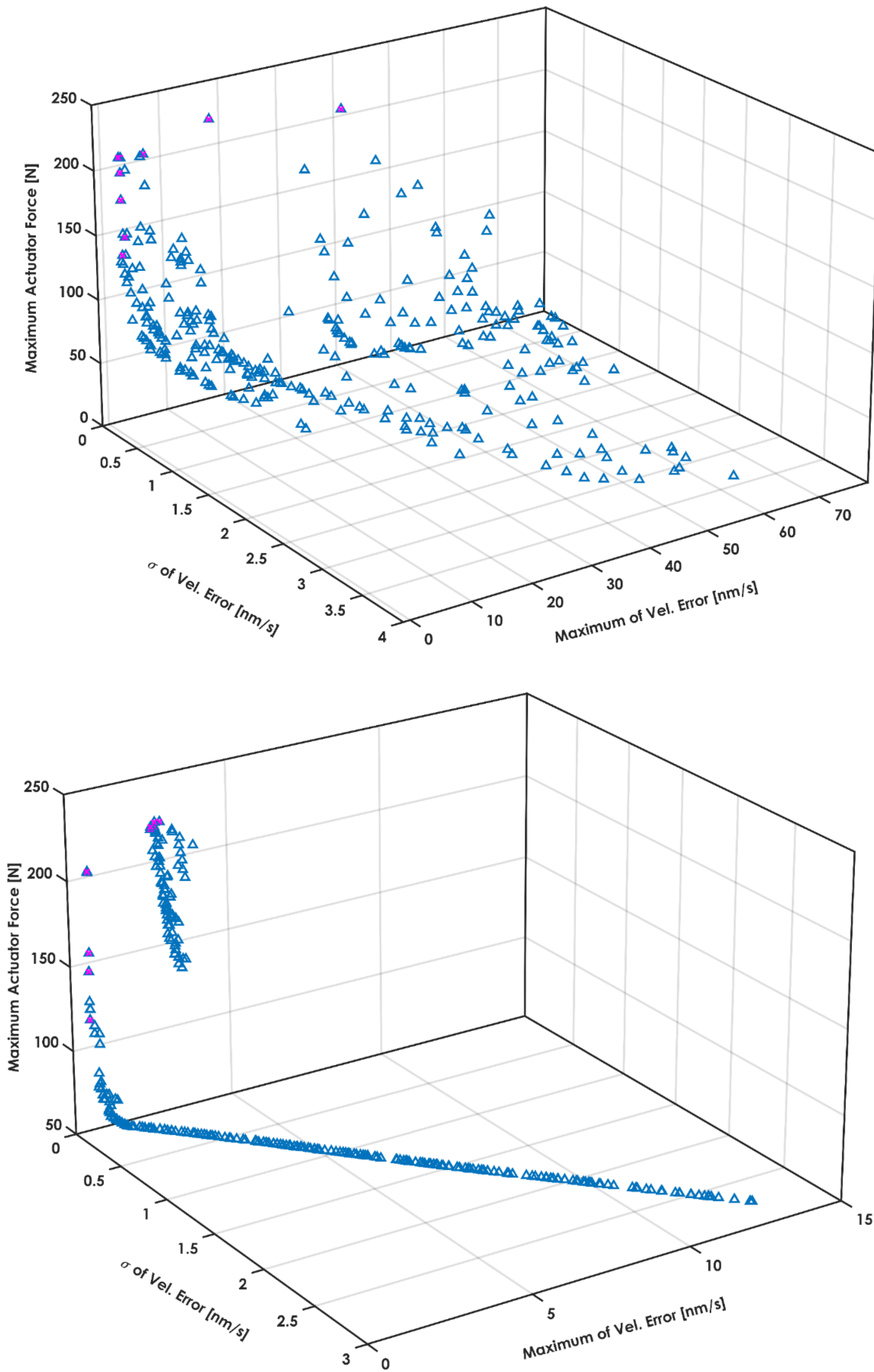

Figure 5.6: Pareto optimal solution spaces after the initial *Direct Multi-Search* algorithm (top) and the final interaction of the NSGA-II algorithm (bottom) with the candidate controllers chosen by the operator filled with purple

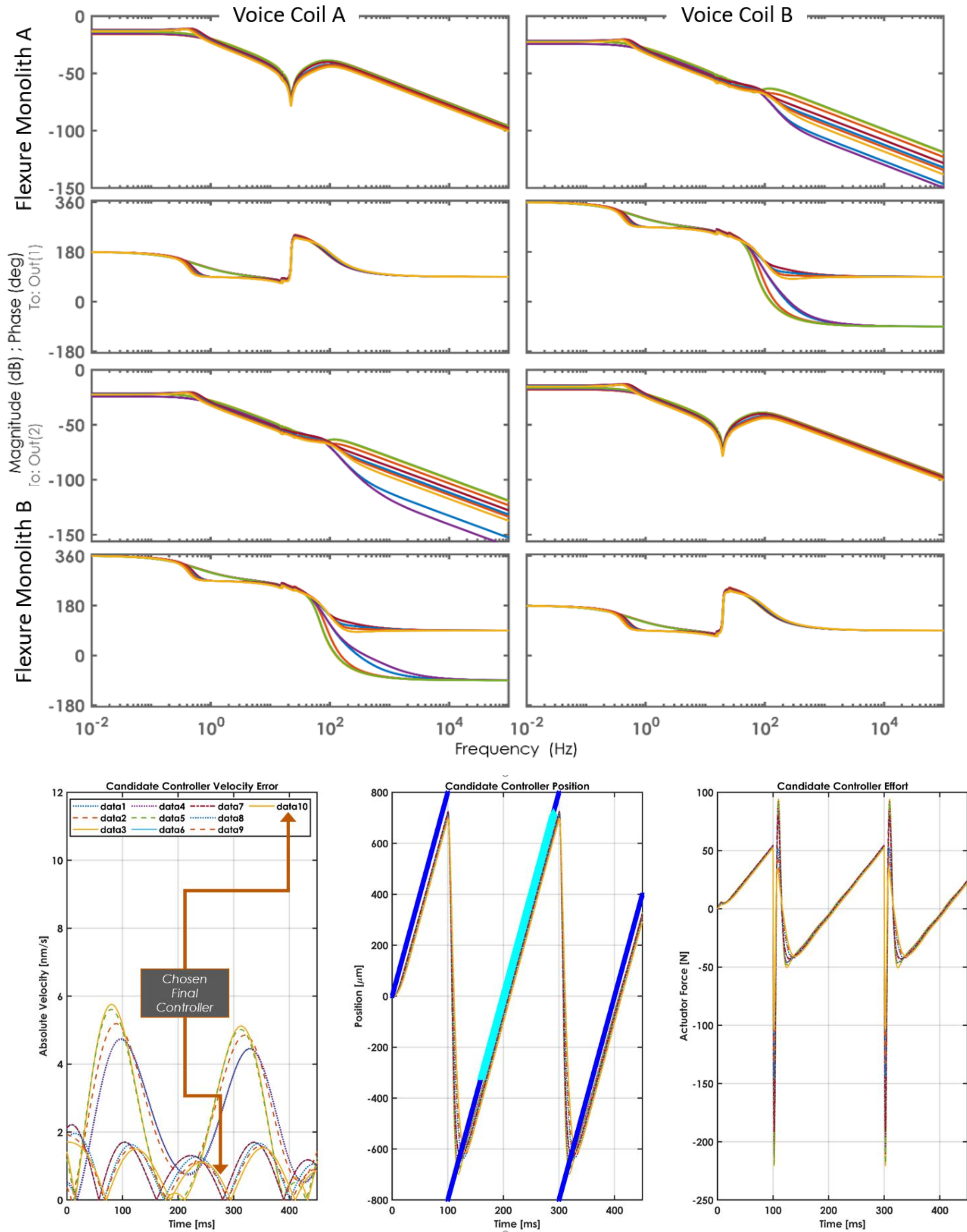

Figure 5.7: Bode response (top) and LTI simulated system performance of final iteration of H-Optometry generated controller candidates (bottom)

A selection of the 10 most promising controller candidates from the final iteration of the algorithm is shown in Figure 5.7. The frequency response of each controller, K is shown in Figure 5.7 (top) where each color corresponds to a disparate transfer function. Figure 5.7 (bottom) shows plots for each figure of merit used in the optimization with the zone where each metric is calculated, highlighted in turquoise, and the reference constant velocity signal shown in navy.

In comparison to both the open loop system and industry standard PI control, it is clear from the frequency response shown in Figure 5.8 that the optometrist optimized H-infinity synthesis, or H-Optometry, significantly outperforms common alternatives.

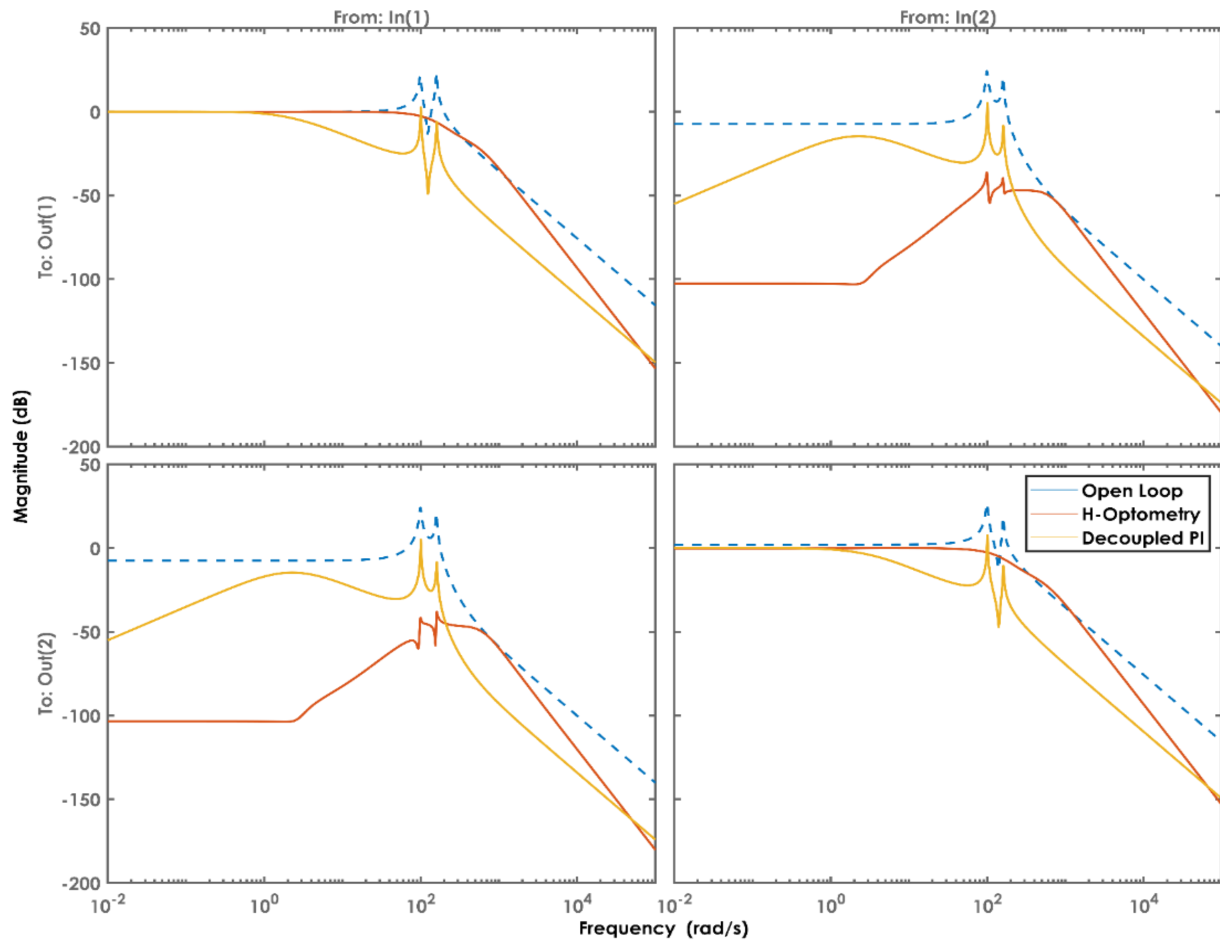

Figure 5.8: Magnitude of the frequency response of the final h-optometry closed loop system in comparison to decoupled pi control and the open loop system

5.2 ROTARY MOTOR FIELD-ORIENTED-CONTROL

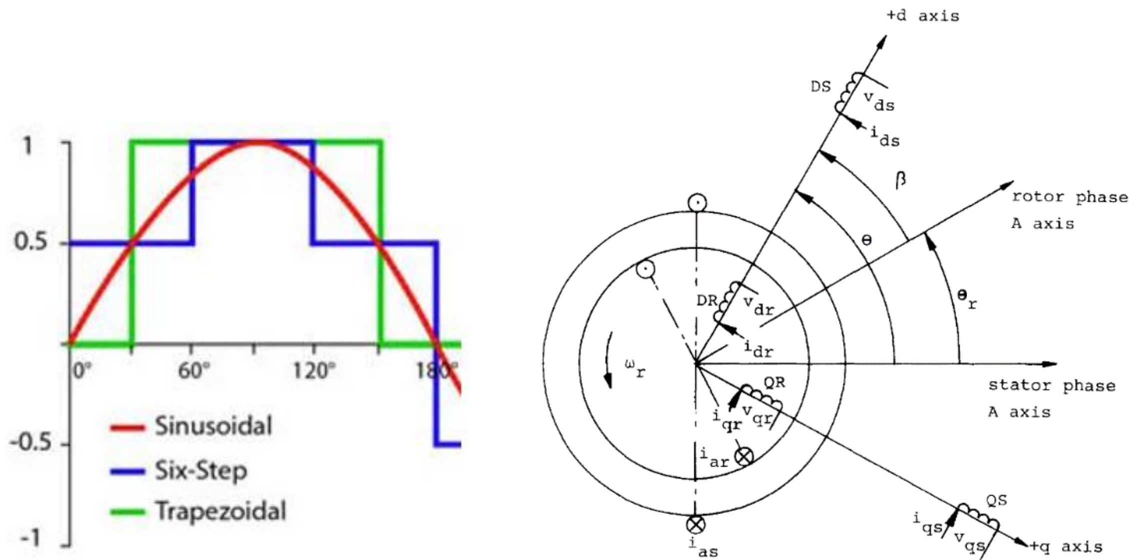

Figure 5.9: Traditional BLDC motor commutation (left) and the different coordinate reference frames of Field Oriented Control (right)

In addition to the upgraded slotless rotary motors, the control algorithm used to actuate them must also be updated from the pulse-train operation of the initial DC stepper motor configuration in order to achieve the smoothest web velocity, especially at lower speeds. Given this focus on the precision and noise of velocity and torque control, a field oriented control (FOC) or vector control algorithm was chosen [181], [182]. This control schema, unlike simple sinusoidal or trapezoidal electronic commutation, FOC increases system bandwidth, improves control precision, and allows for direct torque and speed control. A comparison of the traditional electrical commutation waveforms and the reference frames of FOC vector control are shown in Figure 5.9. To accomplish this vector control, measured outputs must be converted from the rotating d-q rotor reference frame (Clarke transform) to the stationary α-β frame and from there to the 3-phase A-B-C motor lead reference frame (Park transformation) and back again for control inputs. These transformations must be implemented on the control FPGA in addition to the d-axis and q-axis PI controllers. A block diagram showing the coordinate transformations and control architecture is shown in Figure

Figure 5.10: Control block diagram for FOC algorithm applied to rotary motors using a linear amplifier

5.10. In addition to speed control of the unwind motor, torque control of the unwind stand will also be regulated by a parallel FOC algorithm implemented on FPGA, just without the *Optional* PI speed controller outlined in dashes in Figure 5.10.

5.3 HIGH SPEED FPGA CONTROLLER DEVELOPMENT

To guarantee proper coordination between linear velocity commands to the rewind stand and set points to the X- and Z-axis nanopositioning sub-systems, all control calculations and process variable acquisition, filtering, and processing must occur on FPGA. The difficulty herein is the limitation for fixed-point numerical representations to enable efficient operation with multiplication and especially division, which is one of, if not the most expensive arithmetic operation to employ on FPGA. Where possible any conversion constants required, for everything from mm to µm to 1/sqrt(3) or 1/π is implemented as a multiplication block with a hard coded constant value.

This is most challenging when it comes to the implementation of higher order controllers like those generated by H-Infinity synthesis. If implemented in the traditional manner, as in Eq. 5.1, the arithmetic errors due to the constraints of fixed-point math would quickly accumulate to the point of disfunction. To circumvent this critical issue and implement the types of controllers generated through the algorithm presented in this chapter, a cascade of second order sections (SOS) may be implemented. Because each individual node calculation is nominally only 2nd order, the accumulation of fixed-point errors is significantly reduced. To implement this, an algorithm converts from the numerator and denominator coefficients in Eq. 5.1 to the coefficients required for each cascaded SOS from 1 to *L* in Eq. 5.3 while minimizing error [183].

$$H(z) = \frac{B(z)}{A(z)} = \frac{b_1 + b_2 z^{-1} + \cdots + b_{n+1} z^{-n}}{a_1 + a_2 z^{-1} + \cdots + a_{m+1} z^{-m}} \tag{5.1}$$

$$H(z) = g \prod_{k=1}^{L} H_k(z) \tag{5.2}$$

$$H(z) = g \prod_{k=1}^{L} \frac{b_{0k} + b_{1k} z^{-1} + b_{2k} z^{-2}}{1 + a_{1k} z^{-1} + a_{2k} z^{-2}} \tag{5.3}$$

This same approach in a block diagram representation can be seen in Figure 5.11 where *L* is the desired order of the transfer function. Though resource constrained due to the plethora of other control and measurement tasks required to be coded directly on FPGA, such as laser linear velocity calculation, interferometer communication, and motor encoder measurement and

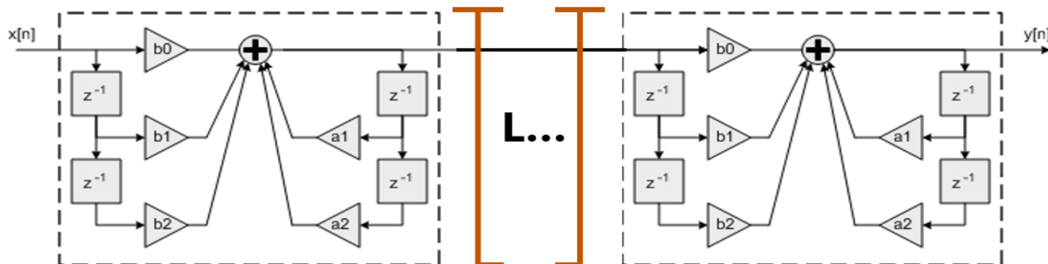

Figure 5.11: Cascaded second order section structure to efficiently represent higher order transfer functions

interpolation, up to 14th order transfer functions may be implemented at loop speeds exceeding 20 kHz.

CHAPTER 6 - CONCLUSIONS AND FUTURE WORK

6.1 Conclusions

By and large, the R2R tip-based metrology architecture presented in this work represents a new and efficacious approach to direct topography measurement on flexible webs with nanometer scale precision. This capability for non-destructive measurement, where previously samples had to be cut out from sections of a R2R web, represents a novel capacity to add to existing, largely optical based, measurement methods for process sampling in R2R nanofabrication. Through implementation of this demonstrated R2R AFM capability, hybrid metrology approaches which have been hugely successful in pushing the boundaries of state-of-the-art wafer based fabrication may now be implemented in R2R processing - enabling research and development efforts towards true HVM of sub-micron overlay error, multilayer fabricated flexible electronics.

Chapter 1 provided an overview of the current state of nanoscale metrology in R2R manufacturing and the novel, MEMS-based sc-AFM probe. Chapter 2 reviewed the status quo in advanced, multi-layer R2R fabrication technologies and current challenges in achieving sub-micron overlay error for advanced devices such as thin film transistors. Chapter 3 presented a proof-of-concept prototype tool which could sample topography data on flexible webs in a step-and-scan fashion with good agreement to traditional table-top AFM and SEM measurement tools. Chapter 4 discussed the upgrades made to the initial prototype tool to enable a new mode of scanning – quasicontinuous operation through a series of structural, sensing, control, and electronic improvements made to the prototype tool, shown in Figure 6.1. Lastly, Chapter 5 demonstrated a novel method for heuristically generating high performance, stabilizing closed loop controllers with the H-Infinity method without the typically requisite deep background in H-2 and H-Infinity norm based controller synthesis to improve closed-loop system performance.

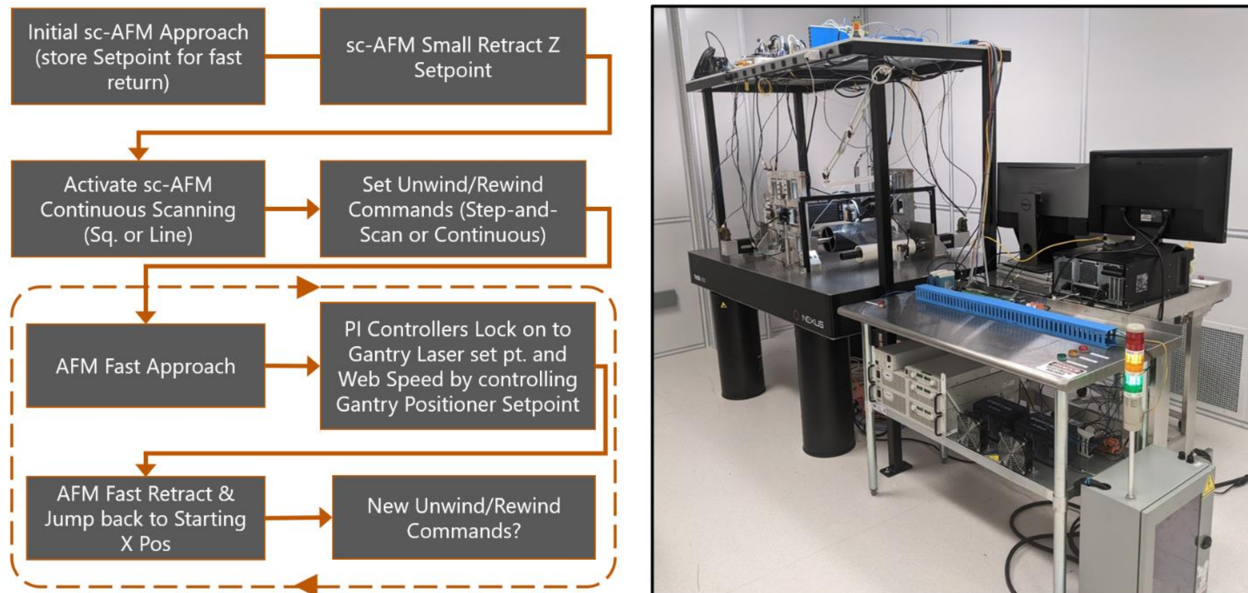

Figure 6.1: Upgraded system state-machine operation flow chart (left) and trimetric view of the system in the NASCENT cleanroom metrology bay

6.2 FUTURE WORK

6.2.1 Further System Improvements

While every effort was undertaken to ensure the upgraded system prototype was fabricated as precisely as possible, a final outside diameter grind of the Unwind/Rewind stand journals would greatly reduce any runout due to geometric error in the CFRP tubes that are bonded to the stainless steel bearing shafts. Unfortunately, the surface grinding tool in UT’s mechanical engineering machine shop does not have the range to perform this operation so it was not completed for this work.

Moreover, full implementation of the optimized H-Infinity controller would improve the dynamic performance of the improved system and aid in enabling quasicontinuous sampling without degradation of the sc-AFM’s measured tip data as outlined in the Line AFM mode of operation in Figure 6.4 (left).

6.2.2 Data Fusion

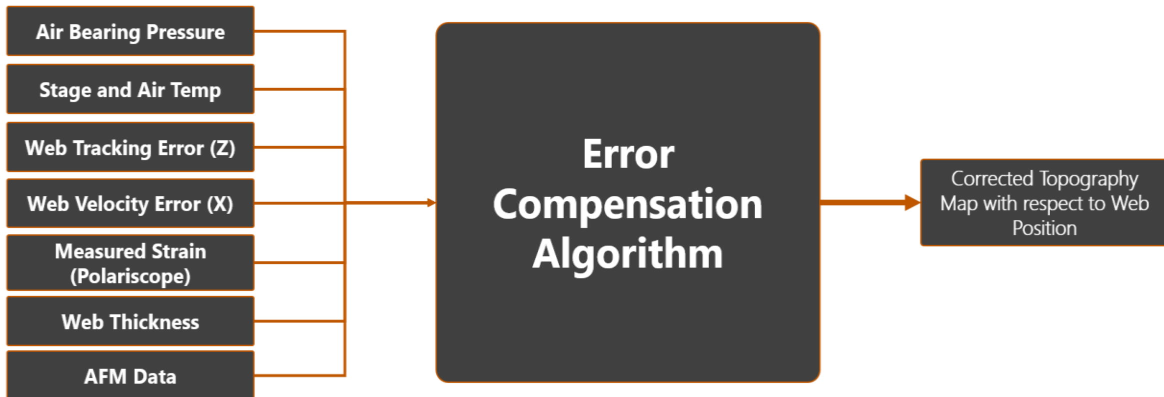

Figure 6.2: System instrumentation future error compensation schema

While instrumenting the upgraded prototype tool with a variety of sensors was a priority, a well-designed algorithm which take advantage of these sensing capabilities and which can continuously measure this plethora of information sources, as is shown in Figure 6.2, and correct for effects such as the thermal expansion and contraction of the aluminum flexure plates, thickness non-uniformity of a web under constant tension, measured web strain, and any system controller web following errors synchronized with tip measurement data. This would enable significant reductions in total measurement uncertainty and thus improved system performance.

6.2.3 True In-line Operation

Finally, the primary forward looking goal of this research was the enabling of future truly in-line measurement of nanoscale topography without negatively impacting the throughput of any new processes or fabrication tools under development. An example of a novel R2R fabrication tool with consideration for in-line metrology is shown in Figure 6.3. A combination of optical metrology and the proposed sc-AFM based in-line process control would provide maximum benefit for yield enhancement and eventual automated process control decision making which could leverage both the high-speed and throughput optical measurements and the quasicontinuous direct tip-based sampling as shown in Figure 6.4 (right) to maximize tool performance. The general

mechanical layout of a modularized, in-line sc-AFM sampling system to sit between fab module and substrate rewind module is shown in Figure 6.5.

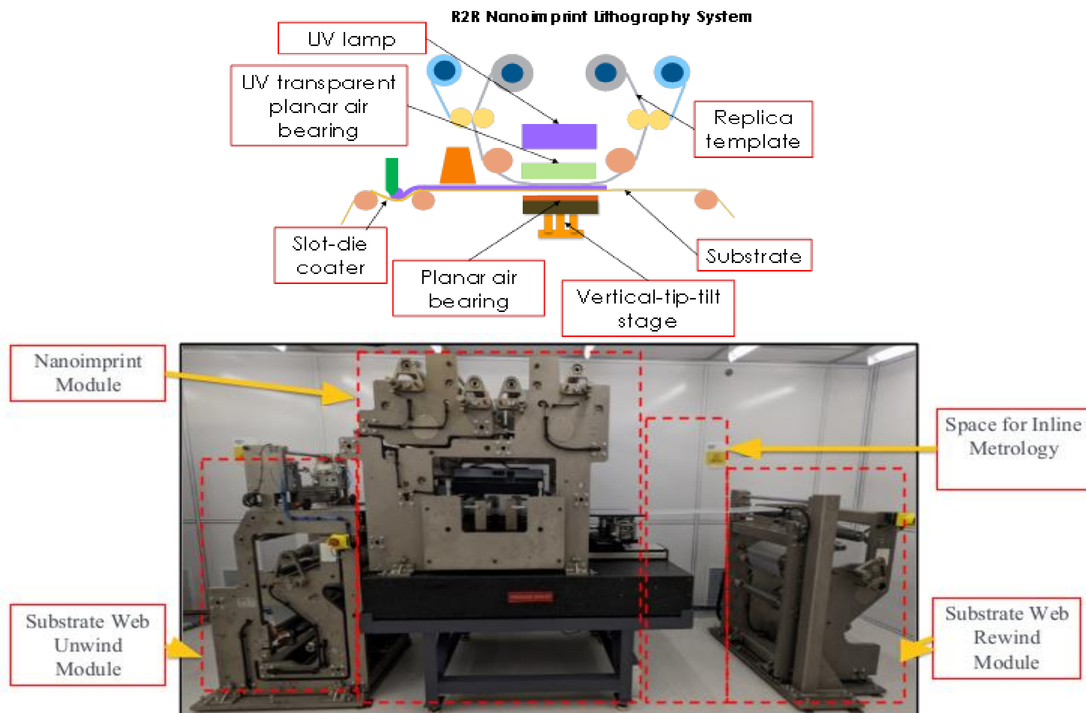

Figure 6.3: Exemplary state-of-the-art R2R nanofabrication tool with design considerations for in-line metrology

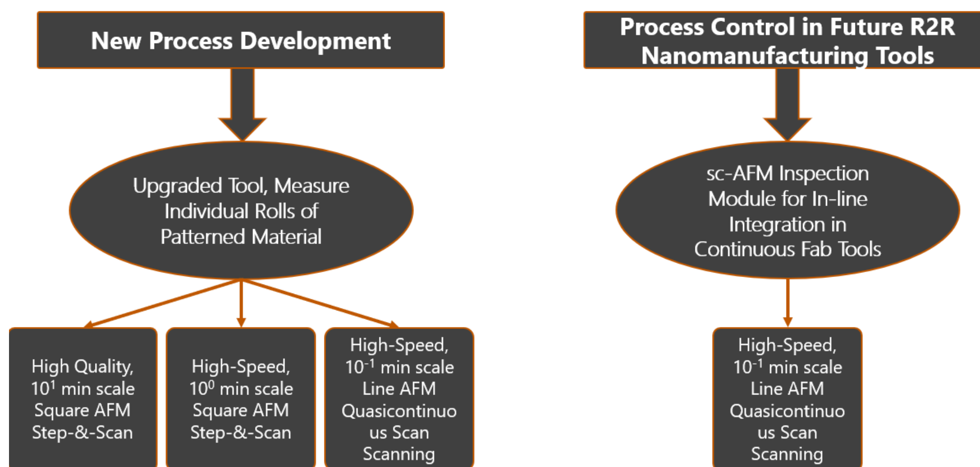

Figure 6.4: Operational modes and applications of the current prototype tool as-designed (left) and future modular applications for true in-line process metrology

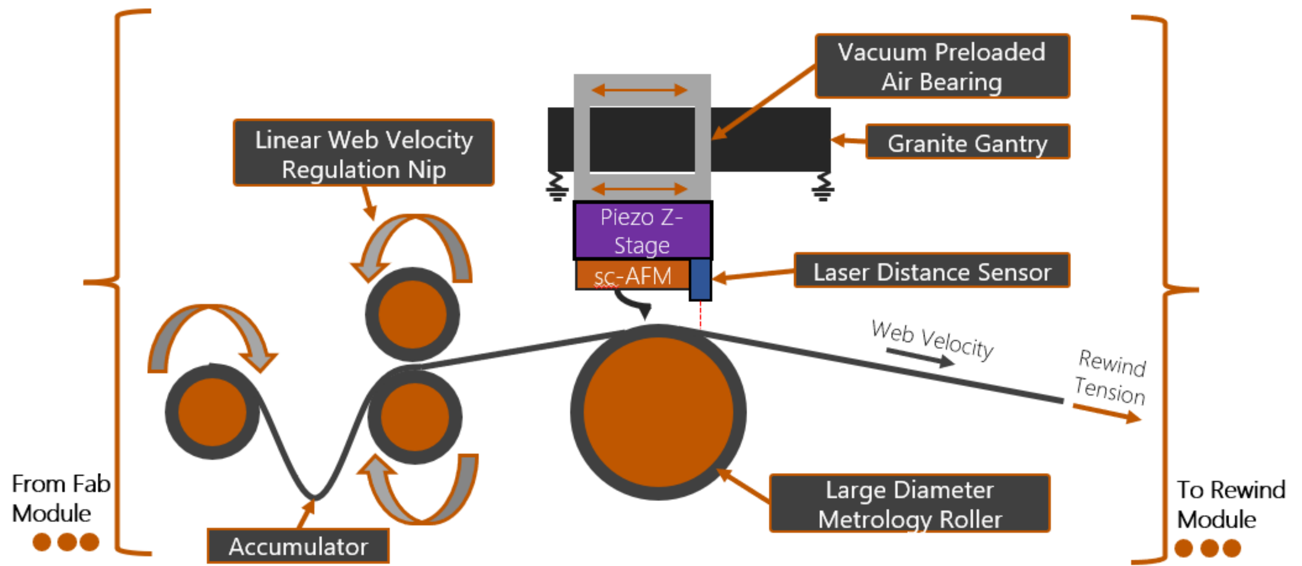

Figure 6.5: Schematic diagram of proposed modularized sc-AFM in-line inspection system

REFERENCES

[1] J. D. Morse, "Nanofabrication Technologies for Roll-to-Roll Processing," *NIST-NNN Workshop*, 2011.

[2] A. Nathan *et al.*, "Flexible electronics: The next ubiquitous platform," *Proceedings of the IEEE*, vol. 100, no. SPL CONTENT, pp. 1486–1517, 2012, doi: 10.1109/JPROC.2012.2190168.

[3] "NextFlex Roadmapping Meeting." Lowell, MA, 2016.

[4] N. Kooy, K. Mohamed, L. T. Pin, and O. S. Guan, "A review of roll-to-roll nanoimprint lithography," *Nanoscale Research Letters*, vol. 9, no. 1, pp. 1–13, 2014, doi: 10.1186/1556-276X-9-320.

[5] Kenneth Carter, "R2R Nanofabrication: A Test Bed Platform for UMass Nanoscale Science Technologies," University of Massachusetts - Amherst, 2011.

[6] J. A. Rogers *et al.*, "Paper-like electronic displays: Large-area rubber-stamped plastic sheets of electronics and microencapsulated electrophoretic inks," *Proceedings of the National Academy of Sciences of the United States of America*, vol. 98, no. 9, pp. 4835–4840, 2001, doi: 10.1073/pnas.091588098.

[7] S. Ahn *et al.*, "Roll-to-roll nanopatterning using jet and flash imprint lithography," 2012, vol. 8323, pp. 83231L-8323–7. [Online]. Available: https://doi.org/10.1117/12.918040

[8] T. R. Andersen *et al.*, "Scalable, ambient atmosphere roll-to-roll manufacture of encapsulated large area, flexible organic tandem solar cell modules," *Energy and Environmental Science*, vol. 7, no. 9, pp. 2925–2933, 2014, doi: 10.1039/c4ee01223b.

[9] M. Bariya *et al.*, "Roll-to-Roll Gravure Printed Electrochemical Sensors for Wearable and Medical Devices," *ACS Nano*, vol. 12, no. 7, pp. 6978–6987, 2018, doi: 10.1021/acsnano.8b02505.

[10] Y. S. Jung, K. Hwang, Y. J. Heo, J. E. Kim, D. Vak, and D. Y. Kim, "Progress in Scalable Coating and Roll-to-Roll Compatible Printing Processes of Perovskite Solar Cells toward Realization of Commercialization," *Advanced Optical Materials*, vol. 6, no. 9, pp. 1–30, 2018, doi: 10.1002/adom.201701182.

[11] G. Kirchner *et al.*, "Toward high volume solution based roll-to-roll processing of OLEDs," *Journal of Materials Research*, vol. 32, no. 12, pp. 2219–2229, 2017, doi: 10.1557/jmr.2017.204.

[12] I.-T. Chen, E. Schappell, X. Zhang, and C.-H. Chang, "Continuous roll-to-roll patterning of three-dimensional periodic nanostructures," *Microsystems & Nanoengineering*, vol. 6, no. 1, p. 22, Dec. 2020, doi: 10.1038/s41378-020-0133-7.

[13] N. Cates *et al.*, "Roll-to-roll nanoimprint lithography using a seamless cylindrical mold nanopatterned with a high-speed mastering process," *Nanotechnology*, 2021, doi: 10.1088/1361-6528/abd9f1.

[14] C.-H. Chang *et al.*, "From Two-Dimensional Colloidal Self-Assembly to Three-Dimensional Nanolithography," *Nano Letters*, vol. 11, no. 6, pp. 2533–2537, Jun. 2011, doi: 10.1021/nl2011824.

[15] H. Subbaraman, X. Lin, X. Xu, A. Dodabalapur, L. J. Guo, and R. T. Chen, "Metrology and Instrumentation Challenges with High-rate, Roll-to-Roll Manufacturing of Flexible Electronic Systems," *Instrumentation, Metrology, and Standards for Nanomanufacturing, Optics, and Semiconductors VI*, vol. 8466, p. 846603, 2012, doi: 10.1117/12.940778.

[16] U. D. of Energy, "Quadrennial technology review: An assessment of energy technologies and research opportunities (September)," US Department of Energy Washington, DC, 2015.
[17] C. Daniel, D. Wood III, G. Krumdick, M. Ulsh, V. Battaglia, and F. Crowson, "Roll-to-Roll Advanced Materials Manufacturing DOE Laboratory Collaboration - FY2018 Final Report," Oak Ridge National Lab. (ORNL), Oak Ridge, TN (United States), ORNL/SPR-2019/1066, Jan. 2019. doi: https://doi.org/10.2172/1502542.
[18] J. A. Liddle and G. M. Gallatin, "Nanomanufacturing: A Perspective," *ACS Nano*, vol. 10, no. 3, pp. 2995–3014, 2016, doi: 10.1021/acsnano.5b03299.
[19] X. Lin *et al.*, "Towards Realizing High-Throughput, Roll-to-Roll Manufacturing of Flexible Electronic Systems," *Electronics*, vol. 3, no. 4, pp. 624–635, Nov. 2014, doi: 10.3390/electronics3040624.
[20] S.-H. Chen and D.-B. Perng, "Automatic optical inspection system for IC molding surface," *J Intell Manuf*, vol. 27, no. 5, pp. 915–926, Oct. 2016, doi: 10.1007/s10845-014-0924-5.
[21] N. Espinosa *et al.*, "OPV for mobile applications: an evaluation of roll-to-roll processed indium and silver free polymer solar cells through analysis of life cycle, cost and layer quality using inline optical and functional inspection tools," *J. Mater. Chem. A*, vol. 1, no. 24, p. 7037, 2013, doi: 10.1039/c3ta01611k.
[22] M. Born, E. Wolf, and A. B. Bhatia, *Principles of optics: electromagnetic theory of propagation, interference, and diffraction of light*. 2019. Accessed: Jan. 26, 2021. [Online]. Available: https://doi.org/10.1017/9781108769914
[23] L. R. F.R.S, "XXXI. Investigations in optics, with special reference to the spectroscope," *The London, Edinburgh, and Dublin Philosophical Magazine and Journal of Science*, vol. 8, no. 49, pp. 261–274, Oct. 1879, doi: 10.1080/14786447908639684.
[24] W. T. Tel *et al.*, "Efficient hybrid metrology for focus, CD, and overlay," in *Metrology, Inspection, and Process Control for Microlithography XXXI*, Mar. 2017, vol. 10145, p. 101452E. doi: 10.1117/12.2257965.
[25] J. Mulkens *et al.*, "Holistic approach for overlay and edge placement error to meet the 5nm technology node requirements," in *Metrology, Inspection, and Process Control for Microlithography XXXII*, Mar. 2018, vol. 10585, p. 105851L. doi: 10.1117/12.2297283.
[26] B. Gawlik *et al.*, "Hyperspectral imaging for high-throughput, spatially resolved spectroscopic scatterometry of silicon nanopillar arrays," *Optics Express*, vol. 28, no. 10, pp. 14209–14221, May 2020, doi: 10.1364/OE.388158.
[27] J. J. Faria-Briceno *et al.*, "Optical angular scatterometry: In-line metrology approach for roll-to-roll and nanoimprint fabrication," *Journal of Vacuum Science & Technology B*, vol. 37, no. 5, p. 052904, Sep. 2019, doi: 10.1116/1.5119707.
[28] "Scanning electron microscope," *Wikipedia*. Jan. 01, 2021. Accessed: Feb. 01, 2021. [Online]. Available: https://en.wikipedia.org/w/index.php?title=Scanning_electron_microscope&oldid=997719588
[29] J. Goldstein *et al.*, "Scanning Electron Microscopy and Microanalysis," in *Physicochemical Methods of Mineral Analysis*, Boston, MA: Springer US, 1975, pp. 421–450. doi: 10.1007/978-1-4684-2046-3_11.
[30] M. von Ardenne, "Das Elektronen-Rastermikroskop," *Z. Physik*, vol. 109, no. 9, pp. 553–572, Sep. 1938, doi: 10.1007/BF01341584.

[31] L. De Broglie, “Waves and Quanta,” *Nature*, vol. 112, no. 2815, Art. no. 2815, Oct. 1923, doi: 10.1038/112540a0.

[32] L. de Broglie, “The reinterpretation of wave mechanics,” *Foundations of Physics*, vol. 1, no. 1, pp. 5–15, Mar. 1970, doi: 10.1007/BF00708650.

[33] J. T. Neumann *et al.*, “High-throughput multi-beam SEM: quantitative analysis of imaging capabilities at IMEC-N10 logic node,” in *Metrology, Inspection, and Process Control for Microlithography XXXI*, Mar. 2017, vol. 10145, p. 101451S. doi: 10.1117/12.2257980.

[34] C. Wang, “Atomic Force Microscope System,” pp. 218–221, 2017, doi: 10.1103/PhysRevLett.56.930.

[35] N. Sarkar, D. Strathearn, G. Lee, M. Olfat, and R. R. Mansour, “A platform technology for metrology, manipulation & automation at the nanoscale,” *International Conference on Manipulation, Automation and Robotics at Small Scales, MARSS 2017 - Proceedings*, 2017, doi: 10.1109/MARSS.2017.8001949.

[36] N. Sarkar, D. Strathearn, G. Lee, M. Olfat, and R. R. Mansour, “A 0.25mm3 Atomic Force Microscope on-a-chip,” in *2015 28th IEEE International Conference on Micro Electro Mechanical Systems (MEMS)*, Jan. 2015, pp. 732–735. doi: 10.1109/MEMSYS.2015.7051062.

[37] N. Sarkar, G. Lee, and R. R. Mansour, “CMOS-MEMS dynamic FM atomic force microscope,” *Transducers 2013*, no. June, pp. 916–919, 2013, doi: 10.1109/Transducers.2013.6626917.

[38] D. Strathearn, N. Sarkar, G. Lee, M. Olfat, and R. R. Mansour, “The benefits of miniaturization of an atomic force microscope,” *Proceedings of the IEEE International Conference on Micro Electro Mechanical Systems (MEMS)*, pp. 1363–1366, 2017, doi: 10.1109/MEMSYS.2017.7863674.

[39] T.-F. Yao, L. G. Connolly, and M. Cullinan, “Expanded area metrology for tip-based wafer inspection in the nanomanufacturing of electronic devices,” *Journal of Micro/Nanolithography, MEMS, and MOEMS*, vol. 18, no. 03, p. 1, Sep. 2019, doi: 10.1117/1.JMM.18.3.034003.

[40] K. Jain, S. Member, M. Klosner, and M. Zemel, “Flexible Electronics and Displays : Lithography and Photoablation Processing Technologies for High-Throughput Production,” *Proceedings of the Ieee*, vol. 93, no. 8, 2005.

[41] C. Land, “Baggy paper webs: Effect of uneven moisture and grammage profiles in different process steps,” p. 59.

[42] T. Sorsa, H. N. Koivo, and R. Korhonen, “Application of Neural Networks in the Detection of Breaks in a Paper Machine,” *IFAC Proceedings Volumes*, vol. 25, no. 4, pp. 219–224, Apr. 1992, doi: 10.1016/S1474-6670(17)50244-X.

[43] J. A. Beisel and J. K. Good, “The Instability of Webs in Transport,” *Journal of Applied Mechanics*, vol. 78, no. 1, p. 011001, Jan. 2011, doi: 10.1115/1.4002116.

[44] Wennerblom A., “Twist Warp. Causes and Remedies.,” *JAPAN TAPPI JOURNAL*, vol. 46, no. 4, pp. 501–505, 1992, doi: 10.2524/jtappij.46.501.

[45] H. Hashimoto, P. Jeenkour, and M. Mongkolowongrojn, “Optimum Winding Tension and Nip-load into Wound Webs for Protecting Wrinkles and Slippage,” *JAMDSM*, vol. 4, no. 1, pp. 214–225, 2010, doi: 10.1299/jamdsm.4.214.

[46] Y. B. Chang, S. J. Fox, D. G. Liley, and P. M. Moretti, “Aerodynamics of moving belts, tapes, and webs,” *American Society of Mechanical Engineers, Design Engineering Division (Publication) DE*, 1991.

[47] Y. Watanabe, S. Suzuki, M. Sugihara, and Y. Sueoka, "AN EXPERIMENTAL STUDY OF PAPER FLUTTER," *Journal of Fluids and Structures*, vol. 16, no. 4, pp. 529–542, May 2002, doi: 10.1006/jfls.2001.0435.
[48] S. Hikita and H. Hashimoto, "Improvement of Slippage and Wrinkling of Transporting Webs Using Micro-Grooved Rollers," *JAMDSM*, vol. 4, no. 1, pp. 226–237, 2010, doi: 10.1299/jamdsm.4.226.
[49] D. R. Roisum, "THE MECHANICS OF WEB SPREADING," p. 40.
[50] G. E. Young and K. N. Reid, "Lateral and Longitudinal Dynamic Behavior and Control of Moving Webs," *Journal of Dynamic Systems, Measurement, and Control*, vol. 115, no. 2B, p. 309, 2008, doi: 10.1115/1.2899071.
[51] J. J. Shelton and K. N. Reid, "Lateral Dynamics of a Real Moving Web," *Journal of Dynamic Systems, Measurement, and Control*, vol. 93, no. 3, p. 180, 2010, doi: 10.1115/1.3426494.
[52] E. Laroche and D. Knittel, "An improved linear fractional model for robustness analysis of a winding system," *Control Engineering Practice*, vol. 13, no. 5, pp. 659–666, 2005, doi: 10.1016/j.conengprac.2004.05.008.
[53] N. Jacques, A. Elias, M. Potier-Ferry, and H. Zahrouni, "Buckling and wrinkling during strip conveying in processing lines," *Journal of Materials Processing Technology*, vol. 190, no. 1–3, pp. 33–40, Jul. 2007, doi: 10.1016/j.jmatprotec.2007.03.117.
[54] G. Brandenburg, "NEW MATHEMATICAL MODELS FOR WEB TENSION AND REGISTER ERROR," 1977.
[55] D. P. Campbell and T. Teichmann, "Process Dynamics: Dynamic Behavior of the Production Process," *Physics Today*, vol. 12, no. 6, pp. 46–48, 2009, doi: 10.1063/1.3060854.
[56] K. P. Grenfell, "Tension Control Paper-Making and Converting Machinery," *IEEE Transactions on Applications and Industry*, vol. 83, no. 73, pp. 234–240, 2010, doi: 10.1109/tai.1964.5407746.
[57] H. K. Shin, "Distributed Control of Tension in Multi-Span Web Transport Systems," *Ph.D. thesis, Oklahoma State University, Stillwater, Oklahoma.*, 1991.
[58] H. Koç, D. Knittel, M. De Mathelin, and G. Abba, "Modeling and robust control of winding systems for elastic webs," *IEEE Transactions on Control Systems Technology*, vol. 10, no. 2, pp. 197–208, 2002, doi: 10.1109/87.987065.
[59] A. Seshadri and P. R. Pagilla, "Optimal Web Guiding," *Journal of Dynamic Systems, Measurement, and Control*, vol. 132, no. 1, p. 011006, 2009, doi: 10.1115/1.4000074.
[60] T. Sakamoto and Y. Fujino, "Modelling and Analysis of a Web Tension Control System".
[61] X. Guan, M. S. High, and D. A. Tree, "Viscoelastic Effects in Modeling Web Handling Systems: Steady-State Analysis," *Journal of Applied Mechanics*, vol. 62, no. 4, p. 908, 2008, doi: 10.1115/1.2896021.
[62] G. Y. Kim, H. M. Kim, J. M. Shin, and J. S. Kim, "Modeling and Feed-forward Velocity Compensation of Multi-span Web Transport Systems with Thermal and Gravity Effects," *ISIJ International*, vol. 48, no. 6, pp. 799–808, 2008, doi: 10.2355/isijinternational.48.799.
[63] Y. Lu and P. R. Pagilla, "Modeling of Temperature Distribution in Moving Webs in Roll-to-Roll Manufacturing," *Journal of Thermal Science and Engineering Applications*, vol. 6, no. 4, p. 041012, 2014, doi: 10.1115/1.4028048.
[64] E. O. Cobos Torres and P. R. Pagilla, "Temperature Distribution in Moving Webs Heated by Radiation Panels: Model Development and Experimental Validation," *Journal of*

Dynamic Systems, Measurement, and Control, vol. 139, no. 5, p. 051003, 2016, doi: 10.1115/1.4035297.

[65] D. P. D. Whitworth and M. C. Harrison, "Tension variations in pliable material in production machinery," *Applied Mathematical Modelling*, vol. 7, no. 3, pp. 189–196, 1983, doi: 10.1016/0307-904X(83)90008-2.

[66] C. Branca, P. R. Pagilla, and K. N. Reid, "Governing Equations for Web Tension and Web Velocity in the Presence of Nonideal Rollers," *Journal of Dynamic Systems, Measurement, and Control*, vol. 135, no. 1, p. 011018, 2012, doi: 10.1115/1.4007974.

[67] B. A. Ross and N. Woo, "Early Experiences in Using Multibody Dynamics Software to Simulate Flexible Webs in Production," in *Volume 4: 7th International Conference on Multibody Systems, Nonlinear Dynamics, and Control, Parts A, B and C*, San Diego, California, USA, Jan. 2009, pp. 1545–1550. doi: 10.1115/DETC2009-86719.

[68] L. Sievers, M. J. Balas, and A. von Flotow, "Modeling of web conveyance systems for multivariable control," *IEEE Trans. Automat. Contr.*, vol. 33, no. 6, pp. 524–531, Jun. 1988, doi: 10.1109/9.1247.

[69] G. E. Young, J. J. Shelton, and C. Kardamilas, "Modeling and Control of Multiple Web Spans Using State Estimation," *Journal of Dynamic Systems, Measurement, and Control*, vol. 111, no. 3, p. 505, 2009, doi: 10.1115/1.3153081.

[70] C. E. Kardamilas and G. E. Young, "Stochastic Modeling of Lateral Web Dynamics," no. 1958, pp. 474–480, 2018, doi: 10.23919/acc.1990.4790781.

[71] R. C. Benson, "Lateral Dynamics of a Moving Web With Geometrical Imperfection," *Journal of Dynamic Systems, Measurement, and Control*, vol. 124, no. 1, p. 25, 2002, doi: 10.1115/1.1435643.

[72] J. B. Yerashunas, J. A. De Abreu-Garcia, and T. T. Hartley, "Control of Lateral Motion in Moving Webs," *IEEE Transactions on Control Systems Technology*, vol. 11, no. 5, pp. 684–693, 2003, doi: 10.1109/TCST.2003.816409.

[73] H. Wang, D. Logghe, and D. Miskin, "Physical modelling and control of lateral web position for wallpaper making processes," *Control Engineering Practice*, vol. 13, no. 4, pp. 401–412, 2005, doi: 10.1016/j.conengprac.2004.02.014.

[74] S. Kee-Hyun and K. Soon-Oh, "The effect of tension on the lateral dynamics and control of a moving web," *IEEE Transactions on Industry Applications*, vol. 43, no. 2, pp. 403–411, 2007, doi: 10.1109/tia.2006.889742.

[75] E. O. Cobos Torres and P. R. Pagilla, "Spatially Dependent Transfer Functions for Web Lateral Dynamics in Roll-to-Roll Manufacturing," *Journal of Dynamic Systems, Measurement, and Control*, vol. 140, no. 11, p. 111011, 2018, doi: 10.1115/1.4040216.

[76] T. Sakamoto and S. Tanaka, "Interaction measures for the decentralized tension control system," pp. 649–654, 2002, doi: 10.1109/isie.2000.930374.

[77] T. Sakamoto and T. Kobayashi, "Decomposition and decentralized controller design of web transfer system," *IFAC Proceedings Volumes (IFAC-PapersOnline)*, vol. 37, no. 11, pp. 135–140, 2004, doi: 10.1016/S1474-6670(17)31602-6.

[78] J.-C. Park, S. W. Jeon, K. S. Nam, and C. H. Kim, "Variable PID Gain Control of Winder Tension of Roll-to-Roll Printing System using Estimation of Winder-Roll Radius," *Journal of manufacturing engineering & technology*, vol. 22, no. 4, pp. 755–760, 2013, doi: 10.7735/ksmte.2013.22.4.755.

[79] J. C. Park, S. W. Jeon, K. S. Nam, L. Liu, J. Sun, and C. H. Kim, "Tension control of web of winder span using adaptive gain control method," *Japanese Journal of Applied Physics*, vol. 53, no. 5 SPEC. ISSUE 3, pp. 1–7, 2014, doi: 10.7567/JJAP.53.05HC11.
[80] M. Yang and S. Zhang, "The research of tension control system in web press based on the fuzzy adaptive PID controller," *Proceedings of the 2014 9th IEEE Conference on Industrial Electronics and Applications, ICIEA 2014*, no. 1, pp. 1204–1208, 2014, doi: 10.1109/ICIEA.2014.6931349.
[81] P. R. Raul and P. R. Pagilla, "Design and implementation of adaptive PI control schemes for web tension control in roll-to-roll (R2R) manufacturing," *ISA Transactions*, vol. 56, pp. 276–287, May 2015, doi: 10.1016/j.isatra.2014.11.020.
[82] E. J. M. Geddes and I. Postlethwaite, "Improvements in product quality in tandem cold rolling using robust multivariable control," *IEEE Transactions on Control Systems Technology*, vol. 6, no. 2, pp. 257–269, 1998, doi: 10.1109/87.664192.
[83] D. Knittel, E. Laroche, D. Gigan, and H. Koç, "Tension control for winding systems with two-degrees-of-freedom H ∞ controllers," *IEEE Transactions on Industry Applications*, vol. 39, no. 1, pp. 113–120, 2003, doi: 10.1109/TIA.2002.807231.
[84] M. D. Baumgart and L. Y. Pao, "Robust Lyapunov-Based Feedback Control of Nonlinear Web-Winding Systems," *Proceedings of the IEEE Conference on Decision and Control*, vol. 6, no. December, pp. 6398–6405, 2003, doi: 10.1109/CDC.2003.1272347.
[85] D. Kuhm, D. Knittel, and M. A. Bueno, "Robust control strategies for an electric motor driven accumulator with elastic webs," *ISA Transactions*, vol. 51, no. 6, pp. 732–742, 2012, doi: 10.1016/j.isatra.2012.05.004.
[86] J. Frechard and D. Knittel, "ESDA2012-82552," pp. 1–8, 2016.
[87] P. R. Pagilla, R. V. Dwivedula, Y. Zhu, and L. P. Perera, "Periodic Tension Disturbance Attenuation in Web Process Lines Using Active Dancers," *Journal of Dynamic Systems, Measurement, and Control*, vol. 125, no. 3, p. 361, 2003, doi: 10.1115/1.1590678.
[88] R. V. Dwivedula, Y. Zhu, and P. R. Pagilla, "Characteristics of active and passive dancers: A comparative study," *Control Engineering Practice*, vol. 14, no. 4, pp. 409–423, 2006, doi: 10.1016/j.conengprac.2005.02.003.
[89] T. J. Manayathara, T. Tsao, J. Bentsman, and D. Ross, "Rejection of Unknown Periodic Load Disturbances," *Control*, vol. 4, no. 3, pp. 259–265, 1996.
[90] G. Ma and P. R. Pagilla, "Design of a Periodic Event-Based Repetitive Controller With Dynamic Output Feedback for Linear Systems," p. V003T30A009, 2018, doi: 10.1115/dscc2018-9146.
[91] D. O. F. Engineering, "Novel Control Approaches for Web Tension Regulation," 2001.
[92] W. Zhou and Z. Gao, "An active disturbance rejection approach to tension and velocity regulations in web processing lines," *Proceedings of the IEEE International Conference on Control Applications*, no. October, pp. 842–848, 2007, doi: 10.1109/CCA.2007.4389338.
[93] T. Fechner, D. Neumerkel, and I. Keller, "Adaptive neural network filter for steel rolling," pp. 3915–3920 vol.6, 2002, doi: 10.1109/icnn.1994.374837.
[94] F. L. Luo, "Multiple-page-mapping backpropagation neural network for constant tension control," *IEE Proceedings - Electric Power Applications*, vol. 145, no. 3, p. 239, 2002, doi: 10.1049/ip-epa:19981803.

[95] C. Wang, Y. Wang, R. Yang, and H. Lu, "Research on precision tension control system based on neural network," *IEEE Transactions on Industrial Electronics*, vol. 51, no. 2, pp. 381–386, 2004, doi: 10.1109/TIE.2003.822096.

[96] M. Rau and D. Schröder, "Compensation of Periodic Disturbances in Continuous Processing Plants by Means of a Neural Controller," no. September, pp. 85–106, 2011, doi: 10.1007/978-94-010-0324-7_6.

[97] C. L. Chen, K. M. Chang, and C. M. Chang, "Modeling and control of a web-fed machine," *Applied Mathematical Modelling*, vol. 28, no. 10, pp. 863–876, 2004, doi: 10.1016/j.apm.2004.04.005.

[98] F. Janabi-Sharifi, "A neuro-fuzzy system for looper tension control in rolling mills," *Control Engineering Practice*, vol. 13, no. 1, pp. 1–13, 2005, doi: 10.1016/j.conengprac.2003.09.013.

[99] N. I. Giannoccaro, I. Uchitomi, and T. Sakamoto, "Decentralized neuro-fuzzy control of an experimental web transport platform," *IECON Proceedings (Industrial Electronics Conference)*, pp. 518–523, 2016, doi: 10.1109/IECON.2016.7793587.

[100] K. M. Tahk and K. H. Shin, "A study on the fault diagnosis of roller-shape using frequency analysis of tension signals and artificial neural networks based approach in a web transport system," *KSME International Journal*, vol. 16, no. 12, pp. 1604–1612, 2002, doi: 10.1007/BF03021662.

[101] S. H. Ahn and L. J. Guo, "High-Speed Roll-to-Roll Nanoimprint Lithography on Flexible Plastic Substrates," *Adv. Mater.*, vol. 20, no. 11, pp. 2044–2049, Jun. 2008, doi: 10.1002/adma.200702650.

[102] H. Tao, N. I. Landy, C. M. Bingham, X. Zhang, R. D. Averitt, and W. J. Padilla, "A metamaterial absorber for the terahertz regime: design, fabrication and characterization," *Opt. Express*, vol. 16, no. 10, p. 7181, May 2008, doi: 10.1364/OE.16.007181.

[103] C. Strohhöfer *et al.*, "Roll-To-Roll Microfabrication of Polymer Microsystems," *Measurement and Control*, vol. 40, no. 3, pp. 80–83, 2013, doi: 10.1177/002029400704000305.

[104] H. Kang, C. Lee, and K. Shin, "A novel cross directional register modeling and feedforward control in multi-layer roll-to-roll printing," *Journal of Process Control*, vol. 20, no. 5, pp. 643–652, 2010, doi: 10.1016/j.jprocont.2010.02.015.

[105] S. Park, J. Park, D. Lee, J. Lee, K.-H. Shin, and J. Seong, "Register control algorithm for high resolution multilayer printing in the roll-to-roll process," *Mechanical Systems and Signal Processing*, vol. 60–61, pp. 706–714, 2015, doi: 10.1016/j.ymssp.2015.01.028.

[106] K. Jain, M. Zemel, and M. Klosner, "Large-area high-resolution lithography and photoablation systems for microelectronics and optoelectronics fabrication," *Proceedings of the IEEE*, vol. 90, no. 10, pp. 1681–1688, 2002, doi: 10.1109/JPROC.2002.803662.

[107] C. C. H. Kim, S. W. Jeon, and C. C. H. Kim, "Measurement of position accuracy of engraving in plate roller and its effect on register accuracy in roll-to-roll multi-layer printing," *Measurement Science and Technology*, vol. 28, no. 12, 2017, doi: 10.1088/1361-6501/aa8ffa.

[108] T. Nagai, S. Naka, H. Okada, and H. Onnagawa, "Organic field-effect transistor integrated circuits using self-alignment process technology," *Japanese Journal of Applied Physics, Part 1: Regular Papers and Short Notes and Review Papers*, vol. 46, no. 4 B, pp. 2666–2668, 2007, doi: 10.1143/JJAP.46.2666.

[109] S. Jussila, M. Puustinen, T. Hassinen, J. Olkkonen, H. G. O. Sandberg, and K. Solehmainen, “Self-aligned patterning method of poly(aniline) for organic field-effect transistor gate electrode,” *Organic Electronics: physics, materials, applications*, vol. 13, no. 8, pp. 1308–1314, 2012, doi: 10.1016/j.orgel.2012.04.004.
[110] *2008. Novel Combination Technology of the Printing and Self-aligned Process for Organic Thin Film Transistor.pdf*.
[111] H. Gold *et al.*, “Self-aligned flexible organic thin-film transistors with gates patterned by nano-imprint lithography,” *Organic Electronics: physics, materials, applications*, vol. 22, pp. 140–146, 2015, doi: 10.1016/j.orgel.2015.03.047.
[112] M. Vilkman, T. Ruotsalainen, E. Jansson, K. Solehmainen, and J. Hiitola-Keinänen, “Self-Aligned Metal Electrodes in Fully Roll-to-Roll Processed Organic Transistors,” *Electronics*, vol. 5, no. 4, p. 2, 2016, doi: 10.3390/electronics5010002.
[113] C. W. Sele, T. Von Werne, R. H. Friend, and H. Sirringhaus, “Lithography-free, self-aligned inkjet printing with sub-hundred-nanometer resolution,” *Advanced Materials*, vol. 17, no. 8, pp. 997–1001, 2005, doi: 10.1002/adma.200401285.
[114] Y. Li, Y. Wu, H. Sirringhaus, N. Zhao, B. Ong, and M. Chiesa, “Self-aligned inkjet printing of highly conducting gold electrodes with submicron resolution,” *Journal of Applied Physics*, vol. 101, no. 6, p. 064513, 2007, doi: 10.1063/1.2496249.
[115] H. Y. Tseng and V. Subramanian, “All inkjet-printed, fully self-aligned transistors for low-cost circuit applications,” *Organic Electronics: physics, materials, applications*, vol. 12, no. 2, pp. 249–256, 2011, doi: 10.1016/j.orgel.2010.11.013.
[116] Y. Y. Noh, N. Zhao, M. Caironi, and H. Sirringhaus, “Downscaling of self-aligned, all-printed polymer thin-film transistors,” *Nature Nanotechnology*, vol. 2, no. 12, pp. 784–789, 2007, doi: 10.1038/nnano.2007.365.
[117] H. Y. Tseng and V. Subramanian, “All inkjet printed self-aligned transistors and circuits applications,” *Technical Digest - International Electron Devices Meeting, IEDM*, no. 510, pp. 391–394, 2009, doi: 10.1109/IEDM.2009.5424343.
[118] H.-J. Kim *et al.*, “Roll-to-roll manufacturing of electronics on flexible substrates using self-aligned imprint lithography (SAIL),” *Journal of the Society for Information Display*, vol. 17, no. 11, p. 963, 2009, doi: 10.1889/jsid17.11.963.
[119] P. Maury, N. Stroeks, M. Wijnen, R. Tacken, and R. van der Werf, “Roll-to-Roll UV Imprint for Bottom-up Transistor Fabrication,” *Journal of Photopolymer Science and Technology*, vol. 24, no. 1, pp. 43–45, 2011, doi: 10.2494/photopolymer.24.43.
[120] P. Maury *et al.*, “Roll-to-roll UV imprint lithography for flexible electronics,” *Microelectronic Engineering*, vol. 88, no. 8, pp. 2052–2055, 2011, doi: 10.1016/j.mee.2011.02.022.
[121] E. Lausecker, Y. Huang, T. Fromherz, J. C. Sturm, and S. Wagner, “Self-aligned imprint lithography for top-gate amorphous silicon thin-film transistor fabrication,” *Applied Physics Letters*, vol. 96, no. 26, pp. 2–4, 2010, doi: 10.1063/1.3457446.
[122] Z. H. Chen and P. S. Huang, “A vision-based method for planar position measurement,” *Measurement Science and Technology*, vol. 27, no. 12, p. 125018, 2016, doi: 10.1088/0957-0233/27/12/125018.
[123] R. Nakahara, M. Uno, T. Uemura, K. Takimiya, and J. Takeya, “Flexible three-dimensional organic field-effect transistors fabricated by an imprinting technique,” *Advanced Materials*, vol. 24, no. 38, pp. 5212–5216, 2012, doi: 10.1002/adma.201201234.

[124] S. P. Li, C. J. Newsome, T. Kugler, M. Ishida, and S. Inoue, “Polymer thin film transistors with self-aligned gates fabricated using ink-jet printing,” *Applied Physics Letters*, vol. 90, no. 17, pp. 3–5, 2007, doi: 10.1063/1.2731527.
[125] S. Li, W. Chen, D. Chu, and S. Roy, “Self-aligned high-resolution printed polymer transistors,” *Advanced Materials*, vol. 23, no. 35, pp. 4107–4110, 2011, doi: 10.1002/adma.201101291.
[126] J. Jeon, B. C. K. Tee, B. Murmann, and Z. Bao, “Micro-imprinted prism substrate for self-aligned short channel organic transistors on a flexible substrate,” *Applied Physics Letters*, vol. 100, no. 4, pp. 2–5, 2012, doi: 10.1063/1.3679119.
[127] D. E. Hardt and T. Supervisor, “Design and Manufacturing of High Precision Roll-to-Roll Multilayer Printing Machine - Machine Upgrade,” no. 2008, 2009.
[128] C. A. (MIT) Datar, *Design and Development of High Precision Elastomeric-Stamp Wrapping System for Roll-to-Roll Multi-Layer Microcontact Printing*. 2009.
[129] L. Yin, Y. Ding, Y. Shi, W. Jiang, and H. Liu, “Roller-reversal imprint process for preparation of large-area microstructures,” *Journal of Vacuum Science & Technology B, Nanotechnology and Microelectronics: Materials, Processing, Measurement, and Phenomena*, vol. 28, no. 1, pp. 104–109, 2010, doi: 10.1116/1.3272717.
[130] S. Choi *et al.*, “The effect of mold materials on the overlay accuracy of a roll-to-roll imprinting system using UV LED illumination within a transparent mold,” *Journal of Micromechanics and Microengineering*, vol. 26, no. 6, p. 65004, 2016, doi: 10.1088/0960-1317/26/6/065004.
[131] H. Koo *et al.*, “Scalability of carbon-nanotube-based thin film transistors for flexible electronic devices manufactured using an all roll-To-roll gravure printing system,” *Scientific Reports*, vol. 5, no. September, pp. 1–11, 2015, doi: 10.1038/srep14459.
[132] C. H. Kim, J. Jo, and S. H. Lee, “Design of roll-to-roll printing equipment with multiple printing methods for multi-layer printing,” *Review of Scientific Instruments*, vol. 83, no. 6, pp. 1–8, 2012, doi: 10.1063/1.4726018.
[133] X. Lin *et al.*, “Towards Realizing High-Throughput, Roll-to-Roll Manufacturing of Flexible Electronic Systems,” *Electronics*, vol. 3, no. 4, pp. 624–635, Nov. 2014, doi: 10.3390/electronics3040624.
[134] J. Lee, P. Isto, H. Jeong, J. Park, D. Lee, and K. H. Shin, “Register mark measurement errors in high-precision roll-to-roll continuous systems: The effect of register mark geometry on measurement error,” *Applied Physics Letters*, vol. 109, no. 14, 2016, doi: 10.1063/1.4964262.
[135] J. Lee, S. Park, K. H. Shin, and H. Jung, “Smearing defects: a root cause of register measurement error in roll-to-roll additive manufacturing system,” *International Journal of Advanced Manufacturing Technology*, vol. 98, no. 9–12, pp. 3155–3165, 2018, doi: 10.1007/s00170-018-2465-0.
[136] E. Lee, Y. M. Choi, S. H. Lee, S. Kwon, T. M. Lee, and D. Kang, “Enhancement of printing overlay accuracy by reducing the effects of mark deformations,” *Microelectronic Engineering*, vol. 180, pp. 8–14, 2017, doi: 10.1016/j.mee.2017.05.046.
[137] R. M. M. Printing, P. Baldesi, and D. E. Hardt, “Design and Development of High Precision Five-Axis Positioning Submitted to the Department of Mechanical Engineering in partial by,” 2009.
[138] C. Doignon, D. Knittel, and X. Maurice, “A vision-based technique for edge displacement and vibration estimations of a moving flexible web,” *IEEE Transactions on*

Instrumentation and Measurement, vol. 57, no. 8, pp. 1605–1613, 2008, doi: 10.1109/TIM.2008.925712.
[139] Y. Seo, Y. M. Kim, and D. Oh, “A position measurement system for precision alignment of roll-to-roll printing and sensitivity analysis of thermal deformation,” *Microsystem Technologies*, vol. 19, no. 9–10, pp. 1539–1548, 2013, doi: 10.1007/s00542-013-1849-1.
[140] M. Jung, Y. Kim, and D. Oh, “A robust position measurement system for precision alignment of roll to roll printing using alignment patterns and light quantity,” *Microsystem Technologies*, 2016, doi: 10.1007/s00542-016-2861-z.
[141] D. Kang, Y. Duk Kim, E. Lee, Y. M. Choi, T. M. Lee, and D. Kim, “Direct and precise measurement of displacement and velocity of flexible web in roll-to-roll manufacturing systems,” *Review of Scientific Instruments*, vol. 84, no. 12, pp. 1–12, 2013, doi: 10.1063/1.4831816.
[142] D. O’Connor *et al.*, “High precision interferometric optical encoder for inline position referencing of instrumented plastic film in a Roll-to-Roll system,” *Proc. ASPE 2016 Annual Meeting*, vol. 9, no. 9, pp. 3461–3482, 2016, doi: 10.5194/gmd-9-3461-2016.
[143] C. Li, H. Xu, and S.-C. Chen, “Design of a precision multi-layer roll-to-roll printing system,” *Precision Engineering*, vol. 66, pp. 564–576, Nov. 2020, doi: 10.1016/j.precisioneng.2020.08.013.
[144] L. Hu, W. Chen, W. Chen, and Z. Liu, “An active register control strategy for multilayer R2R printed electronics based on microscope vision,” *Proceedings of the 13th IEEE Conference on Industrial Electronics and Applications, ICIEA 2018*, pp. 2590–2595, 2018, doi: 10.1109/ICIEA.2018.8398148.
[145] H. Kang, C. Lee, and K. Shin, “Modeling and compensation of the machine directional register in roll-to-roll printing,” *Control Engineering Practice*, vol. 21, no. 5, pp. 645–654, 2013, doi: 10.1016/j.conengprac.2012.09.012.
[146] H. K. Kang, C. W. Lee, and K. H. Shin, “Novel modeling of correlation between two-dimensional registers in large-area multilayered roll-to-roll printed electronics,” *Japanese Journal of Applied Physics*, vol. 50, no. 1, pp. 1–7, 2011, doi: 10.1143/JJAP.50.016701.
[147] H. Kang, C. Lee, and K. Shin, *Two-dimensional register modeling and control in multi-layer roll-to-roll e-printing systems*, vol. 44. IFAC, 2011. doi: 10.3182/20110828-6-IT-1002.03667.
[148] H. Kang and R. R. Baumann, “Mathematical modeling and simulations for machine directional register in hybrid roll-to-roll printing systems,” *International Journal of Precision Engineering and Manufacturing*, vol. 15, no. 10, pp. 2109–2116, 2014, doi: 10.1007/s12541-014-0570-z.
[149] J. Lee, K. Shin, and C. Lee, “Analysis of dynamic thermal characteristic of register of roll-to-roll multi-layer printing systems,” *Robotics and Computer-Integrated Manufacturing*, vol. 35, pp. 77–83, 2015, doi: 10.1016/j.rcim.2015.02.008.
[150] J. Lee, K. Shin, and H. Kang, “Design of a register controller considering inherent characteristics of a roll-to-roll continuous manufacturing system,” 2019, doi: 10.1007/s00170-019-03428-4.
[151] " BY R.B. TAIT A DISCUSSION OF THE PAPER "IN SITU DOUBLE TORSION FRACTURE STUDIES OF CEMENT MORTAR AND CEMENT PASTE INSIDE A SCANNING ELECTRON MICROSCOPE and G. G. GARRETT, “No Title『新版 リヒャルト・ワーグナーの芸術』,” vol. 155, no. 1986, p. 1986, 1987.

[152] T. Yoshida, S. Takagi, Y. Muto, and T. Shen, "Register control of rotogravure printing press. Application of nonlinear control theory to sectional drive printing press," *Electronics and Communications in Japan*, vol. 94, no. 1, pp. 17–24, 2011, doi: 10.1002/ecj.10282.
[153] S. Liu, X. Mei, J. Li, and L. Ma, "Machine Directional Register System Modeling for Shaft-Less Drive Gravure Printing Machines," *Mathematical Problems in Engineering*, vol. 2013, pp. 1–10, 2013, doi: 10.1155/2013/251636.
[154] S. Liu, B. Yin, L. Ma, H. Xu, and G. Zhu, "A Decoupling Control Strategy for Multilayer Register System in Printed Electronic Equipment," *Mathematical Problems in Engineering*, vol. 2016, pp. 1–14, 2016, doi: 10.1155/2016/7165163.
[155] A. Seshadri and P. R. Pagilla, "Interaction analysis of control systems employed in roll-to-roll printing," *2013 American Control Conference*, pp. 4251–4256, 2014, doi: 10.1109/acc.2013.6580493.
[156] A. Seshadri and P. R. Pagilla, "DSCC2013-3992," pp. 1–10, 2016.
[157] K. H. Choi *et al.*, "Web register control algorithm for roll-to-roll system based printed electronics," *2010 IEEE International Conference on Automation Science and Engineering, CASE 2010*, no. May 2017, pp. 867–872, 2010, doi: 10.1109/COASE.2010.5583949.
[158] Y. T. Cho, D. Kim, Y. G. Jung, S. Kwon, and E. S. Hwang, "Positional accuracy of micropatterns in the roll-to-roll imprinting process using a wrapped roll mold," *Journal of Mechanical Science and Technology*, vol. 29, no. 4, pp. 1697–1702, 2015, doi: 10.1007/s12206-015-0342-4.
[159] A. Seshadri, P. R. Pagilla, and J. E. Lynch, "Modeling Print Registration in Roll-to-Roll Printing Presses," *Journal of Dynamic Systems, Measurement, and Control*, vol. 135, no. 3, p. 031016, 2013, doi: 10.1115/1.4023761.
[160] Z. Chen, Y. Zheng, T. Zhang, D. S. H. Wong, and Z. Deng, "Modeling and Register Control of the Speed-Up Phase in Roll-to-Roll Printing Systems," *IEEE Transactions on Automation Science and Engineering*, vol. PP, pp. 1–12, 2018, doi: 10.1109/TASE.2018.2881994.
[161] E. Sutanto and A. G. Alleyne, "Vision based Iterative Learning Control for a roll to roll micro/nano-manufacturing system," *IFAC Proceedings Volumes (IFAC-PapersOnline)*, vol. 19, pp. 7202–7207, 2014.
[162] J. H. Noh, I. Kim, S. H. Park, J. Jo, D. S. Kim, and T. M. Lee, "A study on the enhancement of printing location accuracy in a roll-to-roll gravure offset printing system," *International Journal of Advanced Manufacturing Technology*, vol. 68, no. 5–8, pp. 1147–1153, 2013, doi: 10.1007/s00170-013-4907-z.
[163] H. Zhang, M. D. Poliks, and B. Sammakia, "A roll-to-roll photolithography process for establishing accurate multilayer registration on large area flexible films," *IEEE/OSA Journal of Display Technology*, vol. 6, no. 11, pp. 571–578, 2010, doi: 10.1109/JDT.2010.2077618.
[164] J. Chang *et al.*, "Overlay accuracy on a flexible web with a roll printing process based on a roll-to-roll system," *Review of Scientific Instruments*, vol. 86, no. 5, 2015, doi: 10.1063/1.4921495.
[165] Y.-M. Choi *et al.*, "Development of a precision reverse offset printing system," *Review of Scientific Instruments*, vol. 87, no. 1, p. 015102, 2016, doi: 10.1063/1.4939237.

[166] M. Meng, L. Tu, J. Mi, H. Zhou, and X. Zou, "Machine learning and hybrid metrology using HV-SEM and optical methods to monitor channel hole tilting in-line for 3D NAND wafer production," in *Metrology, Inspection, and Process Control for Microlithography XXXIV*, Mar. 2020, vol. 11325, p. 113250O. doi: 10.1117/12.2551622.
[167] P. Leray, C. Jehoul, O. Inoue, and Y. Okagawa, "Hybrid overlay metrology with CDSEM in a BEOL patterning scheme," *Metrology, Inspection, and Process Control for Microlithography XXIX*, vol. 9424, p. 942408, 2015, doi: 10.1117/12.2087116.
[168] A. Vaid *et al.*, "Holistic metrology approach: hybrid metrology utilizing scatterometry, critical dimension-atomic force microscope and critical dimension-scanning electron microscope," *JM3*, vol. 10, no. 4, p. 043016, Oct. 2011, doi: 10.1117/1.3655726.
[169] L. G. Connolly, T.-F. Yao, A. Chang, and M. Cullinan, "A tip-based metrology framework for real-time process feedback of roll-to-roll fabricated nanopatterned structures," *Precision Engineering*, Apr. 2019, doi: 10.1016/J.PRECISIONENG.2019.04.001.
[170] M. Maroufi and S. O. R. Moheimani, "Cross Coupling in Parallel Kinematic MEMS Nanopositioners," in *Proceedings of the ASME 2015 Dynamic Systems and Control Conference*, Oct. 2016, p. V003T52A006. doi: 10.1115/dscc2015-9824.
[171] H. Vold, J. Crowley, and G. T. Rocklin, "New ways of estimating frequency response functions.," *Sound & Vibration*, vol. 18, no. 11, pp. 34–38, 1984.
[172] H. Nagai, A. Poteet, X. A. Zhang, and C.-H. Chang, "Three-dimensional colloidal interference lithography," *Nanotechnology*, vol. 28, no. 12, p. 125302, Mar. 2017, doi: 10.1088/1361-6528/aa5e3f.
[173] Yongxiao Chen, Jianxin Shen, and Zemin Fang, "Topology and preliminary design of slotless brushless DC motor," in *1997 IEEE International Electric Machines and Drives Conference Record*, May 1997, p. WB2/7.1-WB2/7.3. doi: 10.1109/IEMDC.1997.604311.
[174] J. Seo, J. Kim, I. Jung, and H. Jung, "Design and Analysis of Slotless Brushless DC Motor," *IEEE Transactions on Industry Applications*, vol. 47, no. 2, pp. 730–735, Mar. 2011, doi: 10.1109/TIA.2010.2091611.
[175] N. Bianchi, S. Bolognani, and F. Luise, "High Speed Drive Using a Slotless PM Motor," *IEEE TRANSACTIONS ON POWER ELECTRONICS*, vol. 21, no. 4, p. 9, 2006, doi: 10.1109/TPEL.2006.876824.
[176] H. Garnier, M. Mensler, and A. Richard, "Continuous-time model identification from sampled data: Implementation issues and performance evaluation," *International Journal of Control*, vol. 76, no. 13, pp. 1337–1357, Jan. 2003, doi: 10.1080/0020717031000149636.
[177] "Experiments with Identification of Continuous Time Models," *IFAC Proceedings Volumes*, vol. 42, no. 10, pp. 1175–1180, Jan. 2009, doi: 10.3182/20090706-3-FR-2004.00195.
[178] J. Bibel and D. S. Makyevac, "Guidelines for the Selection of Weighting Functions for H-Infinity Control," U.S. Naval Surface Warfare Center, Dahlgren Division - Weapons Systems Department, NSWCDD/MP-92/43, Jan. 1992.
[179] K. Deb, A. Pratap, S. Agarwal, and T. Meyarivan, "A fast and elitist multiobjective genetic algorithm: NSGA-II," *IEEE Trans. Evol. Computat.*, vol. 6, no. 2, pp. 182–197, Apr. 2002, doi: 10.1109/4235.996017.

[180] E. A. Baltz *et al.*, “Achievement of Sustained Net Plasma Heating in a Fusion Experiment with the Optometrist Algorithm,” *Scientific Reports*, vol. 7, no. 1, Art. no. 1, Jul. 2017, doi: 10.1038/s41598-017-06645-7.
[181] R. W. De Doncker and D. W. Novotny, “The Universal Field Oriented Controller,” *IEEE Transactions on Industry Applications*, vol. 30, no. 1, pp. 92–100, 1993, doi: 10.1109/28.273626.
[182] O. W, “Field Oriented Control: To FOC or not to FOC,” *OlliW’s Bastelseiten*, 2017.
[183] S. K. Mitra, *Digital signal processing: a computer based approach*, 3rd ed. Boston: McGraw-Hill Higher Education, 2006.

APPENDIX A: LABVIEW CODE FOR FPGA CONTROL SYSTEM

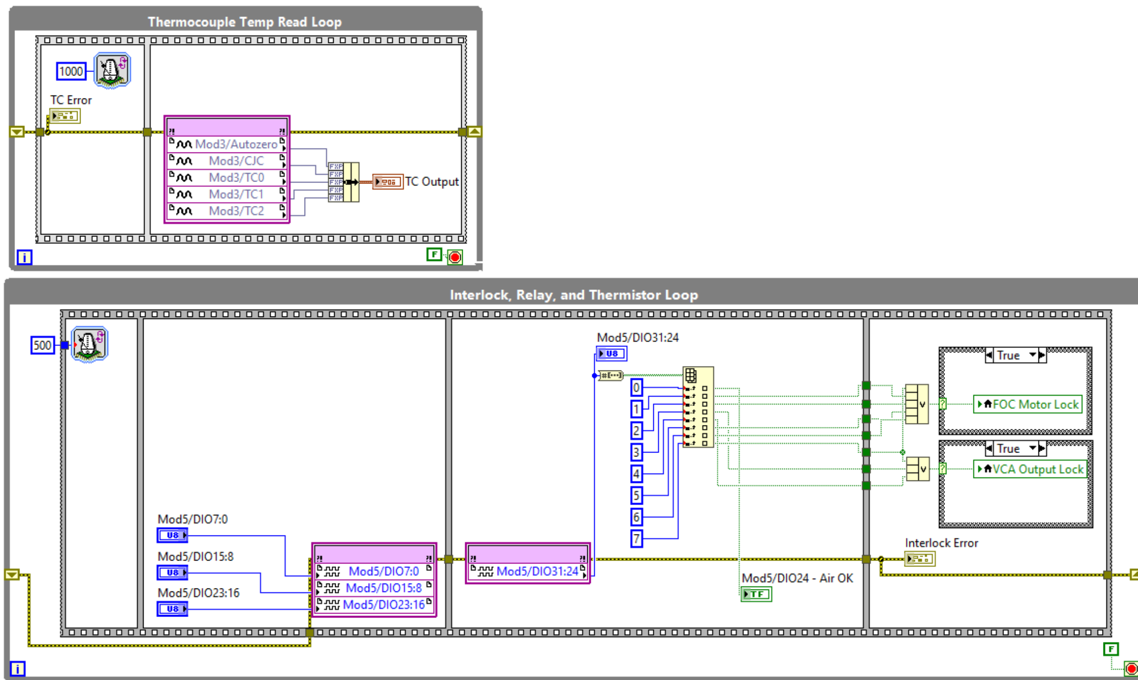

Figure A1: Thermocouple, Interlock, Relay, and Thermistor measurement and control loops.

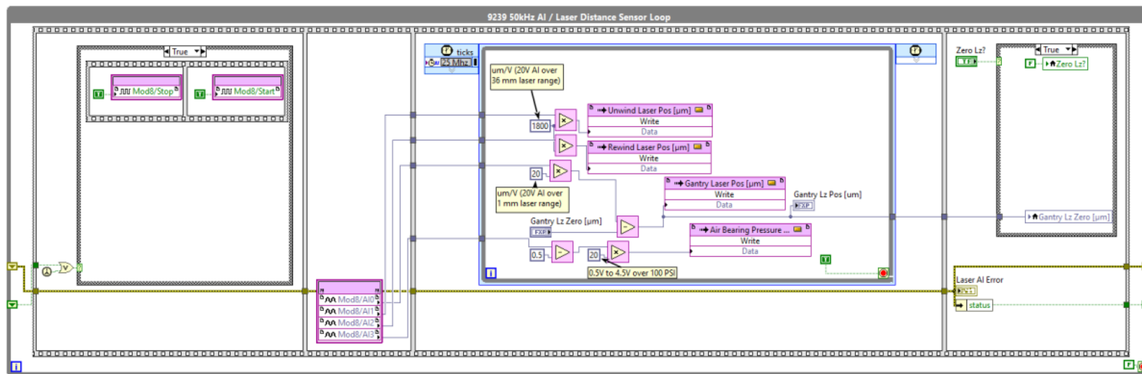

Figure A2: Laser distance sensor and air bearing pressure sensor analog input and scaling loop

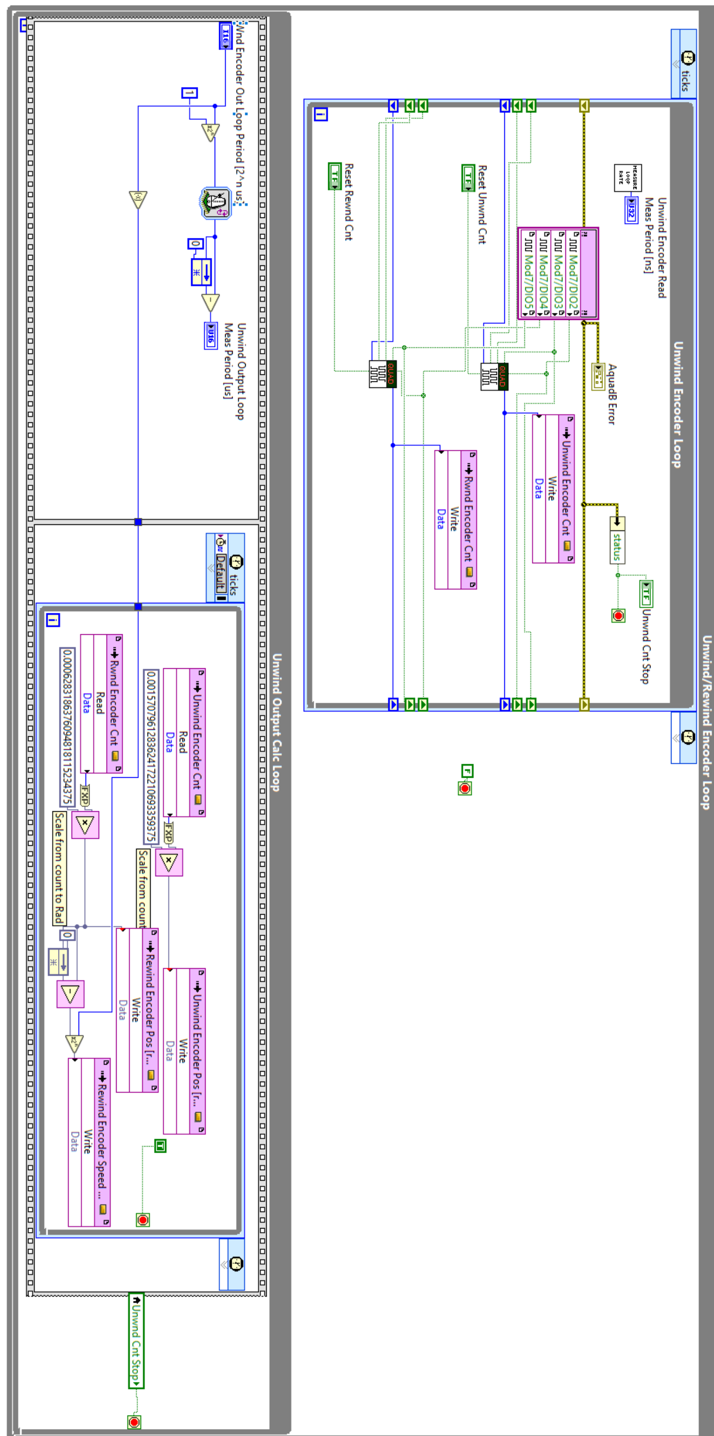

Figure A3: Unwind and rewind stand encoder measurement loops

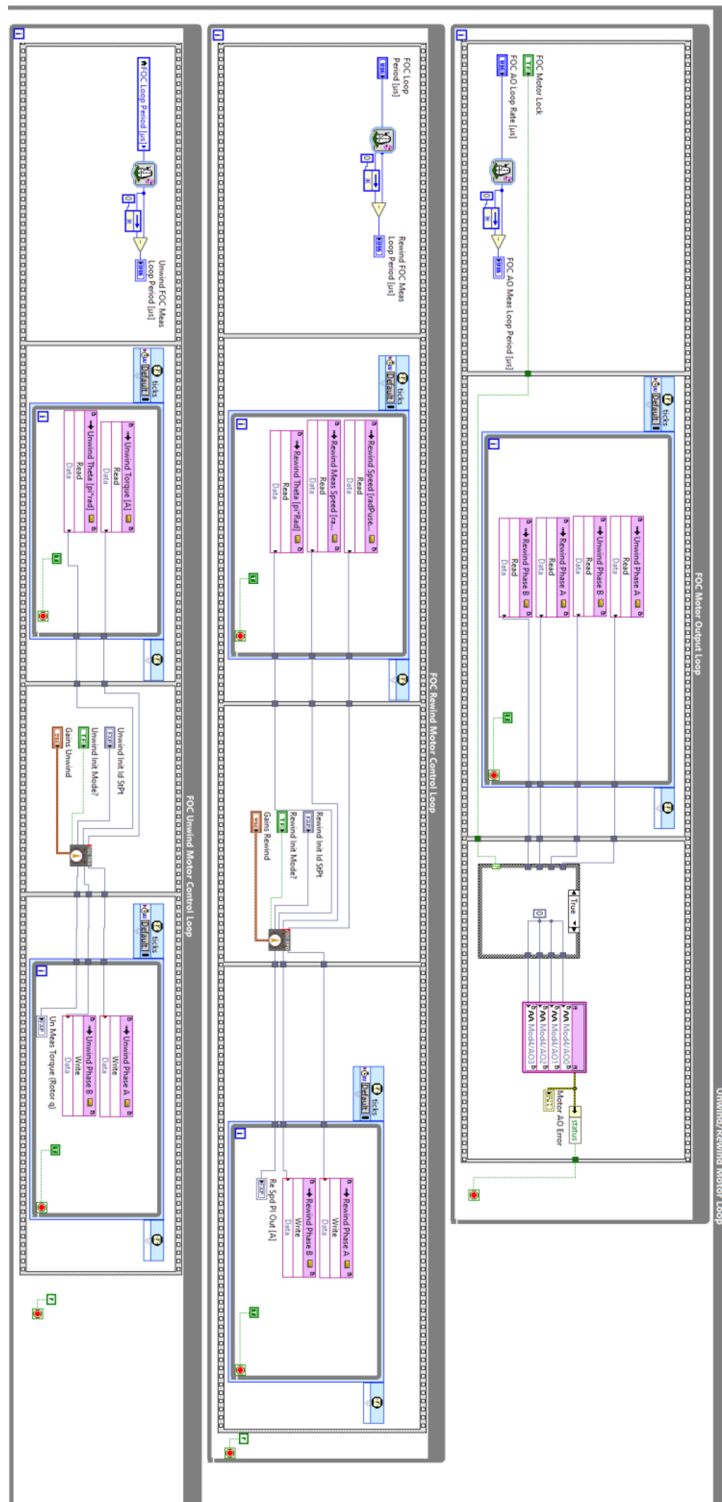

Figure A4: Unwind/rewind motor field oriented control and signal analog output loops.

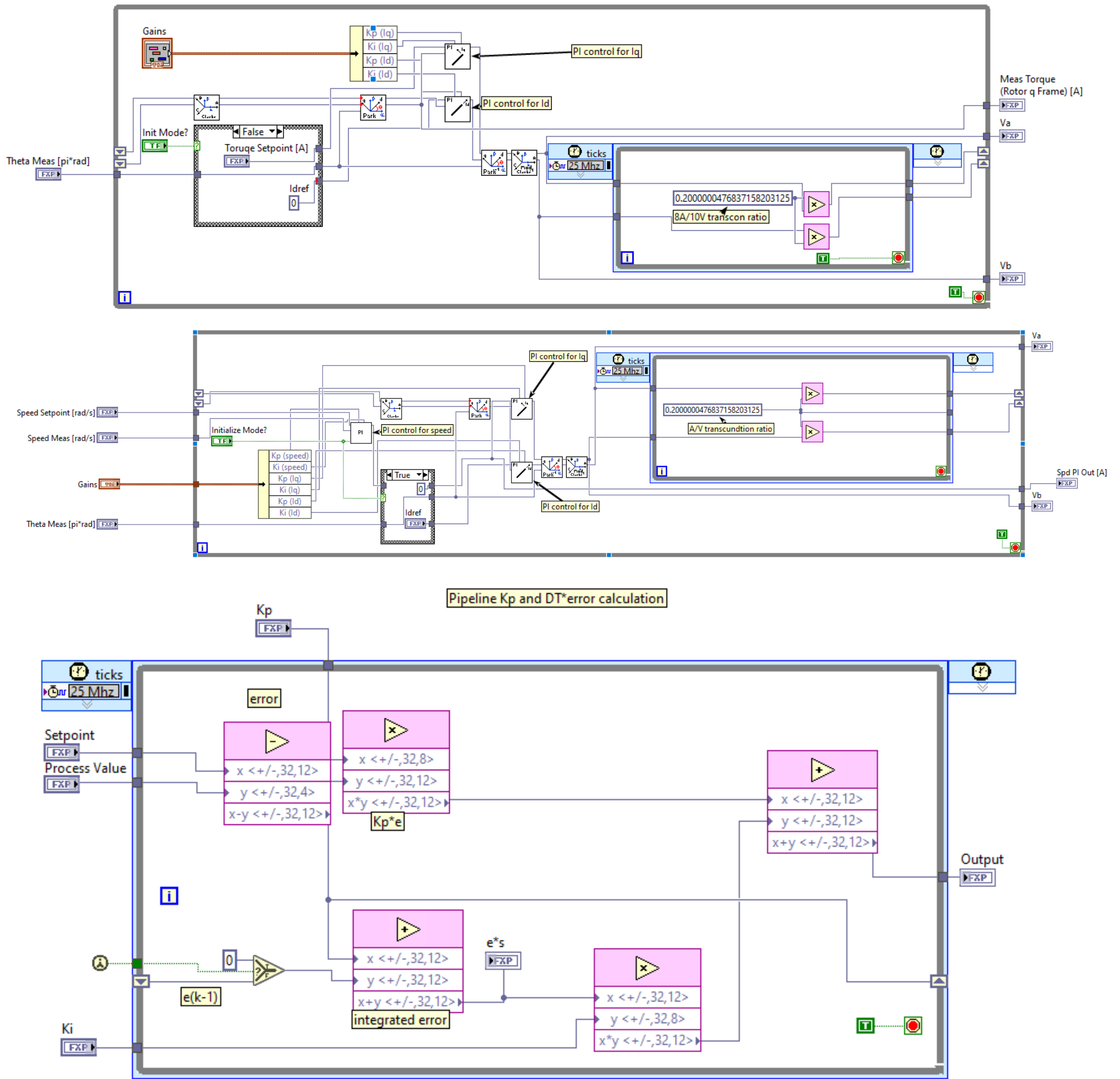

Figure A5: Detail of rotary motor field oriented control algorithm

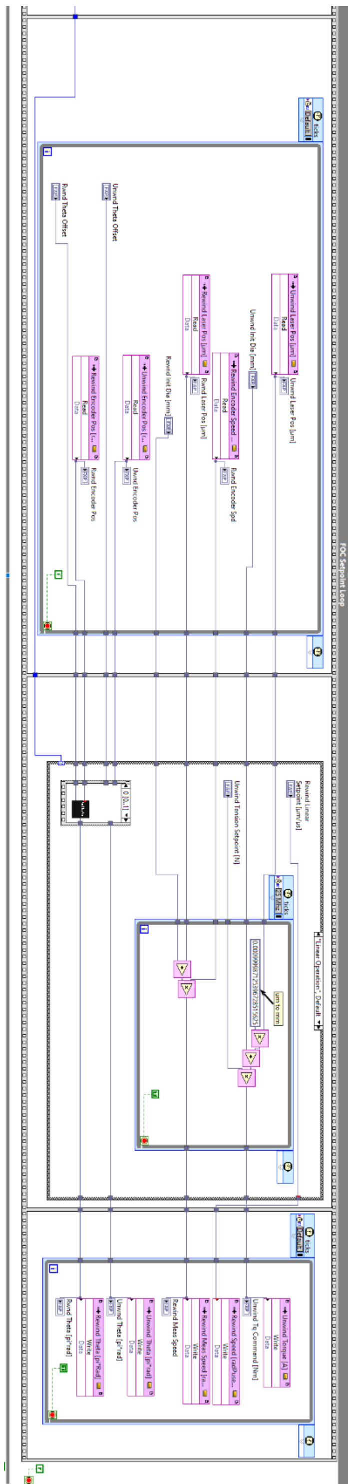

Figure A6: Rotary motor field oriented control setpoint generation loop

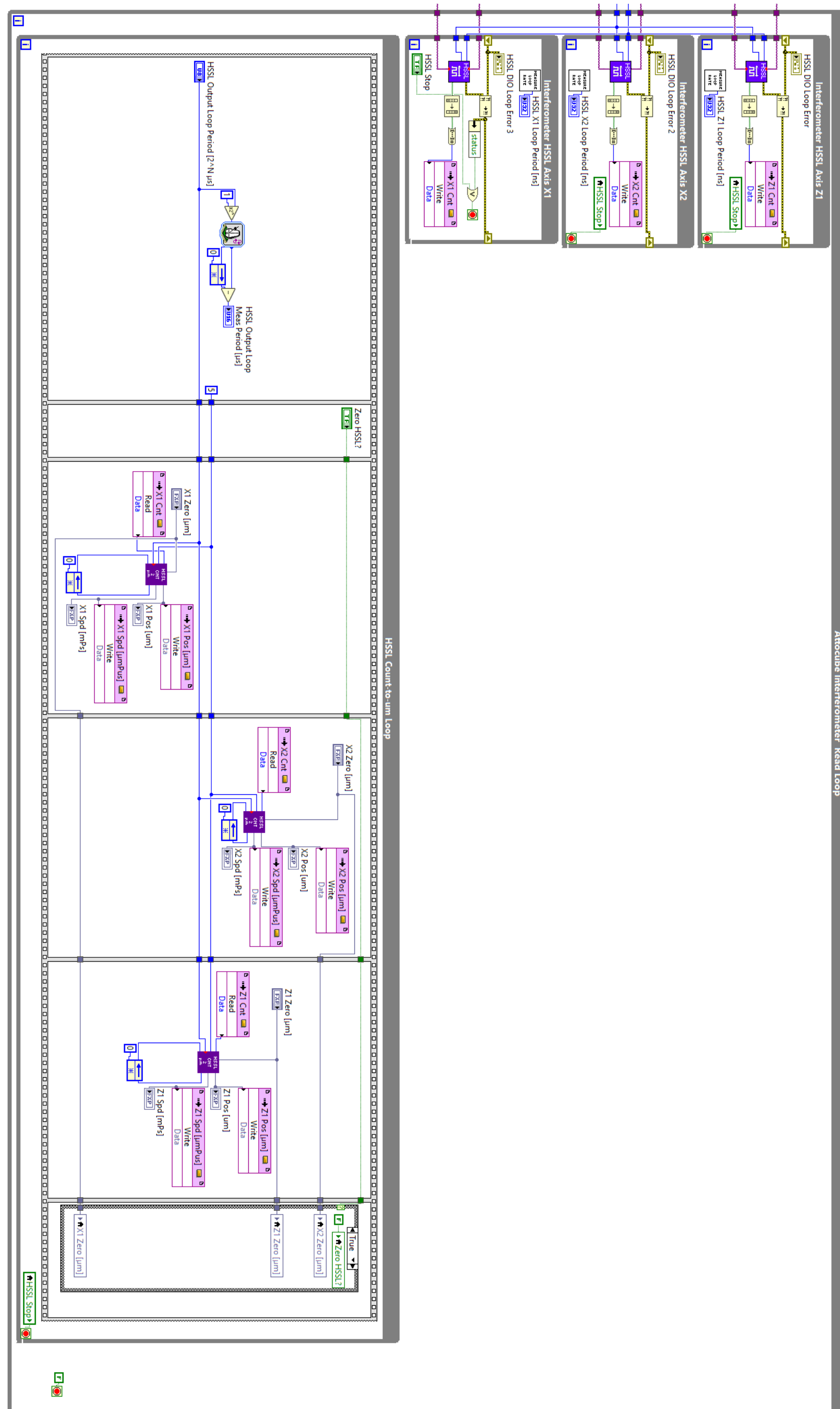

Figure A7: Laser interferometer high speed serial link position and velocity measurement and calculation loops

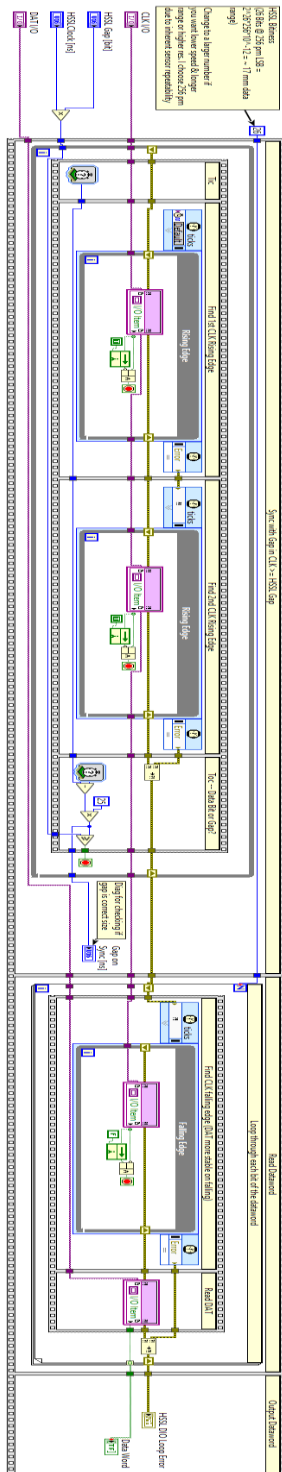

Figure A8: Implementation of high speed serial link interferometer digital communication protocol

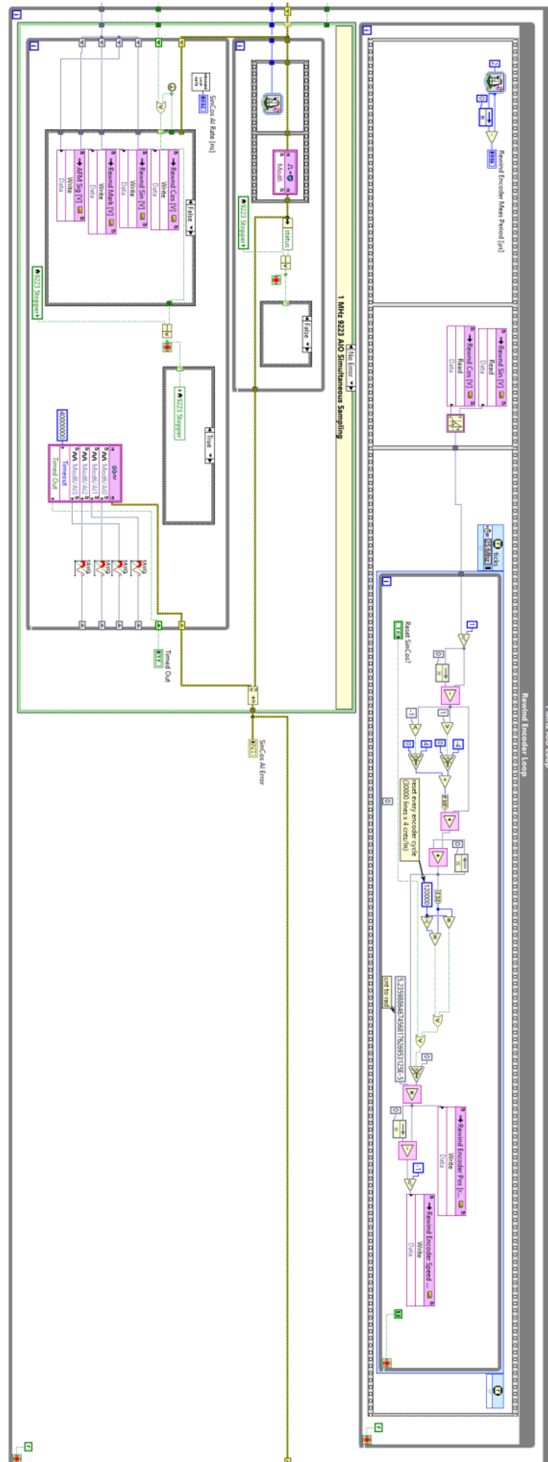

Figure A9: Optical angular encoder high speed 1 MHz analog input module and encoder count interpolation loops

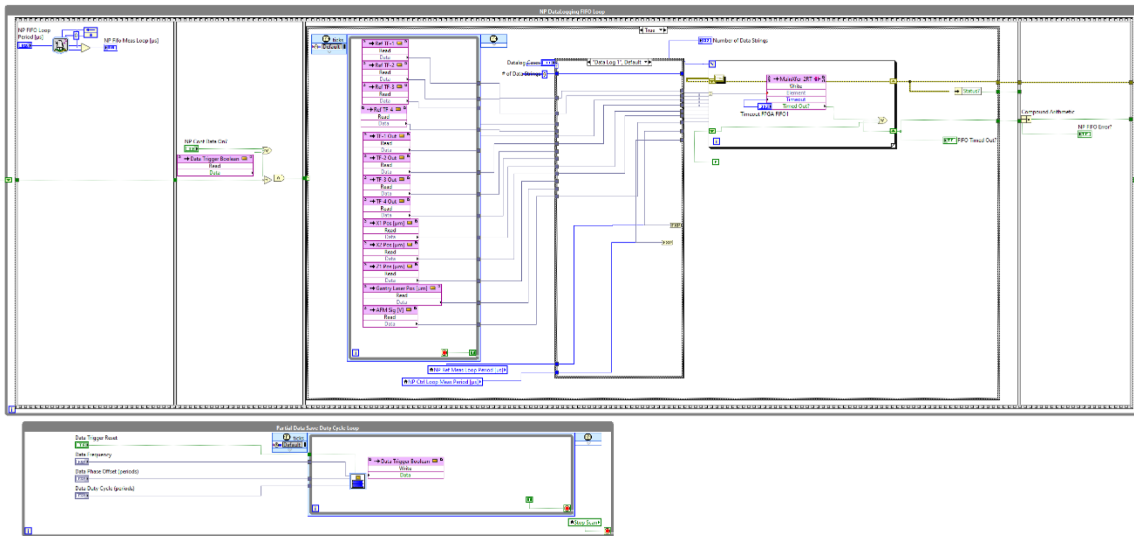

Figure A10: Nanopositioner datalogging loops.

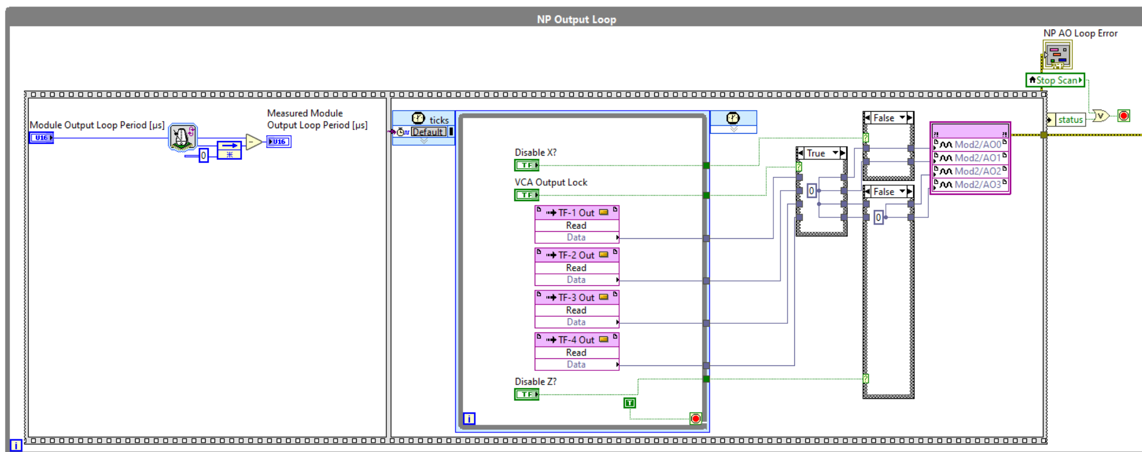

Figure A11: Nanopositioner analog output control signal loop

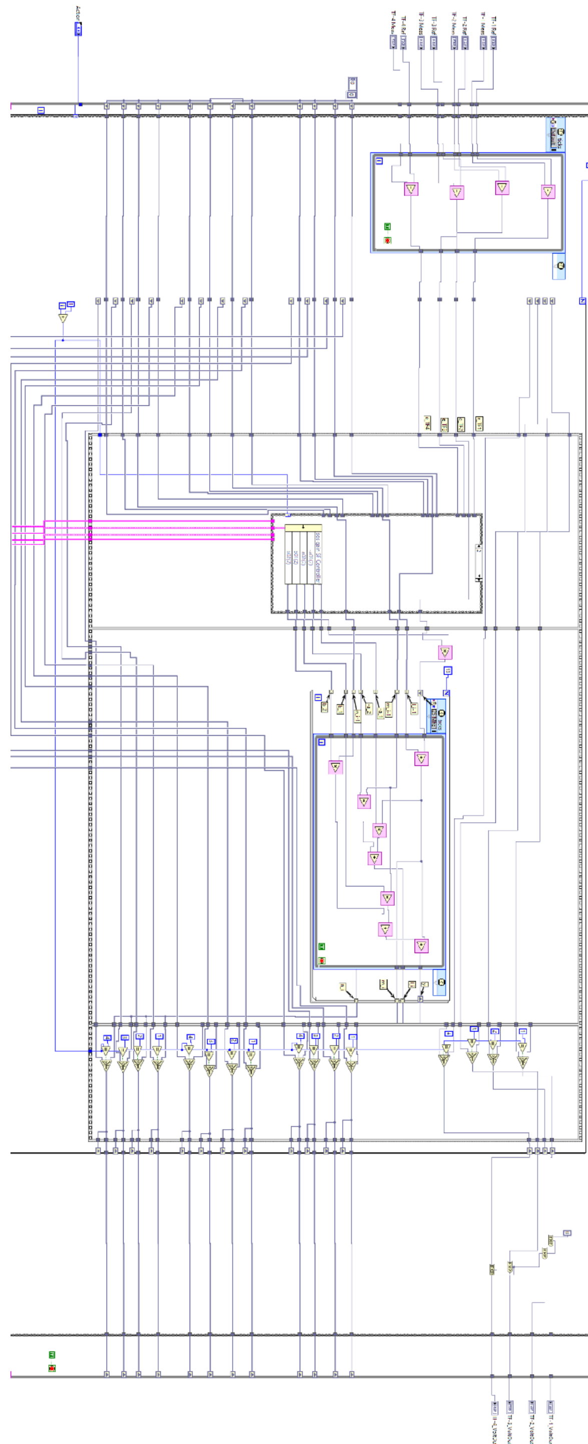

Figure A12: 4-axis higher order transfer function calculation through cascaded second order sections

Figure A13: Nanopositioner setpoint reference generation and control loop

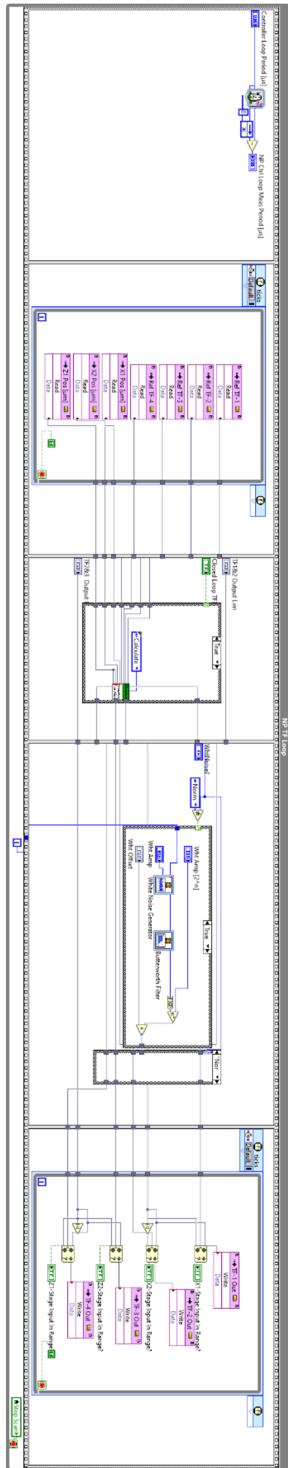

Figure A14: Nanopositioner transfer function calculation loop

APPENDIX B: UPGRADED METROLOGY ROLLER FABRICATION

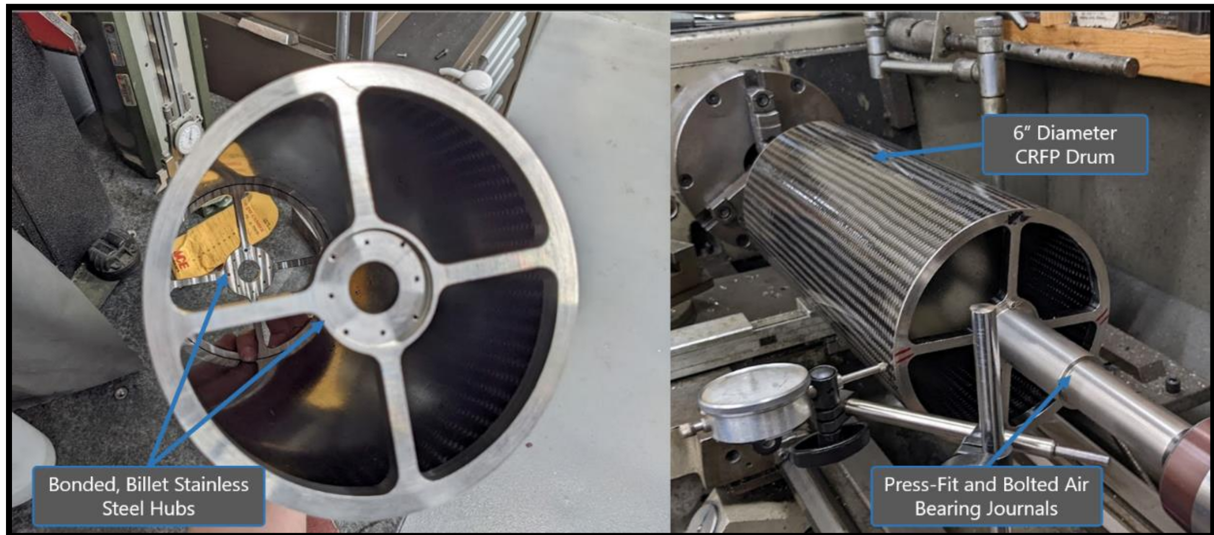

Figure B1: Upgraded idler roller fabrication showing bonding of stainless steel hubs and assembled roller before final precision surface grinding

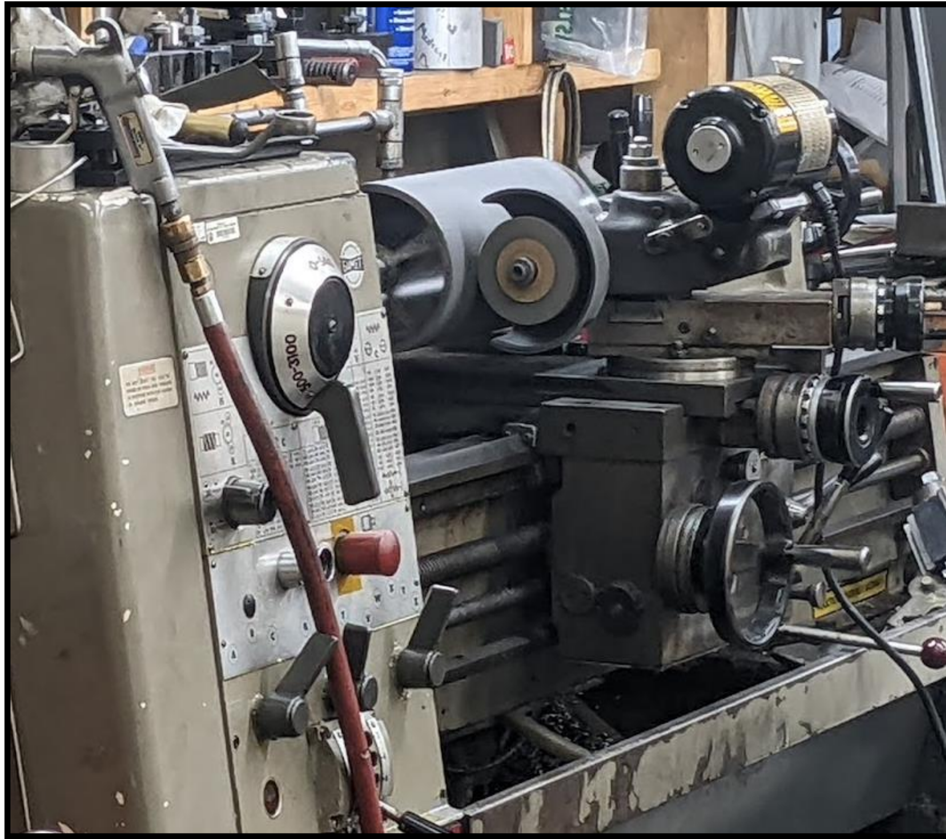

Figure B2: Precision grinding of air bearing journals and CRFP body of upgraded idler roller

Figure B3: Upgraded idler roller after precision surface grinding

Figure B4: Final coating of idler roller CRFP body with acrylic resin based clear coat

Vita

Liam Glazer Connolly was born and raised in Oakland, California. He received a Bachelor of Science in Mechanical Engineering from Tufts University in Medford, Massachusetts in 2016. He joined the Nanoscale Design and Manufacturing Laboratory within the Department of Mechanical Engineering and the NASCENT Nanosystems Engineering Research Center at The University of Texas at Austin in 2016 and received a Master of Science in Mechanical Engineering in 2019.

Liam.Connolly@utexas.edu

This dissertation was typed by the author.